Università degli Studi di Padova

DIPARTIMENTO DI FISICA ED ASTRONOMIA "GALILEO GALILEI"
Corso di Laurea Magistrale in Fisica

Tesi di laurea magistrale

Searching for top partners at the Large Hadron Collider

Candidato:
Piero Ferrarese
Matricola 1034911

Relatori:
Dr. Patrizia Azzi - INFN Sezione di Padova
Dr. Andrea Wulzer - Università e INFN Sezione di Padova

Anno Accademico 2013-2014

Patrizia Azzi

Abstract

After the Higgs boson discovery and the end of the first Large Hadron Collider Run, the Standard Model has reached its complete validation, in the sense that all particles it predicts have been directly observed, no evidence of new physics has emerged so far. Furthermore, while we know for sure that the Standard Model is not thte complete theory of Nature because it lacks of a quantistic description of gravity, and because new physics is needed to describe observed phenonmena such as neutrino masses and oscillations and the Dark Matter component of the Universe, we can not say if this new physics will arise at the TeV scale, within the reach of the Large Hadron Collider, or at much higher energies. The Hierarchy Problem is a theoretical indication that the new Physics scale should be close to the TeV one, if taken seriously it predicts new relatively light particles to be discovered at the Large Hadron Collider. In this thesis we will focus on the s-called "Composite Higgs" scenario, which solves the Hierarchy Problem and predicts a set of new phenomena, such as the production of vector-like quarks that couples to the top-quark, that could be visible at energies of the -order of those explored - and to be explored - at the Large Hadron Collider. The model is based on a global invariance $\mathcal{G}$ of a new strong sector, which is spontaneously broken to its $\mathcal{H}$ subgroup. This breaking produces the Goldstone bosons, one of which we interpret as to be the Higgs. The Goldstone symmetry and the composite nature protect the Higgs mass term from large radiative correction. The analogy is between the standard description of the pions system. In fact, the triplet of bound states of up and down-type quarks emerges as massless in the QCD theory from the breaking of the $SU(2)_L \times SU(2)_R$ down to its vectorial subgroup, that is the standard "isospin" symmetry. The mass is acquired by the tiny explicit breaking of the isospin symmetry. This procedure perfectly describes the spectrum of hadron masses, with spin-1 resonances heavier then the light triplet of pions. Recasting this procedure, enlarging the global symmetry in order to contain the Standard Model gauge groups, results in a mechanism that generates a composite Higgs, boson, from a new strong sector, which is naturally lighter than the other resonances (we have not yet seen). In this framework, new particles transforming in the unbroken global group of invariance emerge, and couple to the Standard Model fermions and gauge bosons. Among all these new particles, a major role is played by the Top Partners, because they turn out to be responsable for the radiative generation of the Higgs mass. Therefore, Naturalness requires them to be light and indeed in explicit models they are the lightest new states in the spectrum. In this thesis, after setting the environment, describing the Standard Model and its great success and issues, we will briefly review the Composite Higgs model in the coset $SO(5)/SO(4)$, and describe the main features of the phenomenology of the top-partners production and decay. In particular we focus on the field transforming in the singlet of the $SO(4)$, that we call $\tilde{T}$. This is a particle with charge 2/3 and a TeV-scale mass - variable with the parameters set in the model. The theoretical instruments used to describe this particle are those of the effective field theory. In the second part of the thesis, from chapter 4 onwards, we discuss the possible experimental manifestation of the $\tilde{T}$, singly produced in association with a botto quark and forward jet, in the Compact Muon Solenoid detector. After a brief desciption of the experimental apparaturs and of the reconstruction algorithms, we discuss our search strategy. Since the mechanism of production is exactly the same of that of the top-quark single production, except for the different mass of the particle, that is heavier, our search elaborates the "singe top" analysis already done rfrom the Compact Muon Solenoid collaboration[1] Five different scenario are discussed, with different mass values between 600 e 1000 GeV - that are the most promising for cross sections. Our search deals with data from 2012 run of the Large Hadron Collider, with center of mass energy and luminosity of respectively

[1]Thanks go to CMS-Napoli group, in particular Alberto Orso Maria Iorio and Luca Lista for providing the needed tools for the analysis.

$\sqrt{s} = 8\,\text{TeV}$ and $\int \mathcal{L}dt = 19.7\,fb^{-1}$. Bounds on the production of top-quark like partners at the Large Hadron Collider are already present, coming from pair production analysis, both from CMS and ATLAS. Those analysis set limits 696 GeV.

Contents

List of Figures

List of Tables

Chapter 1

Standard Model and Beyond

1.1 Standard Model review

The Standard Model is a theory of quarks and leptons and is the most predictive theory of all time in high energy physics. It describes three of the four fundamental interactions among particles. It consists of two successful theories formulated during the 60's and the 70's of the 20th century: the electroweak theory (Glashow-Salam-Weinberg model - GSW, [5]) and the Quantum Chromodynamics (QCD, [6] for a review and applications to collider physics). The Standard Model has been validatedin an uncredibly wide and accurate way. A recent confirmation comes from the discovery of the Higgs boson [7] and [8], the Standard Model picture is now complete in the sense that all the predicted particles have been directly observed. The Standard Model of fundamental interactions is a relativistic quantum field theory. The keyword for understanding its construction is symmetry. Another important concept in quantum field theory is *renormalizability*. We know that divergences appear everywhere and must be eliminated by suitable redefinitions of couplings and fields. In the theories we call "renormalizable", this procedure can be carried on at all orders in perturbation theory by renormalizing a finite set of comupling, while in the so-called "non-renormalizable" ones new couplings have to be introduced at each new perturbative oreder. Furthermore, it turns out that only renormalizable theories have the chance of maintaining predictivity (i.e. perturbativity) up to very high, practically infinite, energy scales. One must thus focus on renormalizable theories to obtain a "complete" model, and thus is what we do when we construct the Standard Model theory.

The interactions and the particle spectrum are classified by a local invariance of the action under some group of transformation. The complete local symmetry group is

$$SU(3)_C \times SU(2)_L \times U(1)_Y \tag{1.1}$$

and the only (imposed) global group of invariance is the Poincaré group of translations and Lorentz rotations The second important role in the construction of the Standard Model is played by the paradigm of spontaneously broken symmetry which is needed to give mass to fermions and gauge bosonsTo write local invariant Lagrangians we need to define the covariant derivative

$$D_\mu = \partial_\mu - ig' W_\mu^a \frac{\sigma^a}{2} - ig\frac{Y}{2} B_\mu - ig_S \frac{\lambda^i}{2} A_\mu^i \tag{1.2}$$

$a = 1, 2, 3$ and $i = 1, ..., 8$ run on the dimension of the adjoint representions of the gauge groups (respectively of weak and strong interactions - $SU(2)_L$ and $SU(3)_C$). Here σ^a are the Pauli matrices, generators of $SU(2)_L$, λ^i (Gell-Mann matrices) are the generators of the colour group $SU(3)_C$.An explicit parametrization is given in the appendix. These matrices satisfy the normalization conditions

$$Tr(\lambda^i \lambda^j) = 2\delta^{ij}\,, \qquad Tr(\sigma^a \sigma^b) = 2\delta^{ab}\,. \tag{1.3}$$

	$SU(3)_C \times SU(2)_L \times U(1)_Y$
$q_L = \begin{pmatrix} u_L \\ d_L \end{pmatrix}$	$(\mathbf{3}, \mathbf{2}, 1/6)$
u_R	$(\overline{\mathbf{3}}, \mathbf{1}, 2/3)$
d_R	$(\overline{\mathbf{3}}, \mathbf{1}, -1/3)$
$l_L = \begin{pmatrix} \nu_L \\ e_L \end{pmatrix}$	$(\mathbf{1}, \mathbf{2}, -1/2)$
e_R	$(\mathbf{1}, \mathbf{1}, -1)$
$H = \begin{pmatrix} H^+ \\ H^0 \end{pmatrix}$	$(\mathbf{1}, \mathbf{2}, 1/2)$

Table 1.1: Standard Model fermion and scalar field content and related quantum numbers. Family indices are not explicitly written

A^i_μ are the eight gluons, mediators of the strong interactions. W^a_μ and B_μ mix to give the fields corresponding to the $W^\pm$ and Z, mediators of the weak interactions, and of A_μ, the photon, mediator of the electromagnetic force. The electric charge is reproduced by defining

$$Q = T_{3L} + Y \tag{1.4}$$

T_{3L} is the third component of the weak isospin (the eigenvalue of T^3), Y is the hypercharge Then we can write the kinetic part of the entire Standard Model Lagrangian, that is

$$\mathcal{L}_k = \sum_i i\bar{\psi}^i \not{D} \psi^i + \left(D^\mu H^\dagger\right)(D_\mu H) \tag{1.5}$$

where $\psi^i = q_L, u_R, d_R, l_L, e_R$; Feynman notation is introduced $\not{D} \equiv D_\mu \gamma^\mu$. The kinetic terms for the gauge fields are written through the field-strength

$$\mathcal{L}_{k,gauge} = -\frac{1}{4} A^i_{\mu\nu} A^{\mu\nu,i} - \frac{1}{4} W^a_{\mu\nu} W^{\mu\nu,a} - \frac{1}{4} B_{\mu\nu} B^{\mu\nu} \tag{1.6}$$

$$A^i_{\mu\nu} = \partial_\mu A^i_\nu - \partial_\nu A^i_\mu + g_S f^{ijk} A^j_\mu A^k_\nu \tag{1.7}$$

$$W^a_{\mu\nu} = \partial_\mu W^a_\nu - \partial_\nu W^a_\mu + g_W f^{abc} W^b_\mu W^c_\nu \tag{1.8}$$

$$B_{\mu\nu} = \partial_\mu B_\nu - \partial_\nu B_\mu \tag{1.9}$$

f^{abc} and f^{ijk} are the structure constants, defined in group theory as

$$\frac{1}{2}\left[\lambda^i, \lambda^j\right] = \frac{i}{2} f^{ijk} \lambda^k \tag{1.10}$$

$$\frac{1}{2}\left[\sigma^a, \sigma^b\right] = \frac{i}{2} f^{abc} \sigma^k \tag{1.11}$$

$f^{abc} = \epsilon^{abc}$ is the standard Levi-Civita complete antisymmetric tensor. Finally, also operators involving the Higgs and the fermions can be written. The complete Lagrangian reads

$$\begin{aligned} \mathcal{L} = \bar{q} i \not{D} q + \bar{l} i \not{D} l - \frac{1}{4}\left(W^a_{\mu\nu}\right)^2 - \frac{1}{4}\left(B_{\mu\nu}\right)^2 - \frac{1}{4}\left(G^i_{\mu\nu}\right)^2 + \\ + |D_\mu H| - V(H) - , \\ - \left(\lambda_u \bar{u}_R H \cdot Q_L + \lambda_d \bar{d}_R H^c \cdot Q_L + \lambda_l \bar{e}_R H^c \cdot L_L + h.c.\right) \end{aligned} \tag{1.12}$$

where H denotes the Higgs doublet and $H^c = i\sigma_2 H^*$ has the same quantum numbers of H but opposite hypercharge $Y = -1/2$.

1.1.1 Higgs mechanism

The Lagrangian of Eq. 1.12 contains no more terms and describes exactly massless particles. Instead we need masses, but we can not just add gauge bosons and fermion masses, because tese are not invariant. For the gauge fields, in particular

$$B_\mu B^\mu \to B_\mu B^\mu + \frac{2}{e} B^\mu \partial_\mu \alpha + \frac{1}{e^2} \partial_\mu \alpha \partial^\mu \alpha \,. \tag{1.13}$$

and similarly for the $SU(2)_L$ fields W^a_μ. The Higgs mechanism provide a method to give mass to the gauge bosons. The Higgs mechanism has its root in the Goldstone theorem, that gives an importan result in the case of global symmetries. We can summarize the result of the Goldstone's theorem in this enunciate

Theorem. *Given a Lagrangian invariant under a global continuous group of symmetry G, with $dim[G] = N$, if the vacuum state is not invariant under a transformation of G, but it breakes the group along M directions, associated to M independent broken generators, then M Nambu-Goldstone massless bosons broken generators appear in the spectrum.*

When the symmetry is local, the massless Nambu-Goldstone bosons are "eaten" by the longitudinal polarisation of the vector gauge bosons, that become massive. Thus is what we call the Higgs mechanism. Gauge invariance and renormalizability restricts the scalar potential to be

$$V(H) = m^2 |H|^2 + \lambda |H|^4 \tag{1.14}$$

the choice $\lambda > 0$ makes the potential bounded from below and $m^2 < 0$ ensures the non-invariance of the vacuum state. To extremize the action we look for constant configurations which are minima

$$|\langle H \rangle|^2 = -\frac{m^2}{2\lambda} \equiv \frac{v^2}{2} \,. \tag{1.15}$$

The general solution of this equation, up to a gauge transformation, can be set o

$$\langle H \rangle = \frac{1}{\sqrt{2}} \begin{pmatrix} 0 \\ v \end{pmatrix} \tag{1.16}$$

with $v > 0$. This is still invariant under $U(1)_{em}$, so the spontanous breaking pattern is

$$SU(2)_L \times U(1)_Y \to U(1)_{em} \,. \tag{1.17}$$

Accordingly, the photon will remain massless and the $W^\pm$,Z fields associated with the three broken generators will acquire a mass. Fluctuations around the Vacuum Expectation Value can be parametrized, again up to a gauge choice, as

$$H = \frac{1}{\sqrt{2}} \begin{pmatrix} 0 \\ v + h(x) \end{pmatrix} \,, \tag{1.18}$$

and the kinetic Lagrangian becomes

$$\mathcal{L}_H = \frac{1}{2} \partial_\mu h \partial^\mu h + \frac{(v+h)^2}{8} \left[g^2 |W^{\mu,1} + i W^{\mu,2}|^2 + (g' B^\mu - g W^{\mu,3})^2 \right] \,. \tag{1.19}$$

This gives mass to the gauge fields, the mass eigenstates are

$$W^\pm_\mu = \frac{W^1_\mu \pm W^2_\mu}{\sqrt{2}} \tag{1.20}$$

$$\begin{pmatrix} A_\mu \\ Z_\mu \end{pmatrix} = \begin{pmatrix} cos\theta_w & sin\theta_w \\ -sin\theta_w & cos\theta_w \end{pmatrix} \cdot \begin{pmatrix} B_\mu \\ Z_\mu \end{pmatrix} \,, \tag{1.21}$$

the weak mixing angle is defined as $tan\theta_w = g'/g$. We can rewrite the Lagrangian

$$\mathcal{L}_H = \frac{1}{2}\partial_\mu h \partial^\mu h + \frac{(v+h)^2}{4} g^2 W^{\mu,+} W^{\mu-2} + \frac{(v+h)^2}{8}(g'^2 + g^2) Z_\mu Z^\mu \,, \tag{1.22}$$

from which we deduce the mass terms

$$M_W^2 = \frac{1}{4} g^2 v^2 \tag{1.23}$$

$$M_Z^2 = \frac{1}{4}(g^2 + g'^2)v^2 = \frac{M_W^2}{cos^2\theta_w} \,. \tag{1.24}$$

Also the physical Higgs boson particle, $h(x)$, is massive. The scalar potential, up to a constant reads

$$V(h) = \frac{1}{2}(2\lambda v^2)h^2 + \lambda v h^3 + \frac{\lambda}{4} h^4 \,, \tag{1.25}$$

from which we find

$$m_h = 2\lambda v^2 \,. \tag{1.26}$$

Interaction vertices among the fermions and the gauge fields arise from the covariant derivative, written in the mass eigenstates basis for gauge bosons

$$\mathcal{L}_{cc} = \frac{g}{\sqrt{2}2} W^+_{mu} \left(\bar{\nu}_L \gamma^\mu e_L + \bar{u}_L \gamma^\mu d_L\right) + h.c. \,, \tag{1.27}$$

$$\mathcal{L}_{nc} = \sum_i \left[e A_\mu q^i \bar{\psi^i} \gamma^\mu \psi^i + \frac{g}{cos\theta_w} Z_\mu \left(T^i_{3L} - sin^2\theta_w q^i\right) \bar{\psi^i} \gamma^\mu \psi^i \right] \,, \tag{1.28}$$

$$\mathcal{L}_{qg} = g_S \left(\bar{u}\gamma^\mu \mathcal{T}^i u + \bar{d}\gamma^\mu \mathcal{T}^i d\right) A^i_\mu \,. \tag{1.29}$$

where $\psi^i = q_L, u_R, d_R, l_L, e_R$ and q^i are the associated electric charges.From the above equation we see, first of all, that the correct electromagnetic interactions with the photon are reproduced, with the electric charge given by $e = g' \cos\theta_w = g \sin\theta_w$. Second, now that we know the couplings of the W we can spite the Fermi costant G_F which controls charged weak interactions at low energy and is precisely measured in the muon decay process. Knowing that $G_F = \frac{1}{\sqrt{2}v^2}$, we find $v \simeq 246\,\text{GeV}$. Finally, from $m_Z =$ all the costants $g =$,$g' =$. The Higgs mass, or λ instead can be fixed only by m_H.

1.1.2 Fermion masses

As for the gauge fields, the mass of the fermions cannot be simply introduced by hand in the Lagrangian because this would break the symmetries, since every quadratic term in fermion fields break the local gauge invariance. The mechanism relies again on the presence of the Higgs boso and on the presence of Yukawa interactions , as reported in Eq. 1.12, which we rewrite here in a long-winded form

$$\mathcal{L}_Y = -(\lambda_u)_{mn} \bar{q}_{L,m} H^* u_{R,n} - (\lambda_d)_{mn} \bar{q}_{L,m} H u_{R,n} - (\lambda_e)_{mn} \bar{l}_{L,m} H^* e_{R,n} + h.c. \tag{1.30}$$

λ_i are complex 3×3 matrices in the flavour space. After the Higgs takes a Vacuum Expectation Value $\mathcal{L}_Y$ leads to mass terms for the charged leptons and for the up- and down-type quarks

$$-(\lambda_e)_{mn} \frac{v}{\sqrt{2}} \bar{e}_{L,m} e_{R,n} - (\lambda_u)_{mn} \frac{v}{\sqrt{2}} \bar{u}_{L,m} u_{R,n} - (\lambda_d)_{mn} \frac{v}{\sqrt{2}} \bar{d}_{L,m} d_{R,n} h.c. \tag{1.31}$$

In order to read the mass eigenstates, the Yukawa matrices must be diagonalized

$$L_f^\dagger \lambda_f R_f = \lambda_f^d \tag{1.32}$$

where $f = d, u, e$; λ_f^d si diagonal with positive elements. After the rotation, the neutral current interactions in Eq. 1.30 are unchanged while the charged current one becomes

$$\mathcal{L}_{cc} = \frac{g}{\sqrt{2}} W_\mu^+ \left(\bar{\nu'}_L \gamma^\mu e'_L + \bar{u'}_L \gamma^\mu V_{CKM} d'_L \right) + h.c.\,. \tag{1.33}$$

where $V_{CKM} = R_f^\dagger L_f$ is the Cabibbo-Kobayashi-Maskawa matrix. Explicitely

$$V_{CKM} = \begin{pmatrix} |V_{ud}| & |V_{us}| & |V_{ub}| \\ |V_{cd}| & |V_{cs}| & |V_{cb}| \\ |V_{td}| & |V_{ts}| & |V_{tb}| \end{pmatrix} . \tag{1.34}$$

The non-diagonal entries lead to flavour transition in the quark sector, compatible with present observations.

1.1.3 The Standard Model as an Effective Field Theory

The Standard Model of course can not be the fundamental theory, because of the lack of a renormalizable theory of gravitational interactions. This is one sure reason to regard the Standard Model as en effective field theory, valid the energies explored so far which loses his validity at some cut-off Λ_{SM}, where new particles and interactions appear. Above that scale, the Standard Model is replaced by a more fundamental theory generally called an Ultra Violet completion. An analogy of this situation could be given by Fermi's theory of weak interactions: it is valid for energies below the mass of the Electroweak bosons, $E \sim m_Z$, at higher energy the Standard Model is the predictive theory we have to use. The dimensional analysis of the operator composing the Lagrangian is a powerful tool when we want to match the effective theory with the fundamental one. Some new physics has to exist, even if it might arise at very high energy scales, that we can not access nowadays. We do not know which is the right Ultra Violet (UV) completion of the Standard Model, anyway it will give rise to a low-energy effectiv Lagrangian of the form

$$\mathcal{L}_{SM} = \mathcal{L}^{d=4} + \frac{1}{\Lambda_{SM}} \mathcal{L}^{d=5} + \frac{1}{\Lambda_{SM}^2} \mathcal{L}^{d=6} + \dots\,. \tag{1.35}$$

From this point of view we understand why the effects of operators with $d > 4$ are not included in the "canonical" Standard Model Lagrangian of the previous section: they are suppressed by powers of the cut-off energy so that they give very sal constributions and can be safely neglected. But not all the $d > 4$ operators are necessarily irrelevant. As described below, a $d = 5$ operator could account for the small observed neutrino masses, provided they are Majorana. In order to better appreciate the virtues of the Standard Model interpretated as an Effective Field Theory, it is useful to introduce the concept of accidental symmetries. If truncated at $d = 4$, the Standard Model Lagrangian posesses other global symmetries besides the gauge and Poincarè invariance which we assumed by construction. The fact that those symmetries are not imposed as principles means that the fundamental theory could badly violate them. Accidental symmetries are a big phenomenological succes of the theory, so it is remarkable that they could arise at that energy scale. One such symmetry is baryon number conservation which forbids the proton to decay, if it was badly violated it would be a serious problem for our life. At the level of $d = 4$ operators, baryon number is exact and the proton is exactly stable. However there are $d = 6$ operators like

$$\frac{1}{\Lambda^2} \epsilon^{abc} (\bar{q}_L)_\alpha (q_L^c)_\beta (\bar{q}_L)_\gamma (e_L^c) \tag{1.36}$$

which violate baryon number, leading to decays by the Feynman diagrams in Fig. 1.1. We estimate

$$\Gamma(p \to e^+ \pi^0) \simeq 1/\tau \sim \frac{1}{8\pi} \frac{1}{\Lambda_{SM}^4} m_p^5 \,. \tag{1.37}$$

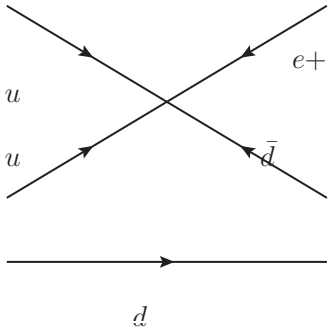

Figure 1.1: Feynman diagram for the pion decay

The proton can thus be made arbitrarily long lived, for large energies Λ_{UV}. The Super-Kamiokande experiment in Japan has set an experimental bound on the decay of the proton $\tau = 1/\Gamma(p \to e^+\pi^0) \geqslant 2.3 \times 10^{33}$ years, [10], this incredibly long lifetime is very easy to understand in the Standard Model. Given the present bound we extimate

$$1\,\mathrm{s} = 300000 \times 10^{18}\,\mathrm{fm} \tag{1.38}$$

$$1 = \hbar c = 197\,\mathrm{MeV}\cdot\mathrm{fm} \Rightarrow fm = \frac{1}{197\,\mathrm{MeV}} \sim 5\,\mathrm{GeV}^{-1} \tag{1.39}$$

$$\Gamma_p \lesssim \frac{1}{3.2\times 10^{32}}\frac{1}{1.5\times 10^{24}}\,\mathrm{GeV} = 2\times 10^{-64}\,\mathrm{GeV} \tag{1.40}$$

$$\Rightarrow \Lambda_{SM} \geq m_p\left(\frac{m_p}{8\pi\Gamma_p}\right) \simeq 3.7\times 10^{15}\,\mathrm{GeV} \tag{1.41}$$

The second important accidental symmetry is *lepton* flavor conservation. After diagonalizing the lepton Yukawas by the relations in Eq. 1.32 we find that the $d = 4$ Lagrangian is invariant under

$$U(1)_{Le} \times U(1)_{L\mu} \times U(1)_{L\tau} \tag{1.42}$$

under which the three leptons families rotate independently. This symmetry forbids any flavor-changing transition in the lepton sector. Experimentally, processes like flavor-violating decays of the μ are indeed largely suppressed[1]

$$Br(\mu \to e\gamma) \leq 1.2\times 10^{-11} \tag{1.43}$$

$$Br(\mu \to eee) \leq 1.0\times 10^{-12} \tag{1.44}$$

$$, \tag{1.45}$$

as expected in the Standard Model with large Λ_{SM}. However by the observation of neutrino masses and oscillations we know that lepton flavor is a a good approximate symmetry, but not an exact one. But this is not a failure of the Standard Model, actually could be a great succes. At $d = 4$, lepton flavor is exact and neutrinos are massless, but both these features are violated by a five-dimensional operator

$$\frac{c}{\Lambda_{SM}}(\bar{e}_L^t H)(e_L H^*) \tag{1.46}$$

which leads, after the Higgs takes a Vacuum Expectation Values, to a Majorana neutrino mass-matrix

$$m_\nu \sim \frac{v^2}{\Lambda_{SM}}\,, \tag{1.47}$$

[1] As attested by [11]

this can lead to a neutrino oscillaion and masses. The expected size of m_ν is of around 0.1 eV, which could be naturally accounted in this framework if $\Lambda + SM \sim 6 \times 10^{14}$. Thus we understand why lepton flavor violation and small ν masses if Λ_{SM} is large enough. It is interesting to note that the first evidences of new phenomena beyond Standard Model, such as neutrino masses and oscillations, could come from the first sector with higher dimensionality than $\mathcal{L}_{SM}^{d=4}$, that is the less suppressed by the scale of new physics. What we would need now is to confirm, or disprove this picture then to establish experimentally whether m_ν is Majorana or not.

1.2 Open issues in the Standard Model

By the arguments presented up to now, it seems extremely plausible that the Standard Model is the valid theory of Nautre up to very high energies, far above the current and foreseen experimental reach, of the order of the so-called Grand Unification Scale, $M_{GUT} \sim 10^{16}\,\text{GeV}$. This is indeed a plausible picture, which is however contradicted by another argument, the so-called *Hierarchy Problem*, which can be formulated as follows. By power-counting, i.e. dimensional analysis, we estimatd that an operator with $d > 4$ must be suppressed by the appropiate power of Λ_{SM}, but exactly the same argument tells us that an operator with $d < 4$ must instead be enhanced

$$\mathcal{L} = \mathcal{L}^{d\geq 4} + \Lambda_{SM}^{d'} \mathcal{L}^{d'<4} \tag{1.48}$$

The only such operator is the Higgs boson mass term

$$m_H^2 H^2 \simeq c\Lambda_{SM}^2 H^2 \tag{1.49}$$

Then, comparing with the Large Hadron Collider result $m_H = 125\,\text{GeV}$

$$\frac{(m_H^2)_{true}}{(m_H^2)_{estimate}} \sim 10^{-16} \tag{1.50}$$

Why the power-counting estimate is so badly violated? This is the esseence of the Hierarchy Problem. This is not a mathematical inconsistency of the thoery. The fact that the Higgs mass estimated by dimensional analysis as in the previous section is so large does not forbid us to obtain the correct Higgs pole mass, 125 GeV. Indeed the one above is only the conttribution to the physical mass, associated with the effect of the UltraViolet particles and iteractions. As made very clear in the Wilson approach to Quantum Field Theory, $m_{phys}^2 = m_{UV}^2 + \delta^2 m$, where $\delta^2 m$ comes from radiative corrections and it is associated with physics below the cut-off Λ_{SM}. Classifying Higgs boson as fundamental scalar particle, this is not protected by large radiative correctionsm so that δm can be very large and compensate for $m_{H,UV}$. Looking Fig. 1.2a we can see the main correction at one-loop order g^2 , that comes from the largest Yukawa, that is the coupling to the top quark.The contribution to the Higgs mass 1.2a of course is not the only one, there are others from gauge bosons, Higgs itself, with different signs, but they are smaller. We compute δm^2 by regularizing the integral with a cut-off, we obtain

$$\delta m_H^2 = 3\lambda_t^2 \int_{|k|\leq\Lambda_{SM}} \frac{d^4k}{(2\pi)^4} \frac{1}{k^2} \sim -\frac{3\lambda_t^2}{2\pi^2} \left[\Lambda^2 + ...\right] \simeq 0.1\Lambda_{SM}^2 \tag{1.51}$$

The correction is quadratically divergent in the energy scales. This suggest that such a term could account for a cancellation with the first computed in the previous chapter. To quantify the precision with which the UV and IR term have to cancel, we can define

$$\Delta = \frac{\max\left[c\Lambda_{SM}^2, \delta m_H^2\right]}{m_{H,pole}^2} \geq \left(\frac{125\,\text{GeV}}{m_H}\right)^2 \left(\frac{\Lambda_{SM}}{400\,\text{GeV}}\right)^2 . \tag{1.52}$$

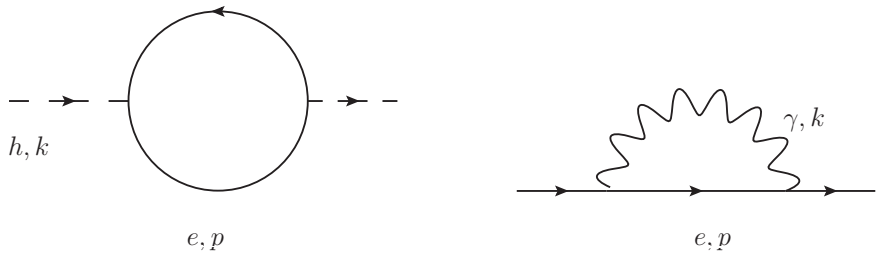

Figure 1.2: Electron self-energy 1.2a and top quark loop correction to the higgs 1.2a

Δ defines the amount of cancellation we need to reproduce the experimentally observed Higgs mass. Besides of being a trouble for the Standard Model, it ensures that some new physics has to exist below M_{GUT}.

The Hierarchy Problem regards only scalar particles, then the Higgs boson in the Standard Model. For example, let us consider the electron, that is a fermion, and let's compute its main radiative correction. Looking to Fig. 1.2b we can see the 1-loop correction to the electron self-energy, that is given by a photon loop. Using a cut-off regularization as before to renormalize our theory, we find that

$$\delta m_e = \frac{3\alpha_{em}}{4\pi} m_e \log \frac{\Lambda}{m_e} \tag{1.53}$$

In this case the dependence of the correction from the energy scale is logarithmic, than we can say that the contribution of the self-energy diagram gives a small correction to the electron mass. This is very simple understood in terms of symmetry: in the limit of vanishing mass $m_e \to 0$, the theory acquires a global chiral symmetry, the left-handed and right-handed component of the electron spinor are decoupled: the action is invariant for phase transformation:

$$\psi'_L \to e^{i\theta_L}\psi_L \qquad\qquad \psi'_R \to e^{i\theta_r}\psi_R \tag{1.54}$$

Since $m_e \neq 0$, chiral symmetry is not exact, but an approximate one, the correction to the electron mass is proportional to the fermion mass itself. Small break implies small correction. All fermion masses are protected from this mechanism, since the Standard Model is a chiral theory. So we may think that a similar mechanism based on symmetries could preserve the Higgs mass to its right value.

The existence of new physics beyond the Standard Model is suggested also by other experimental evidences, in particular the existence of Dark Matter and of neutrino masses as already discussed. Other problems arise if we try to explain baryogenesis and the existence of flavors. The power spectrum of Cosmological Microwave Background allows to extimate the density of the various components of the universe, in particular we have experimental confirm that non-baryonic (i.e. Dark Matter and Dark Energy). We have $\Omega_{non-baryonic}h^2 = 0.127^2$ and $\Omega_{baryonic}h^2 = 0.0222$ (here h^2 is the Hubble parameter) within a very precision range. This shows that the relative abundance of baryonic constituents compared to that of non-baryonics is low, confirming the fact there has to be something else in the universe. Experimental evidences for neutrino masses are given by neutrinos flavor oscillations, measured in the relative abundances of neutrinos coming from the Sun. However nowadays we have not direct information that such problem are directly related with energy scales we are going to explore at the Large Hadron Collider, let's say $4-5\,\text{TeV}$. So which are the possible scenarios? One is fine-tuning, described above: we choose the parametrizations of the model in such a way the cancellation happens. But this situation rises the *naturalness* problem: how is natural to fine-tune quantities to reach the values we want? If we want to make the cancellation

[2]Results taken from [12]; Ω_i is defined as the ratio between the density of the $i-esim$ component of the universe and critical density $\rho_c = (3H_0^2)/(8\pi G)$ - nowadays we have $\Omega_{tot} \sim 1$

accidental, we do not want a large fine-tuning too, and this argument implies that new physics have to arise at energies explored by the Large Hadron Collider. For example

$$\Delta \leq 100 \Rightarrow \Lambda_{SM} \sim 4 - 5\,\text{Tev} \tag{1.55}$$

The other possibility is that new physics arises and so new particles, new phenomena, something else that goes beyond what we actually know, could achieve the goal of canceling out these divergences.For example, one of the solution to the Hierarchy problem, studied in the last thirty years, is Supersymmetry, in which boson masses are related to their fermionic superpartners, then there is a chiral symmetry protecting from large radiative corrections. The Composite Higgs is another solution, different from SuperSymmetry. The mechanism that protect the Higgs mass in the composite scenario is dimensional trasmutation. If the Higgs is a composite state of a new-strongly interacting sector, the dimensionality of the Higgs mass operator, written in terms of the costituents of the new strong sector, is not $d = 2$, but it could be even $d > 4$, so we have not problems in explaining why the Higgs mass is relatively light. The mass is also protected by symmetry, so the radiative corrections do not implies divergences, then for example, if the Higgs is a composite state made of two fermion ψ of the new strong sector, we could write

$$dim\,[H] \sim dim\left[\bar{\psi}\psi\right] \rightarrow dim\left[H^2\right] = 6\,. \tag{1.56}$$

From the altered dimension of the field corresponding to the Higgs boson follows that correction are suppressed by powers of Λ_{SM}, and as it was for the example of the proton decay, the Higgs is protected by correction from $E \sim M_{GUT}$. All the theory so is parametrized in term of the only scale of this new strong sector, where confinement happens, as it is for the QCD theory. In this picture, all the resonances (we gloabally call ρ) must have the same mass, within a range of energy determined by an order of magnitude, for example. Then if the Higgs boson belongs to this picture, it would be surrounded by other strong resonances (of spin 1/2, 1 , 2), all at the same mass. To get a Higgs mass of about 125 GeV the energy scale of the new strong sector would be 100 GeV, and we have of course strong bounds on the production of such particles, since they would be at an energy range explored so far. For example, a large splitting between the Higgs and other spin-1 resonances is strongly suppressed by comparison with ElectroWeak Precison Test (EWPT), and such a situation would require

$$\left(\frac{m_H^2}{m_\rho^2}\right) \lesssim 1/400\,, \tag{1.57}$$

that is a large fine-tuning. However also in the QCD picture we know of particles lighter than the other resonances: these are the pions, that we construct as *pseudo-Nambu-Goldstone bosons*. This is the same feature we require for the Higgs boson in our Composite Higgs model, it has to be a pseudo-Nambu Goldstone boson coming from the spontaneous break of the global group $\mathcal{G} \rightarrow \mathcal{H}$. If the symmetry has been exact, the Higgs would be massless, instead in this way the Higgs acquires a relatively high mass, that is protected yet by the underlying Goldstone symmetry. This will be clearer in the next chapter. Small briefing is done showing how Nature behalfs in the QCD case.

Chapter 2

The Composite Higgs model

2.1 The QCD chiral lagrangian: the pion analogy

Also in QCD we have scalar particles: the pions are the lightest mesons in the mass spectra with $m_\pi \sim 100\,\mathrm{MeV}$. How are their masses protected from being close to other composite states (resonances), with $m_\rho \sim 1\,\mathrm{GeV}$? The chiral symmetry is the answer to this question. If only the two lightest quarks, u and d, are considered, the quarl sector of the QCD Lagrangian reads

$$\mathcal{L} = \sum_{j=u,d} \bar{q}_j \left(i\not{D} + m\right) q_j \,. \tag{2.1}$$

This Lagrangian is invariant under various global symmetries. The firss one is a phase transformation of the quark fields. This is the accidental baryon symmetry described above, it leads to the conservation of *baryon* number, by which we classify the hadrons in mesons and baryons.

$$q'^i \to e^{i\alpha/3} q^i \qquad\qquad B[q] = \frac{1}{3} \qquad\qquad B[\bar{q}] = -\frac{1}{3} \tag{2.2}$$

Thus the classification splits in:

- *mesons*: $B[q\bar{q}] = 0$;
- *baryons*: $B[qqq] = 1$.

Introducing a notation that manifestly shows symmetries that couple different flavours, let's write:

$$q = \begin{pmatrix} u \\ d \end{pmatrix}$$

The lagrangian becomes:

$$\mathcal{L} = \bar{q} \left(i\not{D}\right) q \,. \tag{2.3}$$

We have neglect the masses of the quarks, that are small compared to the energy scale we are dealing with. This Lagrangian is invariant under a 2×2 unitary transformation:

$$q' = exp\left[\sum_0^3 \alpha_i \sigma_i\right] q \tag{2.4}$$

$\sigma_i \,, (i = 1, 2, 3)$ are the Pauli matrices and σ_0 is the unit matrix. So this $U2_V$ is the $U(1)$ phase transformation mentioned above, composed with a $SU(2)_V$ transformation. This is an exact symmetry in the case the u and d masses are degenerated. The subscript V stays for *vectorial*, since the associated current is vectorial:

$$J^i_\mu = \bar{q}\gamma_\mu \sigma^i q \tag{2.5}$$

Decomposing the quark fields in terms of their chiral components, and negelecting the quark masses, the Lagrangian becomes

$$\mathcal{L} = \bar{q}_L i \not{D} q_L + \bar{q}_R i \not{D} q_R \tag{2.6}$$

We can note that two flavours QCD with massless quarks possesses chiral symmetry: $SU(2)_L \times SU(2)_R$. This symmetry does not appear in the observed spectrum of QCD. If it existed, every hadron must have a symmetric partner with opposite parity (since the chirality is opposite). Colour condensation (that means the operator $\bar{q}q$ has a non-zero expectation value $\langle 0| \left(\bar{u}u + \bar{d}d\right) |0\rangle \sim (250\,\mathrm{MeV})^3$) breaks down the chiral symmetry to $SU(2)_V \times U(1)_B$. The composite operator $\bar{q}q$ connects left and chiral components of the quark fields. Three generators broken implies three Nambu-Goldstone bosons, massless. We do not know something similar, but we can note that in the QCD spectrum three low-mass hadrons exist: π^0,$\pi^\pm$. The explanation for such a pattern of the spectrum is again spontaneous symmetry breaking: u and d are not massless, though their masses are very small, compared to Λ_{QCD}. In addiction, electromagnetic interactions split moreover the mass spectrum of the three pions: $\pi^\pm$ have different mass than π^0, because u and d have different charge with respect to electromagnetic interactions. These pions are particles we call pseudo Nambu-Goldstone bosons. In fact they do not come from a broken exact symmetry, but from a broken approximate one. In the appendix, we can see a formal approach for the description of the pions, the linear Σ model, that we will generalize to the case of the Composite Higgs.

2.1.1 The linear Σ model

The linear Σ model of Gell-Mann and Levy [13] was a first toy model of nuclear forces and it was subsequently applicated to the pions. We would like to describy the mass spectrum of hadrons, starting from the lighter resonances. We want to construct an effective theory valid at low energy scales - compare to the QCD scale. Then we add to the Lagrangian a set of scalar fields, that is a 2×2, we say Σ (from which the name of the model). This transforms as

$$\Sigma \to g_L \cdot \Sigma \cdot g_R^\dagger \,. \tag{2.7}$$

The Lagrangian for Σ, descending from the QCD (massless) theory, must be invariant under the chiral symmetry, with global group $SU(2)_L \times SU(2)_R$ thus the Lagrangian has the form

$$\mathcal{L}(\Sigma) = \frac{1}{4} Tr\left[\partial_\mu \Sigma^\dagger \partial^\mu \Sigma\right] - \frac{\lambda}{4}\left[\frac{1}{2} Tr\left[\Sigma^\dagger \Sigma\right] - F_\pi^2\right] . \tag{2.8}$$

Exploiting the spontaneous symmetry breaking paradigm we suppose that Σ takes a Vacuum Expectation Value, proportional to the identity

$$\langle \Sigma \rangle \equiv F_\pi \cdot \mathrm{I} \,. \tag{2.9}$$

The chiral group now has been broken down to its vectorial subgroup

$$\langle \Sigma \rangle \to g_L \langle \Sigma \rangle g_R^\dagger = F_\pi \cdot g_L g_R^\dagger = \langle \Sigma \rangle \Rightarrow g_L = g_R \,. \tag{2.10}$$

In this simple description, the Σ matrix is a complex 2×2 matrix. We can impose some restrictions to Σ, provided these are compatible with the symmetry. We impose the constraint

$$\Sigma^* = +\sigma^2 \cdot \Sigma \cdot \sigma^2 \tag{2.11}$$

where σ^2 stands for the second Pauli matrix. This constraint has been chosen because it is invariant under the transformation law of the global group

$$\Sigma \to \Sigma^{(g_L, g_R)} = g_L \Sigma g_R^\dagger \,, \tag{2.12}$$

$$\left(\Sigma^{(g_L, g_R)}\right) = \sigma_2 g_L \sigma_L \Sigma^* \sigma_2 g_R^\dagger \sigma_2 \,. \tag{2.13}$$

Obviously this works because σ_2 is one of the generators of the $SU(2)$ group. This constraint allows us to rewrite the Σ field in terms of only four scalars

$$\Sigma = \sigma(x) \cdot \mathrm{I} + \imath\sigma^a \pi_a(x)\,. \tag{2.14}$$

The matrix representation of $SU(2)_L \times SU(2)_R$ that obeys the condition in Eq. 2.11, we call it pseudo-reality condition, is referred to as a *bidoublet* $\Sigma \in (2,2)$. Under parity, the bidoublet transformation shows the σ field is a scalar, instead the three π's are pseudo-scalars. Under the isospin group, σ is a singlet and the π's transform in the adjoint. We can see the π^a have the right quantum numbers to describe the pions triplet. We rewrite

$$\pi = \pi^a \sigma^a = \begin{pmatrix} \pi^3 & \pi^1 - i\pi^2 \\ \pi^1 + i\pi^2 & -\pi^3 \end{pmatrix} \equiv \begin{pmatrix} \pi^0 & \sqrt{2}\pi^+ \\ \sqrt{2}\pi^- & -\pi^0 \end{pmatrix}. \tag{2.15}$$

Expliciting in terms of the parametrization we give of Σ, and expanding aroung Vacuum Expectation Value fluctuations, the Lagrangian in Eq. 2.8 becomes

$$\mathcal{L}(\Sigma) = \frac{1}{2}(\partial_\mu \sigma)^2 + \frac{1}{2}(\partial_\mu \pi^a)^2 - \frac{\lambda}{4}\left[\sigma^2 - F_\pi^2 + |\pi|^2\right]^2 \tag{2.16}$$

thus we have found a massive state $m_\sigma = \sqrt{\lambda} F_\pi$ and three massless states $m_\pi = 0$. The great result of Gell-Mann and Levy was that the pions can be interpreted as the Goldstone bosons associated with the spontaneous breaking of the chiral group. In this simplified description the pions are massless yet, but a little mass can be generate by a small breaking of the isospin symmetry. This is the feature before we refer to as pseudo-Nambu Goldstone nature. A similar approach is exploited for the construction of the Composite Higgs model.

2.2 Composite Higgs in short

The idea of a composite Higgs boson was first proposed in 1984 by Georgi and Kaplan [14], [15]. The model interpolates between two different paradigms, the higgless scenario, with Technicolour as reference, and the minimal Higgs mechanism, as embedded in the resent version of the Standard Model. In this scenario, the Higgs emerges as a composite psuedo Nambu-Goldstone boson, it is a bound state of a new strongly interacting sector. In this way the Hierarchy Problem is overwelmed, because the Higgs mass is protected from large Planckian corrections, by the mechanism of dimensional transmutation previously discussed. In comparison with Technicolour theories, Electroweak Precision Test are easier to satisfy thanks to the presence of the Higgs particle. As we have seen an analogous phenomenon is at work for the QCD hadrons. The pseudo Nambu-Goldstone nature of the Higgs allows it to be naturally lighter than other resonances in the strong sector, which arise at an energy scale of some TeV, compatible with present direct bounds. To make the general idea more concrete, and following more recent descriptions as [16] and [17], we must first of all define a global group $\mathcal{G}$, under which the strong sector is invariant.We assume the strong sector to confine, breaking $\mathcal{G}$ to a subgroup $\mathcal{H}$ at the scale f, the analog of the f_π constant in QCD. An $SU(2) \times U(1)$ subgroup of $\mathcal{H}_1$ is gauge by external vector fields, which will provide the Electroweak vector bosons. The global symmetry breaking $\mathcal{G} \to \mathcal{H}_1$ implies $n = dim(\mathcal{G}) - dim(\mathcal{H}_1)$ Nambu-Goldstone bosons, three of them are eaten to give mass to the Electroweak gauge bosons, while the others remain as physical scalars. Obviously for this programma to work the Standard Model group $SU(2)_L \times U(1)_Y$ must be embeddable in the unbroken one $\mathcal{H}$. Furthermore, since the presence of at least one physical Higgs scalar is required, to be identified with the Standard Model Higgs, at least one complex doublet of Goldstones must emerge from the $\mathcal{G} \to \mathcal{H}$. The non-linear realization of the symmetry implies that the Higgs potential vanishes, however the couplings of the Standard Model fields to

the strong sectorare only invariant under G_{SM} and break the complete $\mathcal{G}$. The Higgs potential can thus be generated through Standard Model gauge bosons loops, with the Coleman-Weinberg method, as described for example in [18]. Provided this potential has a non-trivial minimum, the Electroweak symmetry is broken by the Composite Higgs as in the Standard Model. It's interesting to note that in this situation, there is not only one but two scales. On top of the "Higgs decay constant" f, we also have the Electroweak Symmetry Breaking scale v. From the ratio among the two scales we can convenientrly define $\xi = (v/f)^2$. The scale f controls the mass of the other strong sector resonances, besides the Higgs. By Naive Dimensional Analysis we can estimate the masses $m_\rho \sim g_\rho f$ with $1 \leq g_\rho \leq 4\pi$ the coupling constant of the strong sector, while the mass of the Higgs is set by $m_H \sim g_{SM} v$, with g_{SM} any of the Standard Model coupling [1]. Furthermore, as in the pion example given above, all the higher dimensional operators involving additional powers of the Higgs field are suppressed as they appear as H/f. In this way, the limit of $f \to \infty$, or $\xi \to 0$ is the situation in which the Higgs remains lights and the other resonances get infinitely heavy. Moreover the effects associated with the Goldstone Nature of the Higgs decouple and the theory reduces to the Standard Model. In this framework the potential itself compares as a function of H/f, then we would have naturally $\xi \sim 1$. Small ξ makes the scenario less plausible, with fine-tuning to restore the validity of the model. A suitable choice could be $\xi \leq 0.2$.

2.3 The minimal coset $SO(5)/SO(4)$

The *minimal coset* for the Composite Higgs is defined by a global group

$$\mathcal{G} = SO(5) \times U(1)_X \tag{2.17}$$

where the $U(1)_X$ factor is needed to reproduce the correct fermion hypercharges. $\mathcal{G}$ is broken to

$$\mathcal{H}_1 = SO(4) \times U(1)_X \,. \tag{2.18}$$

Any $SO(4)$ vector $v^{\hat{a}}$, transforming as

$$SO(4): \qquad v^{\hat{a}} \to S^{\hat{a}\hat{b}} v^{\hat{a}} \qquad |v| \equiv constant \tag{2.19}$$

is isomorphic to a matrix $V \equiv \bar{\sigma}^{\hat{a}} v^{\hat{a}}$ with $\sigma^{\hat{a}}$ the three standard Pauli matrices and the identity. We know from the theory of Lie groups that $SO(4) \sim SU(2)_L \times SU(2)_R$ in the sense that they have the same algebra. The action of $SU(2)_L \times SU(2)_R$ can be defined on the matrix V as the left multiplication by $L \in SU(2)_L$ and right multiplication by $R \in SU(2)_R$, so that $det(V)$ is left unchanged:

$$SU(2)_L \times SU(2)_R: \qquad V \to L V R^\dagger \qquad det(V) == |v^2| = constant \tag{2.20}$$

For each element of $SO(4)$ two $SU(2)_L \times SU(2)_R$ transformations act in the same way on V:

$$S \to (L, R), (-L, -R) \tag{2.21}$$

That implies:

$$SO(4) = \frac{SU(2)_L \times SU(2)_R}{\mathrm{Z}_2} \tag{2.22}$$

Up to the discrete Z_2 (which identifies the second power of an element with its inverse - it is a reflection) the two groups has the same algebra. Since $\mathcal{H} \equiv SO(4) \sim SU(2)_L \times SU(2)_R \times U(1)_X$, the Standard Mode group is embeddable in $\mathcal{H}$ by identifying $SU(2)_L$ with the Standard Model one and the hypercharge with $Y = T^3_R + X$.

[1] The precise scaling of the Higgs mass with the couplings is actually a model-dependent question. However the scaling with v is robust

2.3.1 Some notations

The Standard Model gauge fields are inserted as external sources, they are not part of the strong sector. They couple to the strong sector by gauging the generators of $SO(4)$ that corresponds to the Standard Model group. We denote the $SO(5)$ generators as

$$T^A = \{T^a, T^{\hat{a}}\}\,, \qquad [T^A, T^B] = if^{ABC}T^C\,, \qquad Tr[T^A T^B] = \delta^{AB} \tag{2.23}$$

where $A = 1, ..., 10$ is the $SO(5)$ adjoint index , T^a and $T^{\hat{a}}$ are the unbroken and broken generators respectively, so that

$$a = 1, ..., dim[SO(4)] = 1, ..., 6\,, \tag{2.24}$$

$$\hat{a} = 1, \cdots, dim[SO(5)] - dim[SO(4)] = 1, ..., 4\,. \tag{2.25}$$

A suitable basis for the $SO(5)$ generators is

$$T^{a,L,R}_{A,B} = -\frac{i}{2}\left[\frac{1}{2}\epsilon^{abc}(\delta^b_A\delta^c_B - \delta^b_B\delta^c_A)) \pm (\delta^a_A\delta^4_B - \delta^a_B\delta^4_A)\right] \tag{2.26}$$

$$T^{\hat{a}}_{AB} = -\frac{i}{\sqrt{2}}(\delta^b_A\delta^5_B - \delta^{\hat{a}}_B\delta^5_A) \tag{2.27}$$

By the Goldstone theorem we know that the representation $\mathcal{R}_\pi$ in which the Goldstone transform is obtained from the decomposition

$$Adj[\mathcal{G}] = Adj[\mathcal{G}] \oplus \mathcal{R}_\pi \tag{2.28}$$

In our case

$$[T^a, T^b] = if^{abc}T^c + i\cancel{f^{abc}}T^{\hat{c}} \tag{2.29}$$

$$[T^a, T^{\hat{b}}] = if^{a\hat{b}\hat{c}}T^{\hat{c}} + i\cancel{f^{a\hat{b}c}}T^c \tag{2.30}$$

$$[T^a, T^b] = i\left(t^a_{Adj[SO(4)]}\right)^b_c T^c \tag{2.31}$$

$$[T^a, T^{\hat{b}}] = i\left(t^a_{\mathcal{R}_\pi}\right)^{\hat{b}}_{\hat{c}} T^{\hat{c}} \tag{2.32}$$

where $t^a_{\mathcal{R}_\pi}$ is the $\underset{\sim}{4}$ representation, $\pi \in \underset{\sim}{4}$. We can see that using the pattern $SO(5) \to SO(4)$ we find exactly one Higgs boson doublet, that is what we would reproduce.

2.3.2 The Callan-Coleman-Wess-Zumino construction

In [19] and [20] Callan Coleman Wess and Zumino studied the general structure of phenomenological Lagrangian and how they can be constructed for a generic spontaneously broken (non-linearly realized) symmetry group. The main result was to prove that the transformations induced by the group on the manifold of the phenomenological fields can be put in a standard forms.The mathematical problem is equivalent to that of finding all (nonlinear) realizations of a (compact, connected, semisimple) Lie group which become linear when restricted to a given subgroup. Let us consider a generic multiplet of the group $\mathcal{G}(SO(5)$ in our special case) $\mathcal{O}$, whose Vacuum Expectation Value $\langle \mathbf{O} \rangle = \mathbf{v}$ breaks the global symmetry group to $\mathcal{H}$ (i.e., $SO(4)$ in our case). TH $U(1)_X$ factor is not spontaneously broken, so we can safely ignore it in this discussion. Then

$$T^a\mathbf{v} = 0\,, \qquad T^{\hat{a}}\mathbf{v} \neq 0\,. \tag{2.33}$$

The massless particles of the theory must correspond to the fluctuations of $\mathbf{O}$ in the direction of the global symmetry group. This leads to an ansatz

$$\mathbf{O}_{ansatz}(\mathbf{x}, t) = U(\mathbf{x}, t)\cdot\mathbf{v}\,, \qquad U(\mathbf{x}, t) \equiv e^{i\alpha_A(\mathbf{x},t)T^A)} \in \mathcal{G}\,. \tag{2.34}$$

We exploit the field matrix U to construct the effective Lagrangian, which must respect the $\mathcal{G}$ symmetry like the original one. On U, $\mathcal{G}$ acts as

$$U \to U^{(g)} = gU\,, \qquad \mathbf{O} \to g\mathbf{O}\,. \tag{2.35}$$

However, the ansatz in 2.34 also displays a local invariance. It indeed remains unchanged if we transform

$$U \to U^{(h(x)} = U \cdot h(x)\,, \qquad \mathbf{O} \to Uh^{\dagger}(x) \cdot \mathbf{v} \tag{2.36}$$

if $h(x) = e^{i\alpha_a(x)T^a}$ is a local translation in the unbroken group $\mathcal{H}$. Therefore, U offers a redoundant parametrization, $U^{(h(x))}$ is equivalent to U because it corresponds to the same field fluctuation. The *physical* Goldstones are not described by U spanning the entire group, but only by a coset space

$$\mathcal{G}/\mathcal{H} \equiv [g]_{\mathcal{H}}; g \in G \tag{2.37}$$

with the equivalence relation given by $U \sim U \cdot h^{\dagger}$. In order to describe only the physical degree of freedom we fix the gauge symmetry of 2.36,restricting U to have the form

$$U(\mathbf{x}, t) \equiv e^{i\sqrt{2}/f\pi_{\hat{a}}(\mathbf{x},t)T^{\hat{a}}}\,. \tag{2.38}$$

The matrix U, with this restriction, is called the Goldstone matrix. Its transformation property is now

$$U^{[\pi]} \to U^{(g),[\pi]} = gU^{[\pi]}h^{\dagger}[\pi, g]\,. \tag{2.39}$$

Using only g to transform the Goldstone matrix would introduce again the unphysical fields α_a this is compenstate by right multiplication with a h element. This particular transformation for U corresponds in general to a non-homogeneus and extremely complicated transformation rule for the Goldstone fields π. Using the U matrx, for which the transformation is simpler provides a considerable simplifiction. After writing the phenomenological $\mathcal{L}$ in terms of U we will compute the Goldstone interactions by expanding the exponential the the aprpropriate order. Although it is a *non-linear* realization, h obeys the $\mathcal{G}$group multiplication rule:

$$h[\pi, g_2 \cdot g_1] = h[\pi^{g_1}, g_1] \cdot h[\pi^{g_2}, g_2]\,, \tag{2.40}$$

thus it provides a valid (though non-linear) representation. An important (and interesting) feature of all this construction is the fact that if $g \in \mathcal{H}$ the transformation law for the π's returns linear

$$g_h \cdot U = g_h \cdot e^{i\sqrt{2}/f\pi_{\hat{a}}T^{\hat{a}}} = exp\left[i\sqrt{2}/f g_h \pi_{\hat{a}} T^{\hat{a}} g_h^{\dagger}\right] \cdot g_h = U\left[\pi^{(g_h)}\right] \cdot g_h \tag{2.41}$$

that is the transformation we called $\mathcal{R}_{\pi}$ in the previous section

$$\pi_{\hat{a}}T^{\hat{a}} = g_h\left(\pi_{\hat{a}}T^{\hat{a}}\right)g_h^{\dagger}\,. \tag{2.42}$$

2.3.3 Construction of the effective Lagrangian

We introduce the two symbols e_μ and d_μ defined by decomposing the Maurer-Cartan form on the unbroken and broken generators, respectively

$$iU^{\dagger}\partial_\mu U \equiv -d_\mu^{\hat{a}}T^{\hat{a}} - e_\mu^a T^a \tag{2.43}$$

Under a group symmetry transformation, the Maurer-Cartan form transform

$$iU^{\dagger}\partial_\mu U \to ih \cdot U^{\dagger}\partial_\mu[U \cdot h^{\dagger}] \tag{2.44}$$

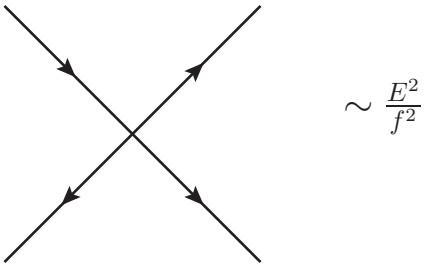

Figure 2.1: Main prediction of the effective Lagrangian

Applying this equation to our two symbols, we can see that

$$d_\mu^{\hat{a}} T^{\hat{a}} \to h d_\mu^{\hat{a}} T^{\hat{a}} h^\dagger \tag{2.45}$$

instead

$$e_\mu^a T^a \to h e_\mu^a T^a h^\dagger - i h \partial_\mu h^\dagger \tag{2.46}$$

The transformation of the e_μ symbol is the analog of a gauge field transformation property. Because of this, we can use it to construct field-strenght and covariant derivatives in the Lagrangian. The transformation of d_μ is instead linear in h, with no additional shift. Using only the Goldstones in our Lagrangian, the lowest dimensional term is

$$\mathcal{L}_\pi^{d=2} = \frac{f^2}{4} d_\mu^{\hat{a}} \cdot d_\mu^{\hat{a}} \tag{2.47}$$

The dimension is given by the power counting: the d_μ contains one derivative, that is $[\partial_\mu] = [1]$ in natural units ($c = h = 1$). The constant is defined to canonically normalize the fields in the Lagrangian. With this Lagrangian we can construct all the effective vertices with E_π external legs, from which we have an extimate of the Goldstones scattering. The expansion of the U matrix gives infinite terms, then we have infinite interactions, all of them with two derivatives and an arbitrary number of π external legs. The interesting feature is that the f parameter completely controls the interactions among the Goldstone, and this is a powerful implication. A general form for the interaction has the form

$$f^2 \partial \frac{\pi}{f} \cdot \partial \frac{\pi}{f} \cdot \left(\frac{\pi}{f}\right) \cdot \ldots \cdot \left(\frac{\pi}{f}\right) \Rightarrow P^2 f^2 \cdot \left(\frac{1}{f}\right)^{E_\pi} \tag{2.48}$$

where the last implication follows from the Feynman rules; E_π is the number of external legs in the diagram we are considering. In Fig. 2.1 there is an exemplification. We have to note that higher terms are suppressed by powers of the f parameter, since each Goldstone field carries a factor $1/f$ from the expansion of the exponential.

2.3.4 Bosonic sector: gauge fields

As we have seen, the coset $SO(5)/SO(4)$ implies four real Nambu-Goldstone bosons transforming as a fundamental of $SO(4)$, or equivalently as a doublet of $SU(2)_L$. The doublet H is the composite Higgs. Recalling what we have said in 2.1.1 about the $SU(2)$ representations, we can define a suitable representation for our Higgs field. Under an $SU(2)_R$ rotation it mixes with its conjugate $H^c = i\sigma^2 H^*$. Thus it forms a bidoublet of $SU(2)_L \times SU(2)_R$, (H, H^c). This is an important result, in particular when we have to write the Yukawa's in the Standard Model Lagrangian, the Higgs is

already in a suitable form to write the interaction terms. Going to the matrix notation of $SO(4)$, we can parametrize the fourplet $\pi^{\hat{a}}$ in terms of the complex doublet Higgs H as

$$\pi = \frac{1}{\sqrt{2}} \begin{pmatrix} -i(h_u - h_u^\dagger) \\ h_u + h_u^\dagger \\ i(h_d - h_d^\dagger) \\ h_d + h_d^\dagger \end{pmatrix} \tag{2.49}$$

with $H = (h_u, h_d)$ the Standard Model Higgs doublet. In the unitary gauge this vector takes a simple form

$$h_u = 0 \qquad h_d = \frac{\langle H^0 \rangle + h}{\sqrt{2}} \qquad \pi = \begin{pmatrix} 0 \\ 0 \\ 0 \\ \langle H^0 \rangle + h \end{pmatrix} \tag{2.50}$$

With the generators in Eq. 2.27, the Goldstone matrix reads:

$$U[\pi] = \exp\left[i \frac{\sqrt{2}}{f} \pi_{\hat{a}} T^{\hat{a}} \right] = \begin{pmatrix} \mathrm{I}_4 - \frac{(1-cos(\pi/f))}{\pi^2} \pi \cdot \pi^t & \frac{sin(\pi/f)}{\pi} \pi \\ -\frac{sin(\pi/f)}{\pi} \pi^t & cos(\pi/f) \end{pmatrix}, \tag{2.51}$$

where $\pi = \sqrt{\pi \cdot \pi^t}$. In the unitary gauge it becomes

$$U = \begin{pmatrix} 1 & 0 & 0 & 0 & 0 \\ 0 & 1 & 0 & 0 & 0 \\ 0 & 0 & 1 & 0 & 0 \\ 0 & 0 & 0 & cos(H^0/f) & -sin(H^0/f) \\ 0 & 0 & 0 & cos(H^0/f) & cos(H^0/f) \end{pmatrix}. \tag{2.52}$$

and the d_μ symbol is easiliy computed as

$$d_\mu^{\hat{a}} = \frac{\sqrt{2}\pi^{\hat{a}}}{\pi^2} \left(\frac{1}{f} - \frac{sin(\pi/f)}{\pi} \right) \pi \cdot \partial_\mu \pi + \frac{\sqrt{2}}{\pi} sin(\pi/f) \partial_\mu \pi^{\hat{a}} \,. \tag{2.53}$$

We should now couple the Goldstone to the Standard Model gauge fields, to this end we define the covariant derivatives

$$\partial_\mu \pi^{\hat{a}} \to D_\mu \pi \hat{a} = \partial_\mu \pi^{\hat{a}} - i A_\mu^a \, (t^a)_{\hat{b}}^{\hat{a}} \, \pi^{\hat{b}} \tag{2.54}$$

where

$$A_\mu^a t^a = \frac{g}{\sqrt{2}} W_\mu^+ (t_L^1 + i t_L^2) + \frac{g}{\sqrt{2}} W_\mu^- (t_L^1 - i t_L^2) + g(c_W Z_\mu + s_W A_\mu) t_L^3 + g'(c_W Z_\mu - s_W A_\mu) t_R^3 \tag{2.55}$$

Using 2.53 in 2.47, we find

$$\mathcal{L}_\pi = \frac{1}{2} (\partial_\mu H^0 \partial^\mu H^0) + \frac{g^2}{4} f^2 \sin^2(H^0/f) \left(|W|^2 + \frac{1}{2c_W^2} Z^2 \right). \tag{2.56}$$

Using the pole-mass of the Z boson to set the value of the Vacuum Expectation Value, i.e. $v = 246\,\mathrm{GeV} = f \sin\left(\frac{\langle H^0 \rangle}{f}\right)$, we can note that f is the unique free parameter that enters the Lagrangian in Eq. 2.56, completely controling the couplings to the Standard Model gauge fields. The Standard Model relation, $\rho = M_W/(M_Z \cos\theta_W) = 1$ is authomatically satisfied, thanks to the global $SO(4)$ symmetry, as a result of the spontaneous symmetry break. Fluctuations around the Vacuum

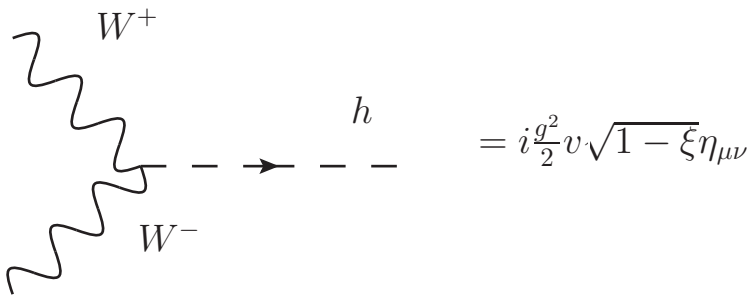

Figure 2.2: Gauge bosons - Higgs coupling in the Composite Higgs model

Expectation Value of the Composite Higgs give the couplings of the physical Higgs with pair of gauge bosons VV

$$f^2 \sin^2 \frac{\left(\langle H^0 \rangle + h\right)}{f} = f^2 \left[\sin^2\left(\frac{\langle H^0 \rangle}{f}\right) + 2\sin\left(\frac{\langle H^0 \rangle}{f}\right)\cos\left(\frac{\langle H^0 \rangle}{f}\right)\left(\frac{h}{f}\right) + \mathbf{O}(h^2)\right] = \\ = v^2 + 2v\sqrt{1-\xi}h \tag{2.57}$$

where $\xi \equiv \frac{v^2}{f^2} = \sin^2\left(\langle H^0 \rangle\right)$, thus the modification in the coupling (with respect to the Standard Model one) is: In the limit $f \to \infty$, that is the situation of a renormalizable Lagrangian with higher operators suppressed by inverse power of f, we find the Standard Model again. All the non-linearities are suppressed.

The Electroweak Precision Tests are a powerful tool to study the validation of the Standard Model and in providing directions for the search of new physics, precision experiments are needed to compare the deviations from the theoretical Standard Model predictions. Peskin and Takeuchi [21] construct a set of three observables, S,T and U, with which we can study these deviations. If new physics exist, we can compute at a radiative order, the deviation of the gauge-boson propagator terms, i.e. from *oblique* corrections. We just derive the interaction vertices of the Higgs with the gauge bosons, and combining the Peskin-Takeuchi parameters with the ElectroWeak Precision Test, we obtain

$$\Delta\hat{T} = -\frac{3g'^2}{64\pi^2}\xi log\left(\frac{\Lambda^2}{m_H^2}\right) \leq 0.3 \times 10^{-3} \tag{2.58}$$

$$\Delta\hat{S} = \frac{g^2}{192\pi^2}\xi log\left(\frac{\Lambda^2}{m_H^2}\right) \leq 2 \times 10^{-3}\,, \tag{2.59}$$

from which we can extimate $\xi \leq 0.05$. Anyway this is not a complete extimation, because we expect contributions to $\Delta\hat{T}$ from other fermionic resonances too, in particular from the partners of the top quark. From now beyond we will describe a scenario with $\xi \sim 0.2$, that is a reasonable one.

2.3.5 Fermionic sector and matter contents

Gauge fields of the Standard Model were introduced as external sources of the new strong sector. We introduced elementary fields that gauge the weak Standard Model group, this corresponds to linear interaction of the Standard Model elementary gauge fields with the composite current operators in the strong sector, as depicted in Fig. 2.3. This is a procedure currently used in the Standard Model too, for example when we write the interaction among the QCD quarks with the photon. To couple fermionic matter to the new strong sector we can similarly postulate that the

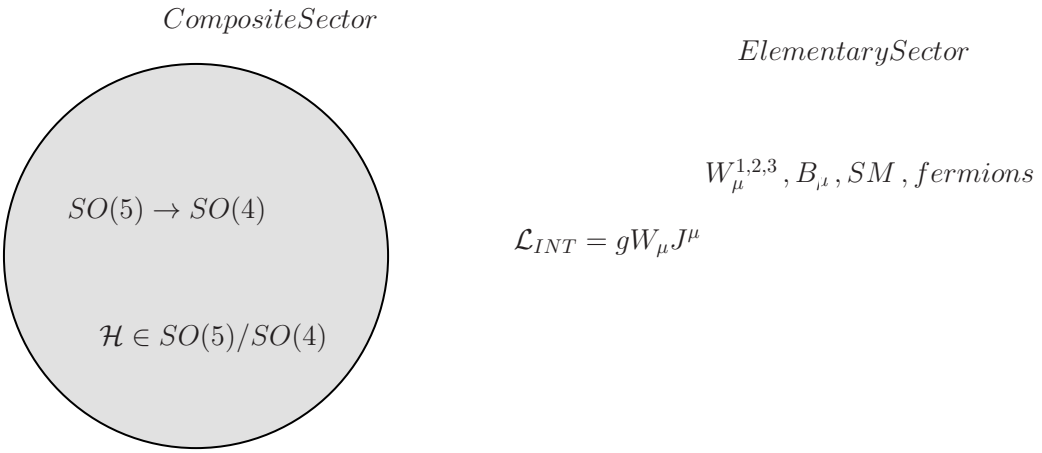

Figure 2.3: Cartoon of the gauging of the Standard Model fields

UV completion of the Standard Model generates *linear* coupling at Λ_{SM} scale.Therefore we assum the elementary-composite interaction to take the form

$$\mathcal{L}_{INT} = y_L \bar{q}_L \mathbf{O}_L + y_R \bar{q}_R \mathbf{O}_R + h.c.\,. \tag{2.60}$$

This assumption is called *partial compositeness*. This mechanism is convenient as it offers a natural protection against large Flavor Changing Neutral Current (FCNC), see [22] for a review. From Eq. 2.60 we can predict the Higgs coupling to fermion using the non-linearly realized symmetry, provided we specify how the $\mathbf{O}_{R,L}$ transform under the global group $SO(5)$. Let us write Eq. 2.60 more explicitely as

$$\mathcal{L}_{INT} = y_L \bar{q}_L \mathbf{O}_L + y_R \bar{t}_R \mathbf{O}_L + y'_R \bar{b}_R \mathbf{O}'_R + y'_L \bar{q}_L \mathbf{O}'_L\,, \tag{2.61}$$

where we coupled the q_L doublet to two different operators because this will be needed to give mass both to the top and to the bottom type quarks. There are different choices for the dimensionality of the representation of the operators that couple to the elementary fields, $\mathbf{O}_L, \mathbf{O}_R, \mathbf{O}'_L, \mathbf{O}'_R \in \underset{\sim}{1}, \underset{\sim}{4}, \underset{\sim}{5}, \underset{\sim}{10}, \underset{\sim}{14}$. We will describe the simplest, that is the $\underset{\sim}{5}$. First of all, in order to satisfy the symmetries of the Standard Model groups, $\mathbf{O}_L$ must contain a $2_{1/6}$, to be mixed with q_L, $\mathbf{O}_R$ instead must contain a $1_{2/3}$ and so on. The decomposition of the $\underset{\sim}{5}$ of $SO(5)$ under $SO(4)$ and under $SU(2)_L \times U(1)_X$ reads

$$\underset{\sim}{5} = (\underset{\sim}{2}, \underset{\sim}{2}) \oplus \underset{\sim}{1} = \underset{\sim}{2}_{1/2} \oplus \underset{\sim}{2}_{-1/2} \oplus \underset{\sim}{1}_0 \tag{2.62}$$

from which we finally understand why we need to consider the extra $U(1)_X$, f $Y = T_{3L}$ we would not be able to find the correct Standard Model hypercharge. Instead, since $Y = T_R^3 + X$, we can assign X charge equal to $2/3$ to the top-like quarks and $-1/3$ to bottom-like ones. The decomposition now reads

$$\mathbf{O}_L \,\text{and} \mathbf{O}_R \in \underset{\sim}{5}_{2/3} = \underset{\sim}{2}_{7/6} \oplus \underset{\sim}{2}_{1/6} \oplus \underset{\sim}{1}_{2/3} \tag{2.63}$$

$$\mathbf{O}'_L \,\text{and} \mathbf{O}'_R \in \underset{\sim}{5}_{-1/3} = \underset{\sim}{2}_{1/6} \oplus \underset{\sim}{2}_{-5/6} \oplus \underset{\sim}{1}_{-1/3}\,. \tag{2.64}$$

In order to exploit the implications of the symmetries, we rewrite Eq. 2.61 as

$$\mathcal{L}_{INT} = yQ^I \mathbf{O}_I + yT^I \mathbf{O}_I + yB^I \mathbf{O}_I\,, \tag{2.65}$$

where Q, T and B are the "embeddings", defined as

$$Q_L = \frac{1}{\sqrt{2}} \begin{pmatrix} b_L \\ -ib_L \\ t_L \\ it_L \\ 0 \end{pmatrix} \qquad ; \qquad T_R = \begin{pmatrix} 0 \\ 0 \\ 0 \\ 0 \\ t_R \end{pmatrix} \tag{2.66}$$

$$Q'_L = \frac{1}{\sqrt{2}} \begin{pmatrix} t_L \\ it_L \\ -t_L \\ it_L \\ 0 \end{pmatrix} \qquad ; \qquad B_R = \begin{pmatrix} 0 \\ 0 \\ 0 \\ 0 \\ b_R \end{pmatrix} . \tag{2.67}$$

When integrating out the strong sector, and thus ignoring loop corrections of the elementary fields, we can treat the embedding fields as non-dynamical external sources, and exploit the fact that $\mathcal{L}_{INT}$ is prefectly invariant under $SO(5)$, which acts as

$$Q^I_L \to g^I_J Q^I_L \qquad ; \qquad T^I_R \to g^I_J T^I_R \tag{2.68}$$

and analogous for the others. At this point we remind that in our effective Lagrangian the Goldstone matrix transform as follows

$$U_{I\bar{\imath}} \to g^J_I U_{J\bar{\jmath}} \, (h[\pi, g])^{\bar{\jmath}}_{\bar{\imath}} \ . \tag{2.69}$$

Here the first index of U, I, transforms in the fundamental of $SO(5)$, and it can be contracted with the embeddings. Instead $\bar{I}$ transforms with $h \in SO(4)$, then it is not a $SO(5)$ index. The matrix h is block-diagonal

$$h = \begin{pmatrix} h_4 & 0 \\ 0 & 1 \end{pmatrix} \tag{2.70}$$

therefore $\bar{I}$ can be splitted in $\bar{I} = \bar{\imath}, 5$. The matrix U can be decomposed as

- $U_{I\bar{\imath}}$ with I on the $\underset{\sim}{5} \in SO(5)$, $\bar{\imath}$ instead to the $\underset{\sim}{4}$ of $SO(4)$;
- U_{I5} with $I \in \underset{\sim}{5}$ and the second index in the singlet of the $SO(4)$.

We can construct invariants starting from the embeddings and the Goldstone matrix. For example we can contract the index in the fundamental of $SO(5)$

$$Q^I_L U_{I\bar{\imath}} \, , \, T^I_R U_{I\bar{\imath}} \in \underset{\sim}{4} \tag{2.71}$$

$$Q^I_L U_{I5} \, , \, T^I_R U_{I5} \in \underset{\sim}{1} . \tag{2.72}$$

This gives two fermion bilinears

$$B_1 = (\bar{Q}_L \cdot U)_{\bar{\imath}} (T_R \cdot U)_{\bar{\imath}} \qquad B_2 = (\bar{Q}_L \cdot U)_5 (T_R \cdot U)_5 \tag{2.73}$$

which however are not indipendent each other

$$B_1 + B_2 = \bar{Q}^I_L U_{I\bar{\imath}} U^t_{\bar{\imath}I} T^J_R + \bar{Q}^I_L U_{I5} U^t_{5I} T^J_R = \bar{Q}^I_L T^I_R \tag{2.74}$$

where we have used the fact that $U_{I\bar{I}} U^t_{\bar{I}J} = \delta_{IJ}$ (orthogonality) and the fact that the two embeddings are orthogonal. These operators are the most relevant ones at low energy, then for simplicity

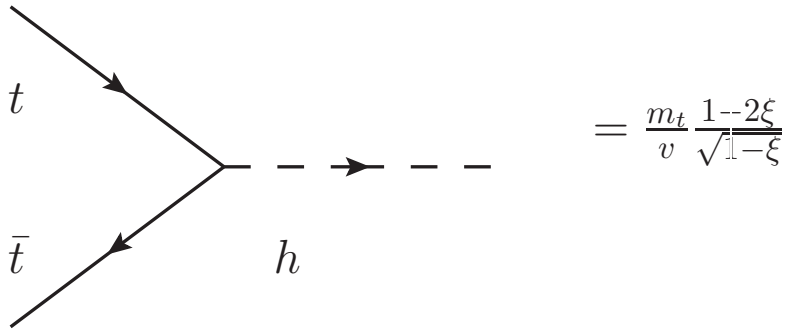

Figure 2.4: Fermion couplings in the Composite Higgs model

we consider only them in our classification. Writing the U matrix in the unitary gauge we are immediately able to compute the non-derivative terms between fermions and Higgs

$$U = \begin{pmatrix} 1 & 0 & 0 & 0 & 0 \\ 0 & 1 & 0 & 0 & 0 \\ 0 & 0 & 1 & 0 & 0 \\ 0 & 0 & 0 & c_H & -s_H \\ 0 & 0 & 0 & s_H & c_H \end{pmatrix} \qquad c_H = \cos\left(\frac{H^0}{f}\right) . \tag{2.75}$$

Now we can write the interaction Lagrangian

$$\mathcal{L}_{INT} = y_L y_R \frac{c}{2} \sin\left(\frac{2H^0}{f}\right) \bar{t_L} t_R + y'_L y'_R \frac{c'}{2} \sin\left(\frac{2H^0}{f}\right) \bar{b_L} b_R \, . \tag{2.76}$$

where te estimate of the coefficients is done with the power-counting rule of ref. All the non-derivative terms are controled by the parameters c and c' and by the same trigonometric function in the coupling. So the deviation is universal for all quarks. This is not a generic feature of all the models. Let's compute the Higgs coupling to top and bottom quarks. In order to reproduce the top and bottom mass, we have to fix y_L , y_R

$$m_t = y_L y_R \frac{c}{2} \sin\left(\frac{2H^0}{f}\right) = y_L y_R c \sqrt{\xi}\sqrt{1-\xi} \tag{2.77}$$

$$m_b = y'_L y'_R c' \sqrt{\xi}\sqrt{1-\xi} \, . \tag{2.78}$$

Next, we have to expand $H^0 = \langle H^0 \rangle + h$ obtaining

$$\sin\left(\frac{2H^0}{f}\right) = \sin\left(\frac{2\langle H^0\rangle}{f}\right) + \frac{2}{f}\cos\left(\frac{2\langle H^0\rangle}{f}\right) \cdot h = \sin\left(\frac{2\langle H^0\rangle}{f}\right) + \frac{2}{f}(1-2\xi) \cdot h \, . \tag{2.79}$$

In Fig. 2.4 we can see the interaction vertices. Event though the experimental error is too large for computing directly the modification in the Higgs coupling to fermions, this could be a powerful tool to test the Composite Higgs scenario. An experimental study of two Higgs production, is visible at the Large Hadron Collider could be an interesting process for this purpose.

Chapter 3

Top partners at the Large Hadron Collider

3.1 The Model

We have just derived the couplings between the Composite Higgs and the Standard Model fermions and gauge bosons. Now we want to study the particles that arise from the new strong sector. These fields mix with the elementary one we trated in the previous chapter, giving several phenomena to be directly exploit to test the Composite Higgs model. We will follow the derivation in [23]. After the strong sector condenses, the composite operators in eq. 2.61 correspond to particles, whose quantum numbers can be read from the decomposition in representation of the unbroken $SO(4)$ group. These are vector-like colored fermions called "partners" of the Standard Model quarks. In particular, the partners of the top quark, the *top partners*, play a particularly important role in the Composite Higgs scenario, because they control the generation of the Higgs potential [18]. These particles, since they couples directly to the Higgs, enter in the computation of the radiative corrections to the Higgs mass term,so they could help in the resolution of the Hierarchy Problem. Recalling the fine-tuning definition in Eq. 1.52, we can roughly write

$$\Delta = \left(\frac{125\,\mathrm{GeV}}{m_H}\right)^2 \left(\frac{m_{partner}}{400\,\mathrm{GeV}}\right)^2 . \tag{3.1}$$

In any reasonable model with low fine-tuning, i.e. $\Delta \simeq 10$, a first extimation with 3.1 gives $m_{partner} \sim 1.3\,\mathrm{TeV}$, that is a mass range visible at the Large Hadron Collider.

Explicitely, we will work on the first row of Eq. 2.64. We have seen that the operator $\mathbf{O}$, that lives in the fundamental of $SO(5)$, can be decomposed in representation of the unbroken $SO(4)$ group. The linear coupling in fact breaks the global group invariance $SO(5) \times U(1)$, though it preserves the invariance of the Standard Model groups. As we said, the decomposition is $\underset{\sim}{5} = \underset{\sim}{4} \oplus \underset{\sim}{1}$. We will focus our considerations on the top partner in the singlet, we will call it $\tilde{T}$. The model with the fourplet is more complicated only for the transformation property $\psi_i \to h(\pi, g)_i^j \psi_j$, but it is absolutely analogous to this we are going to describe. The Lagrangian reads

$$\mathcal{L}^{\underset{\sim}{1}} = \bar{q}_L i \not{D} q_L + \bar{t}_R i \not{D} t_R + i\bar{\psi} \not{D} \psi - M_\psi \bar{\psi}\psi + \left[y f \bar{Q}_L^I U_{I5} \psi_R + y c_2 f \bar{Q}^I U_{I5} t_R + h.c. \right] \tag{3.2}$$

where the covariant derivatives are defined as

$$D_\mu q_L = \left(\partial_\mu - igW_\mu^a \frac{\sigma^a}{2} - i\frac{1}{6}g' B_\mu - ig_S A_\mu\right) q_L \,, \tag{3.3}$$

$$D_\mu t_R = \left(\partial_\mu - i\frac{2}{3}g' B_{mu} - ig_S A_\mu\right) t_R \,, \tag{3.4}$$

$$D_\mu \psi = \left(\partial_\mu - i\frac{2}{3}g' B_\mu - ig_S A_\mu\right) \psi \tag{3.5}$$

where sum over QCD indices is understood. The top-partners form a colour triplet. In the Lagrangian in Eq. 3.2 there could be a direct term of interaction among the top-partner field and the t_R, but a simple redefinition of the fields would absorb it, since the two fields have the same quantum numbers. Apart from f, this model depends only on the three parameters $\{M_\psi, y, c_2\}$. As we have seen in Eq. 2.78, one of this has to be fixed in order to reproduce the right top mass, then, for a given top-partner mass, we have only one free parameter to set, i.e. c_2. All the parameters can be made real by chiral rotations, without need of imposing CP symmetry.

The last two terms in Eq. 3.2 can be written in matrix form, obtaining a mass matrix

$$\frac{1}{\sqrt{2}} \begin{pmatrix} \bar{t}_L \\ \bar{\tilde{T}}_L \end{pmatrix}^t \begin{pmatrix} \frac{c_2 y f}{\sqrt{2}}\sqrt{\xi} & y f \sqrt{\xi} \\ 0 & M_\psi \end{pmatrix} \begin{pmatrix} t_R \\ \tilde{T}_R \end{pmatrix} \,, \tag{3.6}$$

that can be diagonalized with a chiral rotation of the fields

$$\begin{pmatrix} \cos\theta_L & \sin\theta_L \\ -\sin\theta_L & \cos\theta_L \end{pmatrix} \begin{pmatrix} \frac{c_2 y f}{\sqrt{2}}\sqrt{\xi} & y f \sqrt{\xi} \\ 0 & M_\psi \end{pmatrix} \begin{pmatrix} \cos\theta_R & -\sin\theta_R \\ \sin\theta_R & \cos\theta_R \end{pmatrix} = \begin{pmatrix} m_t & 0 \\ 0 & M_{\tilde{T}} \end{pmatrix} \,. \tag{3.7}$$

that in this way mixes the elementary field t with the composite $\tilde{T}$. The chiral rotation of the states in Eq. 3.7 of course implies a modification in the couplings of the Lagrangian, in particular we can better understand how partial compositeness work. The chiral rotation

$$\begin{pmatrix} t_L \\ \tilde{T}_L \end{pmatrix} \to \begin{pmatrix} c_L & -s_L \\ s_L & c_L \end{pmatrix} \begin{pmatrix} t_L \\ \tilde{T}_L \end{pmatrix} \tag{3.8}$$

$$\begin{pmatrix} t_R \\ \tilde{T}_R \end{pmatrix} \to \begin{pmatrix} c_R & -s_R \\ s_R & c_R \end{pmatrix} \begin{pmatrix} t_R \\ \tilde{T}_R \end{pmatrix} \tag{3.9}$$

modifies the Standard Model doublet mixing the elementary and composite states, thus becoming

$$q_L \to \begin{pmatrix} c_L t_L + s_L \tilde{T}_L \\ b_L \end{pmatrix} \,, \tag{3.10}$$

$$t_R \to c_R t_R + s_L \tilde{T}_R \,, \tag{3.11}$$

$$\tilde{T}_L \to s_L t_L + c_L \tilde{T}_L \,, \tag{3.12}$$

$$\tilde{T}_R \to c_R t_R - s_R \tilde{T}_R \,. \tag{3.13}$$

After the rotation, we explicitely write the first term in Eq. 3.2,from which we obtain the interaction vertex between the W boson and the bottom quark

$$g \bar{q}_L W_\mu^a \frac{\sigma^a}{2} q_L \,, \tag{3.14}$$

$$i g_{EW} \frac{\sqrt{2}}{2} \sin\theta_L \tilde{T}_L W^+ b_L + h.c. \,. \tag{3.15}$$

The coupling with the Z boson follows from the mixing of the W^3_μ and B_μ

$$\frac{2}{3}g'\bar{\tilde{T}}\not{B}\tilde{T} = \frac{2}{3}\frac{g}{c_w^2}\bar{\tilde{T}}\not{Z}\tilde{T} + \frac{2}{3}e\bar{\tilde{T}}\not{A}\tilde{T} \tag{3.16}$$

Since $\tilde{T}_R$ and t_R have the same quantum numbers, the Z vertex is not modified after the chiral rotation, and it is the Standard Model vertex, with no change. Then we will write explicitely the only rotation for the left-handed doublet.

Instead the Higgs coupling is given expliciting the term with the Goldstone Matrix

$$yf\left(\bar{Q}^5_L\right)U_{I5}\tilde{T}_R = \frac{yf}{\sqrt{2}}\sin\frac{h}{f}\bar{t}_L\tilde{T}_R \tag{3.17}$$

$$yfc_2\left(\bar{Q}^5_L\right)U_{I5}t_R = \frac{yc_2f}{\sqrt{2}}\sin\frac{h}{f}\bar{t}_Lt_R \tag{3.18}$$

3.2 Decay and production

From this terms we derive the Feynman rules, with which we can computing explicitely the decay widths we resum here

$$\Gamma_{Wb} = \frac{g^2_{EW}\sin^2\theta_L m^3_{\tilde{T}}}{64\pi m^2_W}f(x_W,x_b)g(x_b,x_W) \tag{3.19}$$

$$\Gamma_{Zt} = \frac{g^2_{EW}\sin^2\theta_L\cos^2\theta_L m^3_{\tilde{T}}}{128\pi m^2_W}f(x_Z,x_b)g(x_b,x_Z) \tag{3.20}$$

$$\Gamma_{Ht} = \frac{g^2_{EW}\sin^2\theta_L\cos^2\theta_L m^3_{\tilde{T}}(1-\xi)}{128\pi m^2_W}f(x_Z,x_b)[1+x_t^2+x_H^2)(1+x_t^2)+4x_t^2]\,, \tag{3.21}$$

where

$$f(x_i,x_j) = \sqrt{(1-(x_i+x_j)^2)(1-(x_i-x_j)^2)} \tag{3.22}$$

$$g(x_i,x_j) = 1-x_i^2+x_j^2(1+x_i^2)-2x_j^4\,. \tag{3.23}$$

where $x_i = m_i/M_{\tilde{T}}$. From these equations we can observe that in the limit $M_{\tilde{T}}\to\infty$ the functions $f\,,\,g\to 1$, then the Standard Model couplings are reproduced (i.e. the coupling that would have the top-partner if it has been a Standard Model field). We can give a brief estimation noting that in the limit $\sin\theta_L \ll 1 \Rightarrow \cos\theta_L \sim 1$, and knowing that $\xi \leq 0.2$ the Branching ratios divide in

- $\tilde{T}\to Wb$ with $Br(Wb)\sim 0.5$;
- $\tilde{T}\to tH$ with $Br(tH)\sim 0.25$;
- $\tilde{T}\to tZ$ with $Br(tZ)\sim 0.25$.

In this thesis we will consider the Wb decay channel, that has the largest decay width and an easier final state to detect. The Zt channel with subsequent decay to lepton is an interesting final state too, but it has a lower branching than that of the W boson, that is $Br(W\to l\nu)\sim 33\%$ (from [25]). The reconstruction of the Higgs event is more complex, since it has two bottom quarks, and however is not yet an analysis tool. To exclude the production of such particles at the Large Hadron Collider we have to determine the cross-sections. The single production of $\tilde{T}$ happens via electroweak process, instead, since the top-partners ared colore fermions, the pair production is

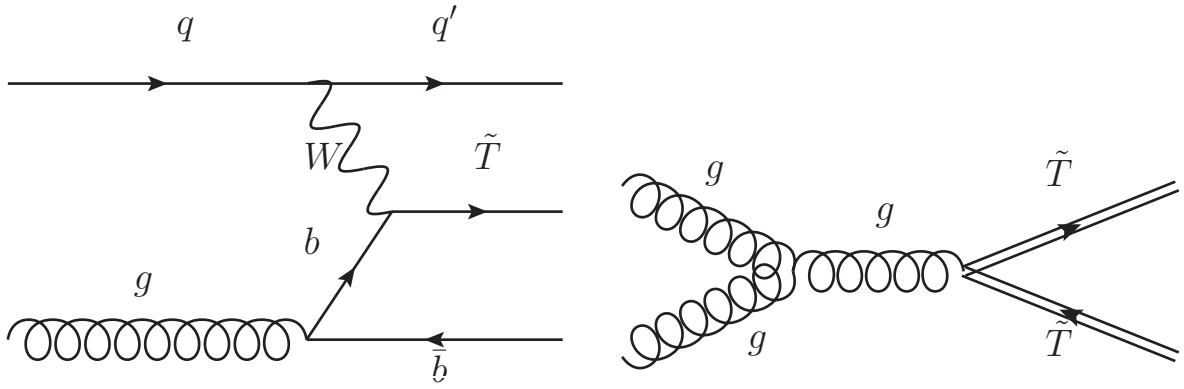

Figure 3.1: Single and pair production Feynman diagrams

through QCD interactions. Then the $\sigma_p air$ is parametrized in terms of the mass $m_{\tilde{T}}$, while we can write the cross section of the single production in terms of the interaction term

$$g_{Xt_R}\bar{X}_L \not{V} b_L \tag{3.24}$$

that leads to a parametrization

$$\sigma_{single}(\tilde{T}b) = (g_{\tilde{T}})^2 \sigma_{Vb}(m_{\tilde{T}})\,. \tag{3.25}$$

where σ_{Vb} resums the Electroweak interaction. In table 3.1 there are the values of the electroweak cross section and Fig. 3.1 shows the two different processes. This is an interesting simplification, from which we can start in defining our multi-dimensional parameter space of couplings. We can explicitly note that the coupling, and thus the cross section of the single production with subsequent decay to Wb, is completely controled by the chiral angle $\sin\theta_L(y, c_2, M_\psi)$. We recall that two of the free parameters are fixed to reproduce $M_{\tilde{T}}$ and m_t. Let's call hereafter $g_{\tilde{T}} = \frac{\sqrt{2}}{2} g_{EW} \sin\theta_L$. Accurate informations about the cross sections can be obtained by MonteCarlo simulation in association with tree-level diagrams computation. For the present work we have used MadGraph 5 [24], with model files implemented with FeynRules package (thanks to Matsedonski). MadGraph 5 is a matrix element generator, that allows to generate MonteCarlo events directly from the Lagrangian of a model. Some kinematic cuts are needed in the generation of the cross sections, then we set the transverse momentum of the parton jets to 5 GeV, in order to avoid infrared divergences. The maximum number of flavor considered as light jets is 4, and the Parton Distribution Function are the $CTEQ6L1$. The values of the Leading Order cross section both for singe and pair production at the Large Hadron Collider with $\sqrt{s} = 8\,TeV$ are reported in Table 3.2. Five mass points are considered, compatibly with what we have discussed in the previous section. The values of the coupling used in the model files are resummed in Table 3.3. From consideration of naturalness, $c_2 \sim y \sim 1$. In this scenario, we can see that the single production mode has a higher rate than the pair one. Then we will focus on this process, in particular, as we said before, on the Wb channel.

For what concerns the phenomenology of the decay, besides the $\tilde{T}$ production, we have a soft bottom-quark, that is useless for an analysis. The other important product of the Wb channel is the emission of a light forward jet, coming from the recoil of the top partner with initial parton states. This could be a variable that discriminates the signal from the backgrounds with high efficiency, provided the masses of the Standard Model particles produced are not so heavy as a top-partner, then the recoil of the forward jet is smaller, with values of the pseudo-rapidity more central. In Fig. 3.2 we can see the parton level distribution in the $\eta - p_T$ plan of this object. Then, besied the

$\tilde{T}$ mass (GeV)	$\sigma_{single}(Vb)(pb)$
600	$5.71 \pm 4 \times 10^{-4}$
700	$2.24 \pm 4 \times 10^{-4}$
800	$1.12 \pm 4 \times 10^{-4}$
900	$0.51 \pm 4 \times 10^{-4}$
1000	$0.40 \pm 4 \times 10^{-4}$

Table 3.1: Electroweak cross section at the Large Hadron Collider, $\sqrt{8}\,\text{TeV}$

$\tilde{T}$ mass (GeV)	$\sigma_{single}(Wb)(pb)$	$\sigma_{pair}(Wb)(pb)$
600	0.112	0.113
700	0.044	0.037
800	0.022	0.013
900	0.010	0.005
1000	0.008	0.002

Table 3.2: $\tilde{T}$ single and pair production at 8 TeV center of mass energy at LHC. The pair production information is taken from [23]

$\tilde{T}$ mass	y	c_2	$\sin\theta_L$
600	1	0.90	0.34
700	1	0.89	0.29
800	1	0.89	0.25
900	1	0.89	0.22
1000	1	0.89	0.20

Table 3.3: $\tilde{T}$ single production at 8 TeV center of mass energy at LHC. Decay channel Wb is considered, with subsequently leptonic decay of the W boson. Values of the couplings used for the generation in Madgraph. Everywhere the mass of the top quark is set to its PDG value $m_t \simeq 172.5\,\text{GeV}$

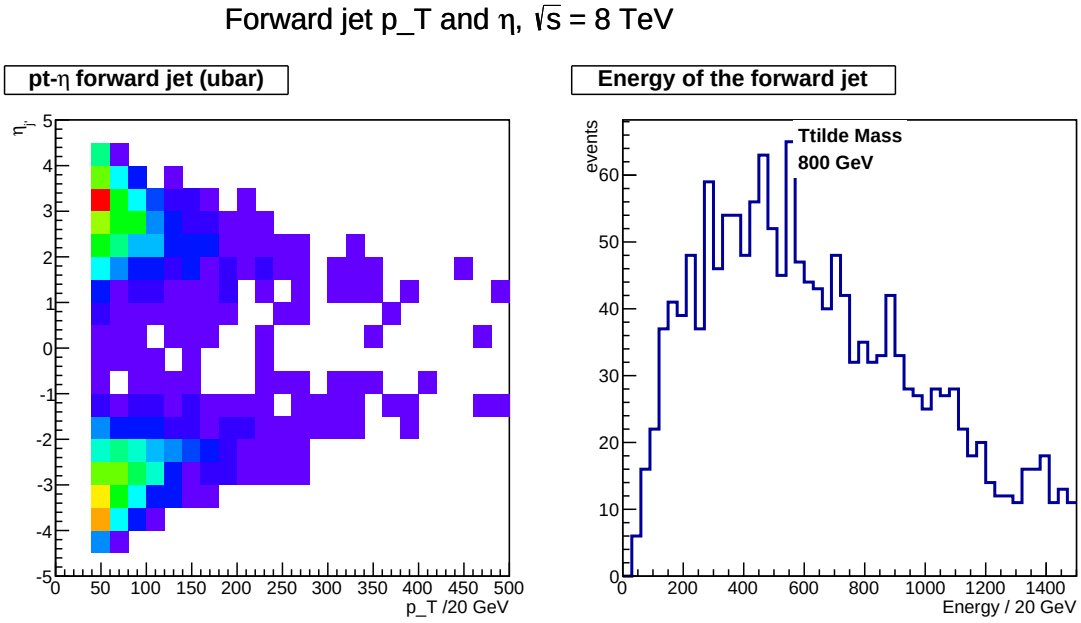

Figure 3.2: Pseudo-rapidity of the forwad jet $\eta_{j'}$, in the scenario with $m_{\tilde{T}} = 800\,\text{GeV}$.

forward jet there are the product of the $\tilde{T}$ decay, W and b, with the W that subsequently decays to leptons. This signature is very similar, except for the mass of the top-partner, to that of single top-quark production in the Standard Model. This is an important feature we will exploit in the subsequent analysis.

3.3 $\tilde{T}$ single production rate

We will now calculate explicitely the relation among the free parameters of the model, in order to get a suitable formula which allow us to better understand the sensitivity of the cross section in the parameters space of the model.

$$M = \begin{pmatrix} A & B \\ 0 & C \end{pmatrix} = -\begin{pmatrix} c_2 \frac{yf}{\sqrt{2}}\sqrt{\xi} & \frac{yf}{\sqrt{2}}\sqrt{\xi} \\ 0 & M_\psi \end{pmatrix} = L^\dagger \begin{pmatrix} m_t & 0 \\ 0 & M_{\tilde{T}} \end{pmatrix} R \tag{3.26}$$

when we chiral rotate the basis, we find

$$M = \begin{pmatrix} c_L & s_L \\ -s_L & c_L \end{pmatrix} \begin{pmatrix} m_t c_R & -m_t s_R \\ M_{\tilde{T}} s_R & m_t c_R \end{pmatrix} . \tag{3.27}$$

The $2-1$ entry has to vanish, then

$$0 = -m_t s_L c_R + M_{\tilde{T}} s_R c_L \tag{3.28}$$

and we obtain a relation between the two angles

$$\frac{\tan\theta_R}{\tan\theta_L} = \frac{m_t}{M_{\tilde{T}}} . \tag{3.29}$$

For the coupling of interest we will next consider only θ_L; let's write

$$M \cdot M^t = \begin{pmatrix} A^2 + B^2 & BC \\ BC & C^2 \end{pmatrix} = \begin{pmatrix} c_L & s_L \\ -s_L & c_L \end{pmatrix} \begin{pmatrix} m_t^2 c_L & -m_t^2 s_L \\ M_{\tilde{T}}^2 s_L & M_{\tilde{T}}^2 c_L \end{pmatrix} \tag{3.30}$$

the $1-2$ entry reads

$$BC = \frac{M_{\tilde{T}}^2 - m_t^2}{2} \sin(2\theta_L)\,. \tag{3.31}$$

Another constraint is given by the determinant equation

$$A \cdot C = m_t M_{\tilde{T}} \tag{3.32}$$

we can safely assume $A, B, C > 0$, since all the parameters of the Lagrangian can be made positive by a field redefinitions. The trace gives the following equation

$$m_t^2 + M_{\tilde{T}}^2 = A^2 + B^2 + C^2\,. \tag{3.33}$$

then combining the two equations, we obtain a suitable formula among the physical parameters and the angle

$$\frac{1}{c_2} = \frac{M_{\tilde{T}}^2 - m_t^2}{2 m_t M_{\tilde{T}}} \sin 2\theta_L\,. \tag{3.34}$$

With this formula we can easily variate the rate of production of $\tilde{T}$ using directly the couplings that enter in the Lagrangian of the model. From this constraint we have $0 \leq \sin 2\theta_L \leq 1$ and nothing else. This implies that we have a minimal value for c_2 (for which we have the maximal allowed coupling) that is

$$\frac{1}{c_{2,min}} = \frac{M_{\tilde{T}}^2 - m_t^2}{2 m_t M_{\tilde{T}}}\,. \tag{3.35}$$

This happens when $\sin(2\theta_L) = 1$ that is $\theta_L = \pi/4$. From this discussion we can thus note that the maximal coupling never reach the Standard Model value, since we have

$$\sin\theta_L^{max} = \frac{\sqrt{2}}{2} \Rightarrow g_{\tilde{T}} = \frac{\sqrt{2}}{2} g_{EW} \frac{\sqrt{2}}{2}\,. \tag{3.36}$$

$$\tag{3.37}$$

We note that the cross section is almost independent of ξ. In Fig. 3.3 we can see how the branching ratios change with the coupling c_2, then we can use directly the results given in Eq. 3.21 to compute the right cross section with subsequent decay of the top-partner to the Wb channel. Then, as we have just described, the cross section has a maximum at $c_{2,min}$ and a minimum with $c_2 \to \infty$, for which the cross section vanishes. Not considering such extreme scenario in the following analysis, we have drawn , in Fig. 3.4, a suitable variatons of the above cross sections, with $c_2 \in [c_{2,min}, 3]$.

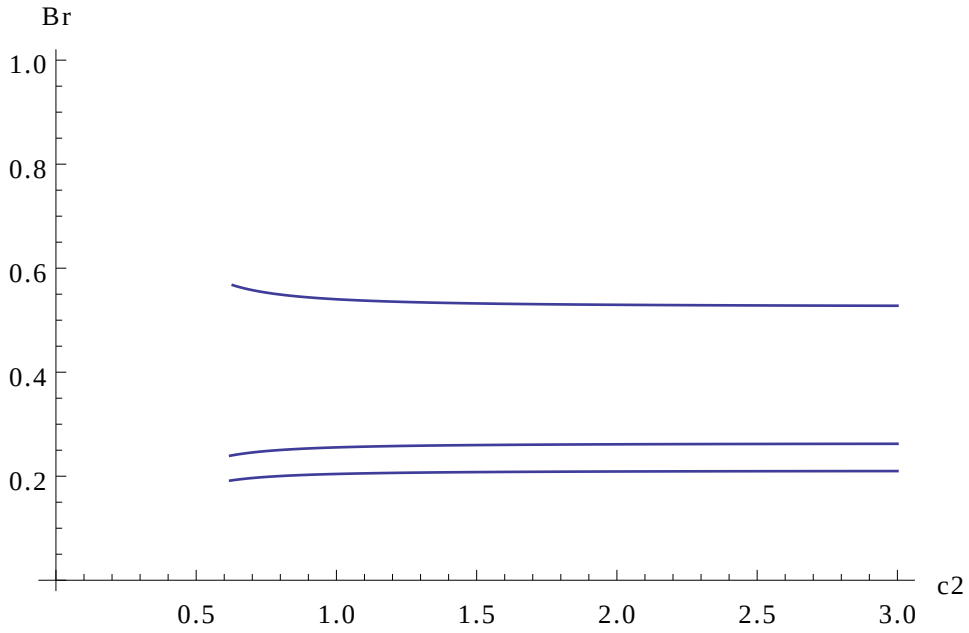

Figure 3.3: Branching ratios of the $\tilde{T}$ production with $M_{\tilde{T}} = 800\,\text{GeV}$ as a function of the coupling, with $c_2 \in [c_{2,min}, 3]$.

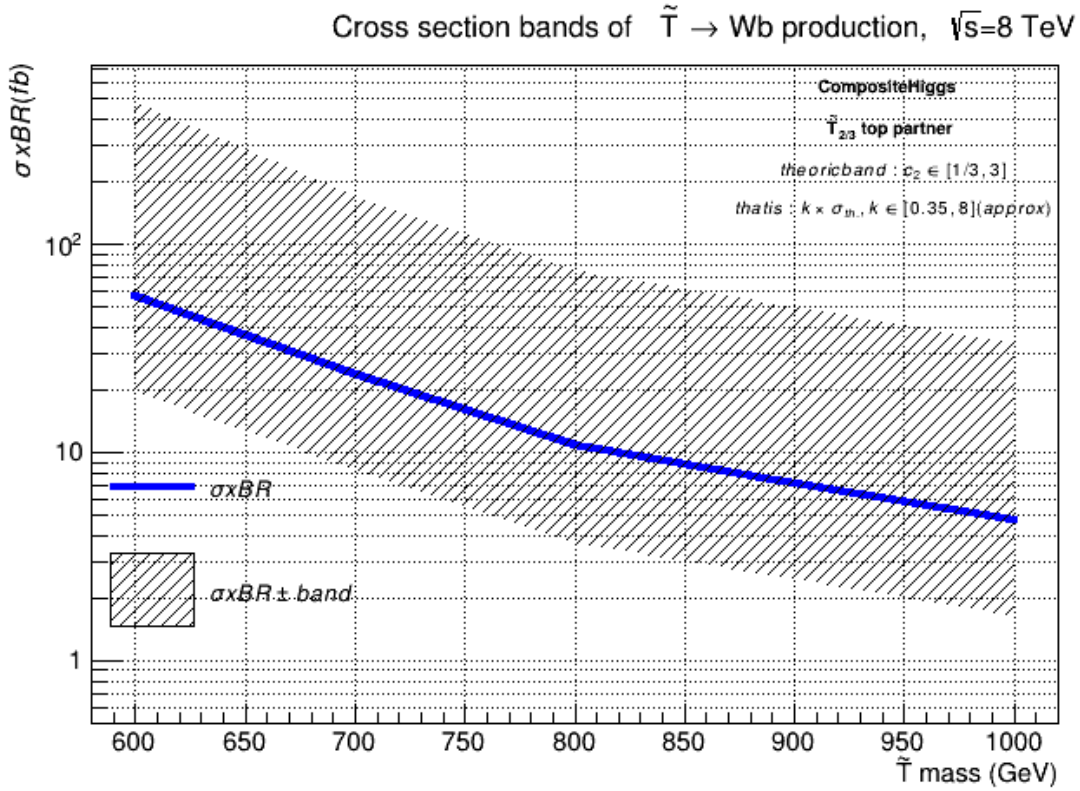

Figure 3.4: Cross section with theoric band for the top partner in the singlet at the Large Hadron Collider $\sqrt{s} = 8\,\text{TeV}$

Chapter 4

Experimental environment

4.1 The Large Hadron Collider

The Large Hadron Collider (LHC) [26] is a proton-proton and heavy ion accelerator installed at CERN, in a tunnel about 100 m underground in Geneva, Switzerland. The choice of a non-elementary particle as the proton for the beams instead of electrons-positrons was mandatory due to the energy loss by synchrotron radiation, which was the ultimate limitation for the LEP beam energy. Being proportional to γ^4 the synchrotron radiation for protons is $(m_p/m_e)^4 \sim 10^{13}$ smaller than for electrons.

The LHC ring is composed by two parallel adjacent beam pipes at the radial distance of 2.8 cm from proton beams, one for each pipe (Fig. 4.1b). Along the LHC there are only four interaction points in correspondence to the four diametrical opposite experiments installed on the ring. The *Compact Muon Solenoid* (CMS) and the *A Toroidal LHC Apparatus* (ATLAS) are multipurpose detectors, while the *LHC bottom Experiment* (LHCb) and *A Large Ion Collider Experiment* (Alice) are more focused on specific physics studies. In particular LHCb has been designed to study the CP symmetry violation in b physics, while Alice to analyze the quark-gluon plasma produced mainly in heavy ion runs.

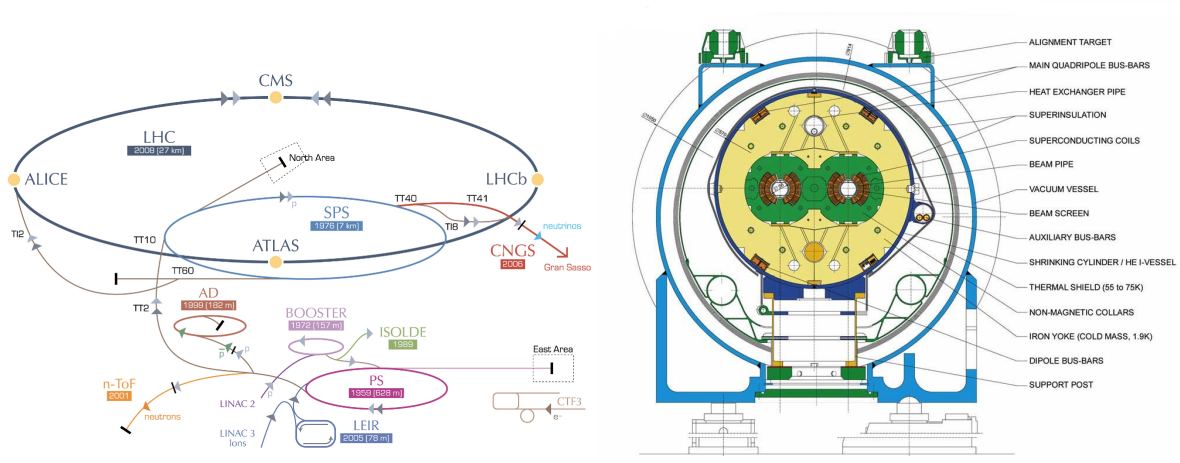

(a) The LHC accelerator complex

(b) Section of a LHC magnet

Figure 4.1: The Large Hadron Collider

The commissioning for the LHC started on December 5^{th} 2009 with a first pilot physical Run at 900 GeV and $2 \cdot 10^{10}$ proton/bunch with 16×16 bunches circulating inside LHC. At the end

Energy per nucleon	E	7 TeV
Dipole field at 7 TeV	B	8.33 T
Design luminosity	$\mathcal{L}$	$10^{34} cm^{-2} s^{-1}$
Bunch separation		25 ns
Number of bunches	k_B	2808
Number of particles per bunch	N_p	$1.15 \cdot 10^{11}$
β value IP	β^*	0.55 m
RMS beam radius at IP	σ^*	16.7 μm
Luminosity lifetime	τ_L	15 $hours$
Number of collision/crossing	n_c	≈ 20

Table 4.1: The Large Hadron Collider main features

of December also some 2.36 TeV collisions were done, already making the LHC the most powerful proton accelerator machine in the world. Consecutively the first real physical Run started on March 30^{th} 2010 with a nominal beam energy of 3.5 TeV and a luminosity goal of at least 1 fb^{-1} already achieved in the first months of 2011.

The usage of two proton beams instead of having one composed by anti-protons (like at the Tevatron or at the $Sp\bar{p}S$) is not a disadvantage from the physics point of view, given the higher center of mass energy; on the contrary, it allows an easy and fast population of both beams with a high number of particles. The fact that the two partons involved in the interaction have unknown momentum has two fundamental consequences. First of all the total effective energy of an event is unknown, because the proton remnants, that carry a sizable fraction of the proton energy, are scattered at small angles and are predominantly lost in the beam pipe, escaping undetected. Experimentally, it is therefore not possible to define the total and missing energy of the event, but only the total and missing transverse energies (i.e. in the plane transverse to the beams). Moreover, the center of mass may be boosted along the beam direction; it is therefore very useful to use experimental quantities that are invariant under such boosts, such as pseudorapidity (see Section 4.2.1).

The collisions are between two counter-rotating proton beams, each with an energy of 4.0 TeV (in 2012) giving a total collision energy of 8 TeV. The machine is composed by 1232 magnet dipoles, which can yield a magnetic field up to 8.3 T, and by 392 quadrupoles for the focalisation of the beam. In order to reach this very high value of magnetic field the magnets are brought at the temperature of 2.3 K with a cryogenic system based on liquid helium. Radio frequency cavities installed between one dipole and the following provide to generate an opportune electric field to increase the proton energy of 0.5 MeV per turn. The luminosity is

$$\mathcal{L} = \frac{\gamma f k_B N_p^2}{4\pi \epsilon_n \beta^*} F$$

where γ is the boost Lorentz factor, f is the revolution frequency, k_B and N_p refer respectively to the number of the bunches and to the number of protons per bunch. ϵ_n is the normalised transverse emittance while β^* is the betatron function at the interaction point. Finally F is the reduction factor due to the crossing angle of the bunches. For LHC the design value for the luminosity is $\mathcal{L} = 10^{34} cm^{-2} s^{-1}$ [27] for collision energy of 14 TeV, which corresponds to one billion pp collisions per second. The maximum number of bunches that can circulate in the machine is 2808 with a

25 ns time span between each other. The gaps of the beam are used to synchronise the beam, acquiring calibration data and providing resets to front-end electronics.

4.2 The Compact Muon Solenoid

The Compact Muon Solenoid (CMS) [28], shown in Fig. 4.2, is a cylindrical barrel 21.6 m long, with a diameter of 15 m. It is one of two general purpose particle physics detectors built at LHC. The detector has been designed to study various aspects of pp collisions at $\sqrt{s} = 14\ TeV$ and heavy-ion (Pb-Pb) collisions at $\sqrt{s} = 5.5\ TeV$, that will be provided by the LHC at a design luminosity of $10^{34} cm^{-2} s^{-1}$ and of $10^{27} cm^{-2} s^{-1}$, respectively.

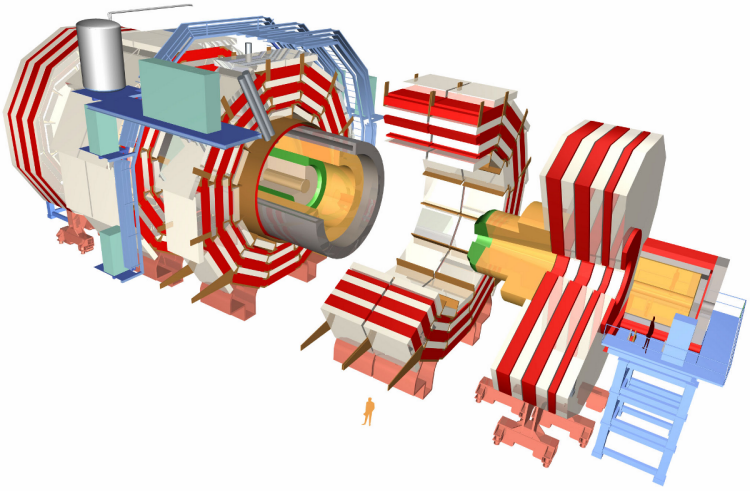

Figure 4.2: The Compact Muon Solenoid [1]

To enhance the physics reach of the experiment the CMS subcomponents must provide:

- a high performance system to detect and measure muons
- a high resolution method to detect and measure electrons and photons
- a high quality central tracking system to give good reconstruction of charged particle tracks and accurate momentum measurements
- a "hermetic" calorimeter, designed to entirely surround the collision and prevent particles from escaping

With these priorities in mind, the first essential item was a very strong magnet. The higher a charged particle's momentum, the less its path is curved in the magnetic field, so when knowing its path its momentum can be measured. A strong magnet was therefore needed to allow us to accurately measure even the very high momentum particles, which can provide a discovery of new physic at high energy, such as energetic muons. A large magnet also allowed for a number of layers of muon detectors within the magnetic field, so momentum could be measured both inside the coil (by the tracking devices) and outside of the coil (by the muon chambers).

The magnet is the Solenoid in Compact Muon Solenoid; it is a coil of superconducting wire that creates a magnetic field when electricity flows through it; the CMS solenoid has an overall length of 13 m and a diameter of 7 m, and generates a homogeneous magnetic field of the strength of 3.8 T [**?**] ($\sim 100,000$ times stronger than that of the Earth). To reach the necessary current of 41.7 $MA/turn$, the 220 t solenoid cold mass is composed of a 4-layer of NbTi wires co-extruded

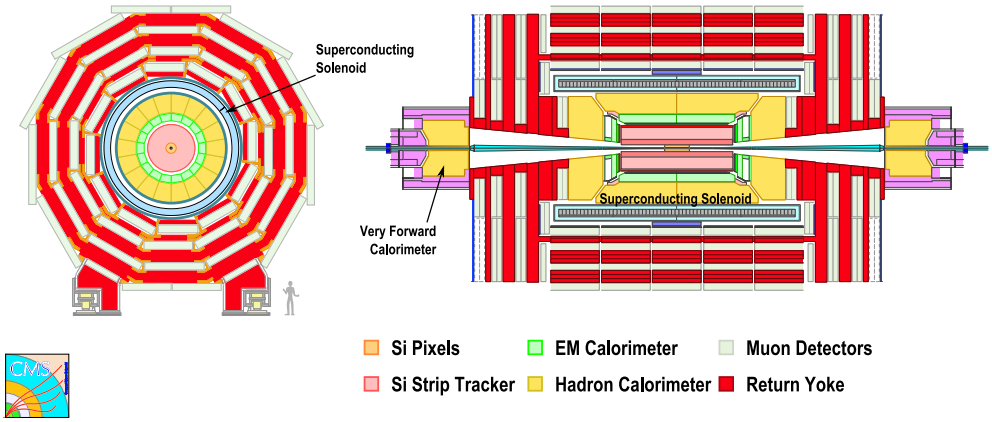

Figure 4.3: CMS front and side views, with its main apparatus highlighted [**?**]

and mechanically reinforced with Al. The solenoid thickness is 3.9 radiation lengths and it can store up to 2.6 GJ of energy. The field is closed by a 12,000-tonne yoke made of five three-layered dodecagonal barrel wheels and three end-cap disks at each end of common structural steel. The coil is cooled down to 4.8 K by a helium refrigeration plant, while insulation is given by two pumping stations providing vacuum on the 40 m^3 of the cryostat volume. Its main role is to increase the field homogeneity in the tracker volume and to reduce the stray field by returning the magnetic flux of the solenoid. In addition, the yoke is instrumented with four layers of muon stations and the steel plates play the role of absorber for these four interleaved layers ("stations") of muon chambers, which provide for a measurement of the muon momentum independent of the inner tracking system.

The CMS magnet is the largest magnet of its type ever constructed and allows the tracker and calorimeter detectors to be placed inside the coil. ATLAS in contrast has chosen the so-called *small coil* solution, where only the tracker is inside the solenoid coil (with a field strength of 2 T). Their calorimeters and the muon system are located outside the solenoid coil and are in an extra toroidal magnetic field. CMS is a little smaller compared to ATLAS, but with a weight of 14,000 tonnes CMS is much heavier and weighs twice as much as ATLAS.

4.2.1 CMS coordinate system

The interaction point is chosen as the center of the coordinate system, the z-axis points along the beam pipe towards the Jura mountains from LHC Point 5, the y-axis points vertically upward and the x-axis points to the center of the LHC. Since the detector has a cylindrical shape the cylindrical coordinate system is used. It is described by the radial distance to the beamline r, the polar angle θ and the azimuthal angle φ. The polar angle is measured with respect to the z-axis: $\theta = 0$ corresponds to the positive z-direction and $\theta = \pi$ to the negative z-direction. The azimuthal angle is measured from the x-axis in the xy-plane: $\varphi = 0$ points to the positive x-direction and $\varphi = \pi/2$ to the positive y-direction. The pseudo-rapidity η is defined as:

$$\eta = -\log \tan\left(\frac{\theta}{2}\right)$$

This leads to an η of 0 for particles moving perpendicular to the beam direction and the beam direction itself has a pseudo-rapidity of $+\infty$ in $+z$ and $-\infty$ in $-z$ direction. The region of $|\eta| < 1.4$ will be referred to as the central region in the following. Both $\Delta\eta$ and $\Delta\varphi$ of two particles are independent of Lorentz boosts, therefore the distance between two particle can be measured in a

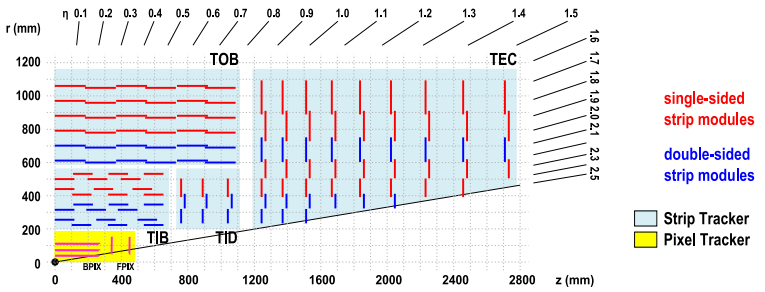

(a) Scheme of the silicon strip detectors and their angular $|\eta|$ coverage

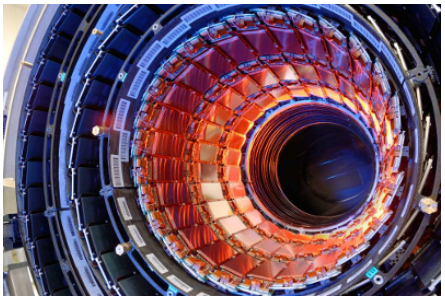

(b) The barrel region of the silicon strip detector. Some of the modules can be seen without the pixel detector installed

Figure 4.4: The CMS tracker systerm

third Lorentz invariant variable:

$$\Delta R = \sqrt{\Delta\eta^2 + \Delta\varphi^2}$$

4.2.2 Tracker

The CMS tracker [29] [30] is a cylindrical detector of 5.8 m in length and 1.2 m in radius and measures charged particles within the $|\eta| < 2.5$ pseudo-rapidity range and is fully immersed in the 3.8 T magnetic field produced by the CMS superconducting solenoid. Its purpose is to provide high resolution track hits as close as possible to the interaction point. The large charged track density close to the beam requires the usage of a pixel system (Section 4.2.2), which can provide three dimensional hit information while keeping the pixel occupancy low. The precise and efficient measurement of the tracks close to the interaction region is essential to determine their impact parameters with respect to the collision point and moreover to provide a precise reconstruction of secondary vertices. These quantities are the basis for the tagging of b-jets.

The typical momentum resolution achieved by the inner tracking system is $\Delta p_T/p_T = 0.7\%$ at 1 GeV, 5% at 1 TeV [31].

Pixel detector

The pixel detector is the closest one to the beam pipe, therefore it is exposed to very high levels of radiation coming from the collisions. The radiation at a distance of 8 cm from the beam pipe will be of about 10 million particles per cm^2 per second. This number is very high and demanded a careful design for this system. The radiation hardness achieved in the pixel detector system will allow it to operate for about 10 years. When a charged particle passes through any of those sensors, the electrons in the silicon get enough energy to create electron-hole pairs and therefore a small electrical current, this current is read out by the electronics attached to each tile. The pixel readout allows the experimentalist to know a charged particle trajectory with a space resolution of one tile (100 μm by 150 μm).

Silicon strip detectors

Once the particles leave the pixel detector [32], they pass through ten layers of Silicon Strip Detectors (SSD) (Fig. 4.4). These detectors surround the pixel system and they go out until a radius of 130 cm completing the central part of the CMS tracker (Fig. 4.4a). The SSD contains 15,148 sensitive modules with a total of 9.3 million strips. All the information produced is read by 80,000 microelectronic chips. Each one of these modules is made out of a set of sensors, a mechanical

support structure, and the electronics for the readout. The SSD has an active area of $200m^2$ and consist of four inner barrel layers assembled in shells (TIB); two inner end-caps, each one composed of three small discs (TID); an outer barrel formed by six layers of detectors (TOB); and two outer end-caps that close the tracker (TEC) [33].

4.2.3 Electromagnetic calorimeter

The electromagnetic calorimeter (ECAL) [34] of the CMS detector is a homogeneous crystal calorimeter. The CMS ECAL is build out of lead tungstate ($PbWO_4$) crystals, a transparent material denser (8.3 g/cm^3) than iron, with a radiation length X_0 of 0.89 cm, a Molière radius R_M of 2.19 cm and with fast response (80% of light emitted within 25 ns, corresponding with the designed bunch crossing rate of the LHC). ECAL is composed of a barrel covering $|\eta| \sim 1.48$ and two endcaps covering $1.48 < |\eta| < 3.0$. The barrel is made of 61200 trapezoidal and quasi-projective crystals of approximately $1 \times R_M$ in lateral size and about $25.8X_0$ in depth. The barrel inner radius is 124 cm. Viewed from the nominal interaction vertex, the individual crystals appear tilted (off-pointing) by about 3° both in polar and azimuthal angles and the granularity is about $\Delta\eta \times \Delta\varphi = 0.0175 \times 0.0175$ rad. The barrel is divided into two halves, each made of 18 super-modules containing 1700 crystals. Each super-module is composed of four modules. The end-caps consist of two detectors, a pre-shower device followed by $PbWO_4$ calorimetry. The pre-shower is made of silicon strips placed in a 19 cm sandwich of materials including about 2.3 X_0 of Pb absorber. It covers inner radii from 45 cm to 123 cm, corresponding to the range $1.6 < |\eta| < 2.6$. Each end-cap calorimeters are located at a distance of 314 cm from the nominal vertex and cover $1.479 < |\eta| < 3.0$. They are made of 7324 rectangular and quasi- projective crystals of approximately $1.3 \times R_M$ in lateral size and about 24.7 X_0 in depth.

The ECAL has an energy resolution of better than 0.5% above 100 GeV. The HCAL (see Fig. 4.5), when combined with the ECAL, measures jets with a resolution $\Delta E/E \approx 100\%/E \oplus 5\%$.

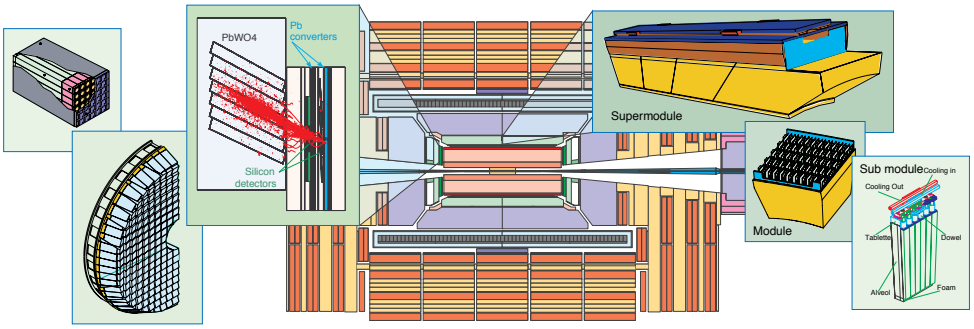

Figure 4.5: The CMS Electromagnetic Calorimeter (ECAL)

4.2.4 Hadronic calorimeter

The magnet system directly following the hadronic calorimeter (HCAL) [35] has a large impact on its design since most of the hadronic calorimeter is located inside the magnet coil which can not be enlarged arbitrarily. The most important requirements to be fulfilled by the hadronic calorimeter are those of maximizing the number of hadronic interaction lengths inside the magnet coil to minimize the non-Gaussian tails in containment and guaranteeing the hermeticity for the measurement of jets and of the transverse energy. This is achieved by using brass as absorber material with layers of active, scintillating material in between. The scintillating material is chosen to be a plastic scintillator connected with wavelength- shifting fibers to the multi-channel hybrid photodiodes which read out the signal.

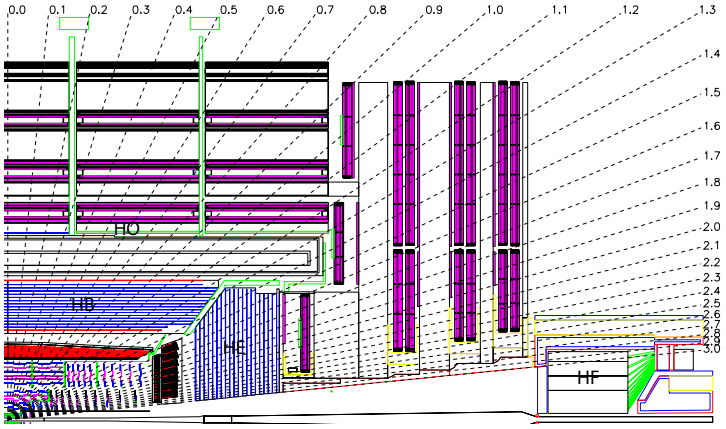

Figure 4.6: The CMS Hadronic Calorimeter (HCAL)

The barrel part of the hadronic calorimeter covering $0 < |\eta| < 1.4$ consists of 15 layers of absorber of 5 cm combined with scintillators as thin as 3.7 mm accompanied by two external layers of stainless steel for mechanical strength. In front of the first layer of absorber a 9 mm scintillator is located and it is optimized to collect 1.5 times more light then the other scintillators. The end-caps of the hadronic calorimeter cover $1.3 < |\eta| < 3.0$ with a granularity of $\Delta\eta \times \Delta\varphi = 0.175 \times 0.175$. Each end-cap consists of 1152 towers.

The last part of the hadronic calorimeter is the hadronic forward calorimeter (HF) which increases the containment and hermeticity of the system. It is located 11.2 m from the nominal interaction vertex and has a depth of the absorber of 1.65 m. It covers $3.0 < |\eta| < 5.0$ and is made of steel as absorber and quartz fiber. The signal is produced by light emitted due to the Cerenkov effect in the quark fibers and is channeled by them to photomultipliers detecting the light, which enables the hadronic forward calorimeter to derive an effective electromagnetic fraction of energy corresponding to the first centimeters of the absorber as in this region of $|\eta|$ where no electromagnetic calorimeter is available.

4.2.5 Muon system

While electromagnetic and hadronic particles are mainly contained inside the calorimeters, muons are able to travel through the solenoid with minimal energy loss inside the detector. Muons can provide strong indication of interesting events at hadron collider and are natural candidates for triggering purposes. The CMS muon system [36] was designed to cope with three major functions: robust and fast identification of muons, good resolution of momentum measurement and triggering. The muons are measured in the pseudo-rapidity window $|\eta| < 2.4$, with detection planes made of three technologies: Drift Tubes, Cathode Strip Chambers, and Resistive Plate Chambers. Matching the muons to the tracks measured in the silicon tracker results in a transverse momentum resolution between 1 and 5%, for p_T values up to 1 TeV/c.

The muon spectrometer [36] consists of three different kinds of detectors: 250 drift tubes chambers (DTs) in the barrel region of $|\eta| < 1.2$, 540 cathode strip chambers (CSCs) covering the end-cap region up to $|\eta| < 2.4$, and 912 resistive plate chambers (RPCs) in the range of $|\eta| < 1.6$ covering the whole barrel and parts of the end-caps. The iron magnet return yoke hosts the muon detector stations. The barrel region ($|\eta| < 1.2$) is composed by 5 wheels, each divided in 12 sectors which cover each a 30° azimuthal angle. Four iron gaps within each sector are equipped with detector stations. The barrel muon station consists of one DT and two RPCs joint together. The two end-caps are made of three iron disks and four layers divided into two or three stations of CSCs

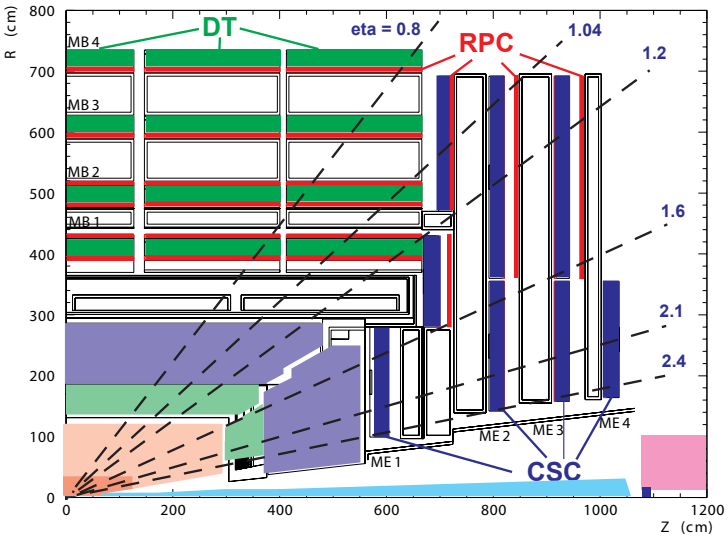

Figure 4.7: Section view of the CMS muon chambers and their coverage as a function of η [**?**]

and RPCs.

Chapter 5

Simulation, reconstruction and Datasets

5.1 The Compact Muons Solenoid *FastSimulation*

The events generated by the MonteCarlo generator contain only a list of finale states particles with their energies and momenta as coming out of the hard interaction process; they need to undergo the simulation of the detector response to be compared with the real data. The CMS collaboration has developed two different types of MonteCarlo simulation: a detailed *GEANT4*-based [37] simulation, and a simpler but faster implementation of particle propagation and interaction (called Fast Simulation [38]). The FastSimulation is based on a detector model with simplified geometry, response evaluation and pattern recognition, to decrease the processing time per event. The particles produced by event generators, used as inputs to the simulation, are propagated through the detector undergoing all the physically relevant material effects and interactions. With complex events taking minutes to simulate using Geant4, the FullSimulation cannot keep up with the constraints imposed by time, computing power and needed statistics. At 100-1000 times faster per event, the FastSimulation is the only way to produce large statistic data sets necessary especially for beyon the standard model analyses that require to cover a large phase space of parameter points. Let's look in more details at the Fast Simulation approach:

- GEOMETRY: the FastSimulation uses a simplified version of the CMS geometry, using nested cilindrical layer. Particles are propagated from one layer to the next;
- MATERIAL EFFECTS: bremsstralhung, photon conversion, multiple Coulomb scattering, energy loss through ionization and nuclear interactions are computed analytically . Cross sections are taken from Particle Data Group (or Data Libraries) and the kinematics are derived from single particle collisions saved beforehand.
- TRACK RECONSTRUCTION: since the pattern recognition phase of track reconstruction is very time consuming, the Fast Simulation implements instead an emulation of the pattern recognition. The hits of the "true" MonteCarlo particle are used to build and fit the track, for this reason no fake tracks are possible. This is reasonable in the configuration of tracking of 2011 and 2012 where the fake rate is very small.
- MUON: muons are propagated in the magnetic field through the tracker and calorimeters with average energy loss, then dE/dX and multiple scattering in the iron yokes of the muon chambers are computed. Muon simulated hits are produced in all sections of the muon revelation system.

- CALORIMETRY: the Grindhammer [39] parametrization is used to simulate electron showers in the Electromagnetic Calorimeter (ECAL). Photons undergo pair conversions based on the number of radiation lenghts they have traversed. Energy leakage into the crystal gaps and into the Hadron Calorimeter (HCAL) are included, as well the electronic noise. Shower simulation in the HCAL is similar, with different types of particles parametrized from GEANT-based simulation results.

In chapter 3 we studied the generation of the signal process. In order to be able to compare the MonteCarlo events with the data, the next step is to run the FastSimulation on the Les Houches Event files. The explicit command we set was:

```
cmsDriver.py Hadronizer_TuneZ2star_8TeV_generic_LHE_pythia_tauola_cff.py
 --filein=file:process.lhe --step GEN,FASTSIM,HLT:7E33v2
 --beamspot Realistic8TeVCollision --conditions START53_V7C::All
  --pileup 2012_Summer_inTimeOnly --datamix NODATAMIXER
 --eventcontent AODSIM  --datatier AODSIM --fileout=file: process.root
```

- *Hadronizer_TuneZ2star_8TeV_generic_LHE_pythia_tauola_cff.py* is the fragment which contains the information about the hadronization of the signal, implemented by PYTHIA 6.4 [40]. Tauola performs the polarization of the fermion particles.
- the input file is the Les Houches Events generated in 3;
- Generation, FastSimulation, HighLevelTrigger with 6×10^{33} instant luminosity are used;
- $\sqrt{s} = 8\,\text{TeV}$;
- START53_V7C::All, Global Tag;
- Pileup "2012_Summer_inTimeonly": represents the distribution used to simulate the effects of the multiple interactions based on the pattern of the pile-up distribution measured in data, during the second half of 2012 data taking, shown in Fig. 5.1 ;
- *eventcontent* and *datatier* set the type of object in output of the FastSimulation: AOD, that is Anaysis Object Data. AOD is the compact analysis format, designed to allow a wide range of physics analyses whilst occupying sufficiently small storage so that very large event samples may be held at many centres. AOD events contain the parameters of high-level physics objects, plus sufficient additional information to allow kinematic refitting.

5.2 Event reconstruction in CMS

The event reconstruction is the operation of constructing physics quantities from the raw data collected by the experiment. The reconstruction process is seen as a collection of independent units, each one providing a set of corresponding reconstructed objects as an output. Each reconstruction unit retrieves information from the input event, and produces and adds to the event new products. It is performed as a "Framework application", in which all steps are explicitly scheduled in advance, and care is taken to ensure that any information required by a given reconstruction unit will have already been prepared by a prior unit. The output of the Data Acquisition (DAQ) system consists of signal pulse heights, the time when the signal occurred, and the address of the detector element where it occurred. The Particle Flow algorithm, [41], is an event recostruction method based on the optimal combination of informations among all the available subdetectors of the Compact Muon

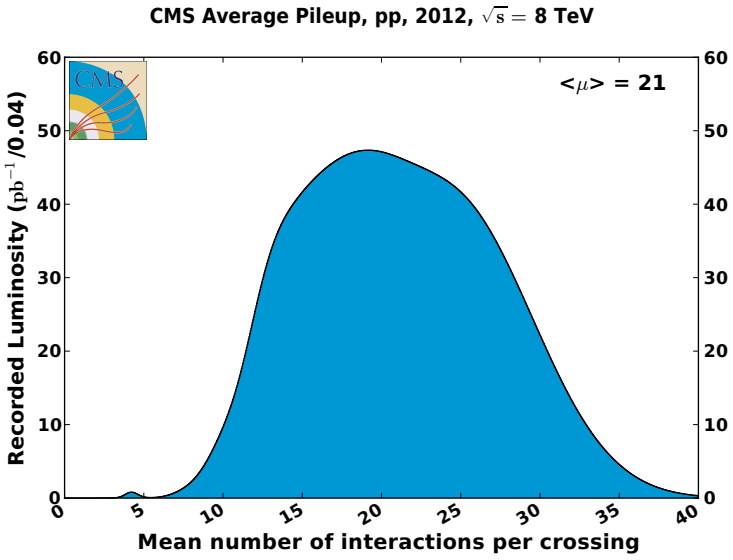

Figure 5.1: Pile-Up distribution

Solenoid. This approach has its reason in the intrinsic structure of the detector; charged particle tracks, ECAL and HCAL clusters and muon tracks are the fundamental building bricks of this algorithm. These must be delivered with high efficiency and low fake rate event in high-density environments like jets hadronization. The Particle Flow method is an off-line way to determine momenta, energy, directions and positions of the individual physical objects. Looking at Fig. 5.2, we can better understand how the Particle Flow algorithm works: an ECAL cluster not linked to any track is a photon, an ECAL and HCAL cluster matched to a track is a charged hadron, an HCAL cluster without a track gives a neutral hadron. Electrons are only ECAL cluster linked to a track; a muon releases hits in the muon chambers. These are the basic elements, from which we can reconstruct other composite physical objects, as τ leptons, from their decay products, jets from hadronization and missing transverse energy. Since thousands of particles are generated in each event, some quality requirements are needed. The CMS collaboration study the best compromise between purity and efficiency to give the most realistic reconstruction of physical objects.

5.2.1 Track reconstruction

The high resolution of the tracker and the large magnetic field allow an extremely accurate measurement of the momentum of the charged particles. The proton-proton interaction region, known as the beamspot, is used as a first estimate of the hard interaction point. Tracks are seeded from either triplets of hits or pairs of hits with an additional constraint from the beamspot or a pixel vertex. This first estimate of the trajectory is then propagated outwards in a search for compatible hits with the combinatorial track finder (CTF). An additional search for hits is performed from the outer boundaries of the detector and propagating inwards. Finally, the tracks are fitted and filtered to remove those that are likely fakes. Before starting the next iteration of the algorithm, hits that were unambiguously assigned to a track are removed from the collection to create a smaller, cleaner collection. The first iterations usually pick up prompt tracks, with high quality and higher p_T, while the the following iterations find displaced tracks or tracks with missing hits in the pixel detector, allowing the reconstruction of conversions or nuclear interactions, down to very low p_T.

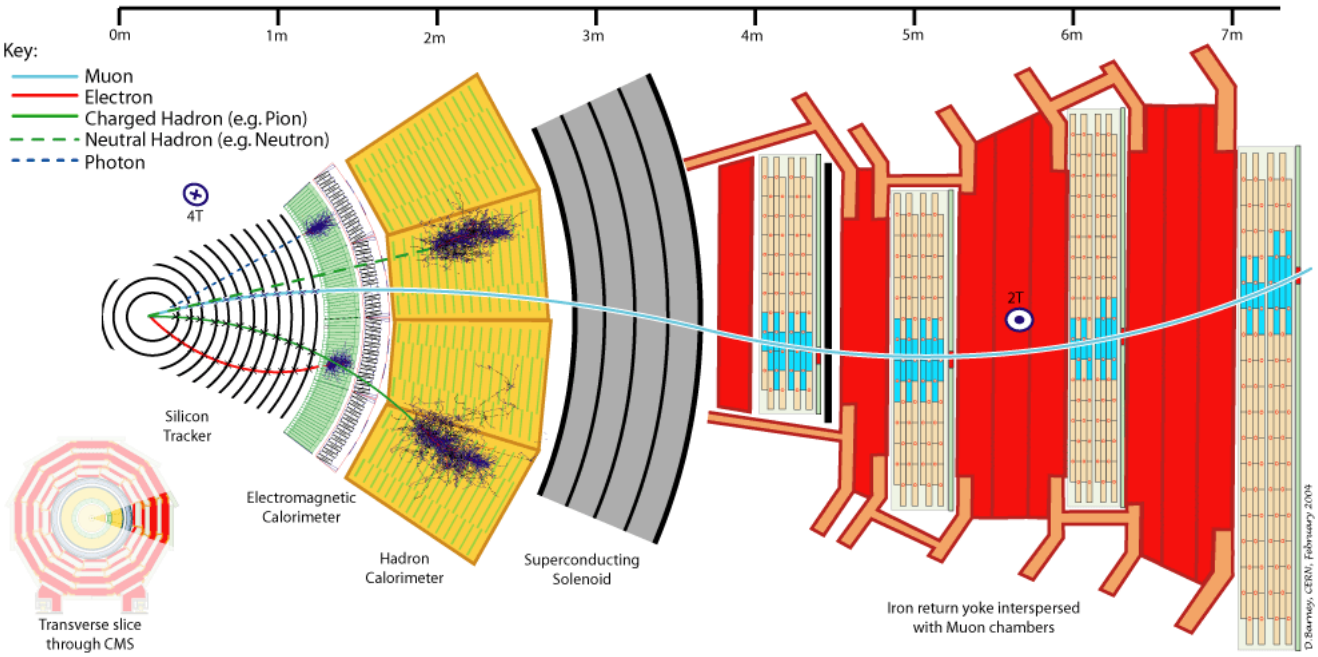

Figure 5.2: Transverse view of CMS detector with some examples of tracks

5.2.2 Vertex reconstruction

The primary interaction vertex is reconstruced combining collections of tracks. These candidate tracks are clustered along the $z-axis$, then a fit algorithm is performed to find the most compatible vertex with the selected tracks. The reconstruction of the vertex is then used to better estimate track momenta and parameters. In this analysis, at least one primary vertex is required to be reconstructed from at least four tracks, requiring the track fit to have $n_{dof} \geq 5$, with $z_{PV} < 24\,\text{cm}$ and $\rho_{PV} < 2\,\text{cm}$, where $|z_{PV}|$ and ρ_{PV} are the vertex distance with respect to the nominal interaction point along the $z - axis$, and to the transverse plane. Prompt tracks are defined by some variables, the transverse impact momentum d_0, the number of hits and the normalized χ^2.

5.2.3 Muon Reconstruction

The muon offline reconstruction starts with the reconstruction of hit positions in the DT, CSC and RPC sub-systems. The hits within each DT and CSC are matched. In the offline reconstruction, the latter are collected and matched among each other in order to generate seeds, which give the position, direction and a first p_T estimate of the muon candidate. The segments and hits from all three muon sub-systems are used in a muon track fit, which is based on the Kalman filter technique [42]. The result is a collection of objects reconstructed in the muon spectrometer, which are referred to as standalone muons. To improve the momentum resolution, a beam-spot constraint can be applied in the fit. To benefit from the full CMS resolution, the standalone muon tracks are then matched with the tracks reconstructed in the central silicon tracker and combined to form global muon tracks. For each standalone muon track, a search for tracks matching it among those reconstructed in the inner tracking system (referred to as "tracker tracks", "inner tracks" or "silicon tracks") is performed, and the best matching tracker track is selected. For each "tracker track" - "standalone muon" pair, the track fit using all hits in both tracks is performed, again based on the Kalman filter technique. The result is a collection of objects referred to as "global muons". The efficiency to reconstruct a global muon candidate with $p_T > 7\ GeV$ and $|\eta| < 2.4$ is 99% for events

accepted by the HLT. Quality criteria impose the agreement of the two approach, leading to a high efficiency in recostructing high energy leptons.

For each muon candidate, a number of quantities is computed that can help to distinguish isolated muons from the muons embedded in jets. Tracker- and calorimeter- based isolation requirements are imposed to reduce the contamination from the W +jets and tt backgrounds with secondary muons from b-quark jets. First, the sum of the p_T of the tracks, within a $\Delta R = 0.3$ cone around the global muon candidate, must be lower than 10 GeV for the muon to pass the loose tracker isolation and 2 GeV for the tight tracker isolation. The tracks contributing to the sum need to pass the transverse momentum threshold of 0.9 GeV and come from the event vertex ($|z_{track} - z_\mu| < 0.2\,\text{cm}$). Second, the energy in the electromagnetic and hadronic calorimeters, within a $\Delta R = 0.3$ cone around the global muon candidate, must be lower than 10 GeV for the muon to pass the loose calorimeter isolation and 5 GeV for the tight calorimeter isolation. In both cases, a veto cone of $\Delta R = 0.01$ around the global muon candidate is taken into account. Together with these muon isolation criteria, the muon selection has an efficiency of 92% for muons passing the HLT requirements.

5.2.4 Electron Reconstruction

Electrons energies are measured in the CMS Hadron Calorimeter. To collect the photons and electrons energy in the Electromagnetic Calorimeter, local deposits ("basic clusters) are summed into superclusters (SCs) which are extended in ϕ . After applying small energy corrections the superclusters are used to reconstruct photons and electrons, and to seed electron track reconstruction. Electron reconstruction uses two complementary algorithms at the track seeding stage: "tracker driven" seeding, more suitable for low p_T electrons as well as performing better for electrons inside jets and "ECAL driven" seeding. The "ECAL driven" algorithm starts by the reconstruction of ECAL "superclusters" of transverse energy $E_T > 4\,\text{GeV}$ and is optimized for isolated electrons in the p_T range relevant for Z or W decays and down to $p_T 5GeV$. A "supercluster" is a group of one or more associated clusters of energy deposits in the ECAL constructed using an algorithm which takes account their characteristic narrow width in the η coordinate and their characteristic spread in ϕ due to the bending in the magnetic field of electrons radiating in the tracker material. As a first filtering step, superclusters are matched to track seeds (pairs or triplets of hits) in the inner tracker layers, and electron tracks are built from these track seeds. Trajectories are reconstructed using a dedicated modeling of the electron energy loss and fitted with a Gaussian Sum Filter (GSF) [43]. The filtering performed at the seeding step is complemented by a preselection. For candidates found only by the "tracker driven" seeding algorithm, the preselection is performed based on a multivariate analysis. For candidates found by the "ECAL driven" seeding algorithm, the preselection is based on the matching between the GSF track and the supercluster in η and ϕ. The few "ECAL driven" electron candidates ($\sim 1\%$ for isolated electrons) not accepted by these matching cuts but passing the multivariate preselection are also kept.

5.2.5 Jet Reconstruction

Almost every process of interest at the LHC contains quarks or gluons in the final state. While partons are not directly observable they manifest themselves through hadronization to stable particles which can then be detected in tracking chambers and calorimeters. Perturbative theory and the hadronization model describe the interaction between constituent partons of the protons and the subsequent showering into stable particles. In addition to the hard interaction effects such as the underlying event and multiple pp interactions [44], which will change the observable energy flow, also have to be modeled. The evolution of a jet from hard interaction to observable energy deposits is shown schematically in Fig. 5.3. Jet algorithms cluster energy deposits in the calorimeter or

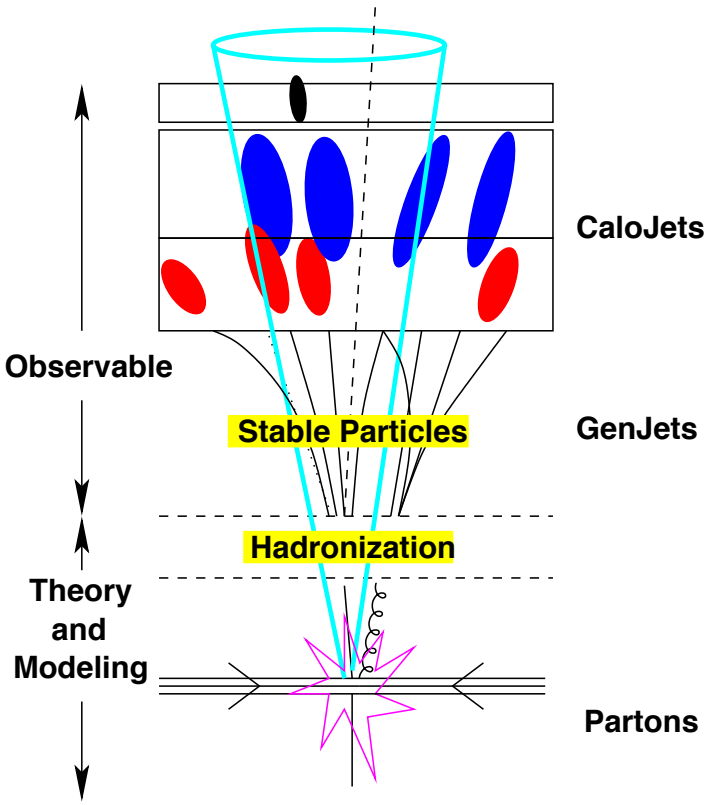

Figure 5.3: Evolution of a jet

four-vectors of particles. A successful jet algorithm will provide a good correspondence between the parton level and the particle level, where particle level refers to the stable particles remaining after the hadronization stage. Candidates found by the Particle Flow algorithm are clustered into jets using the anti-k_T algorithm [45] with a cone size of 0.5. The process of hadronization usually results in a number of hadrons in tight cone aroung the original quark or gluon direction. Hadron originating from heavy flavour quarks can decay emitting leptons. Other hadrons sometimes leave all their energy in the ECAL, so they might be confused with electrons deposit, or others can leave a track in the muon chamber. These are called *fake leptons*, since they are not part of the signal process. There are several difficulties in reconstructing the product of a quark or gluon hadronization: particles could be generated with large momentum with respect to the original parton, or there could be initial state radiation or soft radiation that contribute with additional tracks. The criteria for clustering particles into jet is the following:

$$d_{ij} = min\left(k_{ti}^{2p}, k_{tj}^{2p}\right)\frac{\Delta_{ij}^2}{R^2} \tag{5.1}$$

$$d_{iB} = p_{Ti}^{2p} \tag{5.2}$$

i and j are the particles involved in the step of the algorithm (that is iterative among the clusters of particles); d_{ij} is the distance between those and d_{iB} is the distance between the ith-esim particle and the beam line. $\Delta_{ij}^2 = (y_i - y_j)^2 + (\phi_i - \phi_j)^2$; $p_T i$,y_i and ϕ_i are with respect the transverse momentum, the rapidity and the azimuthal angle of the ith particle. p in the standard k_T algorithm was equal to 1; in the anti-k_T version is -1 (this explain the name). The algorithm compares d_{ij} and d_{iB} iteratively:

- $d_{ij} < d_{iB}$ for some j; i and j are clustered into a jet;

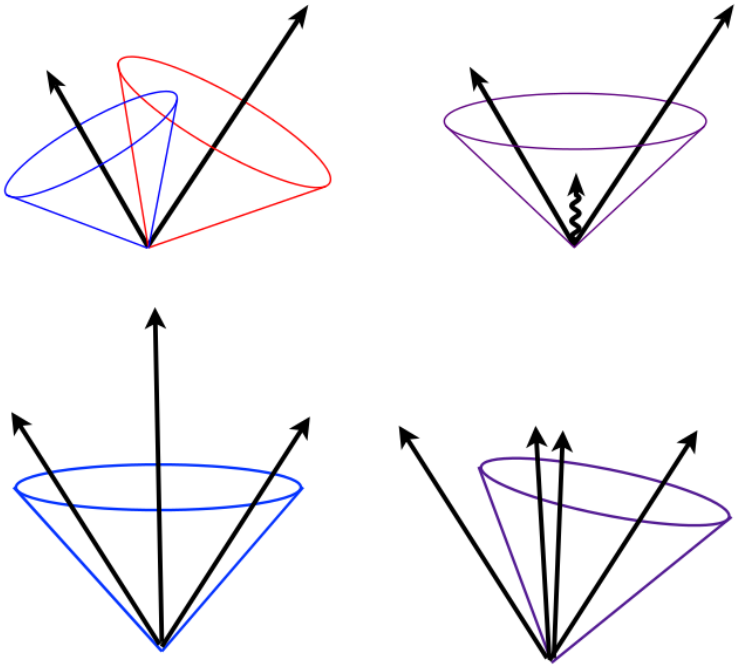

Figure 5.4: Infrared safety (top, adding a soft gluon) and Collinear safety (bottom, splitting one parton into two collinear partons) should not change the jet clustering results

- $d_{ij} > d_{iB}$ for all j: i is a jet.

Anti-k_T algorithm is now a standard tool to reconstruct jet safely respect to collinear and infrared emission. In Fig. 5.4 we can see a sketch that clarify the concept of infrared and collinear extra radiations.

5.2.6 *b*-jets Reconstruction

Several algorithms are defined with the purpose to tag jets stemming from b quarks hadronization, or b-jets. Such jets usually contain B-hadrons which present several characteristics which allow to discriminate between b-jets and jets stemming from light quark hadronization (also referred to as light jets). First of all, the tracks produced by long lived particle decays (such as B-hadrons) are expected to have a non negligible impact parameter(IP). The IP is invariant with respect to changes of the long lived particle kinetic energy, this is due to the cancellation of the boost effects on the flight path (scaling as γ and the average angle of the decay products with respect to the flight direction (scaling as $1/\gamma$). The typical scale of the IP is the one of the decaying particle $c\tau$; for a B-hadron this corresponds to about $450\,\mu m$. In CMS the IP can be measured with a precision between $30\,\mu m$ and hundreds μm. Given that the uncertainty can be of the same order of magnitude as the IP, a better observable for b-tagging is the impact parameter significance defined as

$$S = \frac{IP}{\sigma_{IP}} \tag{5.3}$$

The IP in CMS is life time signed: tracks orginating from the decay of particles travelling in the same direction of the jet are signed as positive, while those in opposite direction are tagged as negative. This is obtained by using the sign of the scalar product of the IP segment with the jet direction. On the other hand, it is possible to reconstruct the secondary vertices from B hadron decays inside of jets. To do this an adaptive vertex fit is performed. The first simple way of

Dataset	Run Range	Integrated Luminosity
/SingleMu (Electron) /Run2012A-22Jan2013-v1 /AOD	190450-193621	876.164 pb^{-1}
/SingleMu (Electron) /Run2012B-22Jan2013-v1 /AOD	193833 – 196531	4405.519 pb^{-1}
/SingleMu (Electron) /Run2012C-22Jan2013-v1 /AOD	198022 – 203742	7049.058 pb^{-1}
/SingleMu (Electron) /Run2012D-22Jan2013-v1 /AOD	203777 – 208686	7369.0 pb^{-1}

Table 5.1: Data and Integrated Luminosity

producing a discriminator based on track impact parameters is an extension of the so-called Track Counting algorithm used in past experiments. The track counting approach identifies a jet as a b-jet if there are at least N tracks each with a significance of the impact parameter exceeding S. Currently two algorithms are defined: Track Counting High Purity, for N = 3, and Track Counting High Efficiency, with N = 2. Other algorithms are available in the CMS reconstruction but they will not be described since they have not been used in this study.

5.2.7 Missing Transverse Energy

Neutrinos do not interact in the detector hence their presence creates an energy imbalance which can be measured, E_T^{miss} . At a hadron collider such as the LHC, the energy imbalance is computed in the transverse view only, since the longitudinal momentum of the individual colliding partons is not known (just the longitudinal momentum of the whole proton can be measured) and only the transverse momentum of the colliding partons can be assumed with a large precision to be zero. The particle flow algorithm reconstructs the missing transverse energy E_T from the vectorial sum of all the candidates transverse momentum. In order to have the best definition of the $E_{T^{miss}}$ special care must be taken in the evaluation of the calorimeter noise. A cleaning algorithm to reduce the detector noise is applied to the calorimeter hits themselves, before the rest of the event reconstruction.

5.3 Trigger and Datasets

As we said before, the center of mass energy at the LHC reached during 2012 was $\sqrt{s} = 8\,\text{TeV}$. The luminosity reached during the data taking was of 19.7 fb^{-1}, known within 4.0% - a plot of the luminosity reached by the LHC during 2012 is shown in Fig. 5.5. The collision events used for the analysis are taken from the SingleMu and SingleElectron Primary Datasets, selected using specific HLT paths that select events with at least one high energy lepton (muon or electron). The exact nomenclature of the paths used is the following:

- `HLT_IsoMu24_eta2p1`
- `HLT_Ele27_WP80`

In practice this means that events are selected requiring either a muon with $p_T > 24GeV/c$ and $|\eta| < 2.1$ or an electron with $E_T > 27GeV$ and tracking identification criteria yielding an electron selection efficiency of 80%. In order to reproduce the effect of the online selection on Monte Carlo, the events are weighted with and η-dependent efficiency derived from data.

In each run the luminosity sections flagged as bad according to the validations performed by each Detector Performance Group (DPG) and Physics Object Group (POG) are excluded. Tab. 5.1contains the run ranges used for the present analysis.

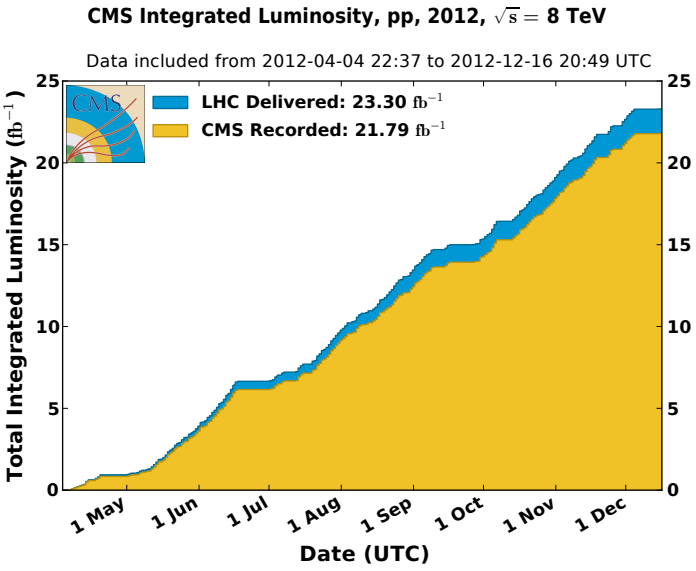

Figure 5.5: Integrated luminosity cumulative distribution

Chapter 6

Analysis Strategy

Starting from the observation that the top partner single production considered here and the Standard Model single top production share the same list of objects in the final state, we would like to exploit as much as possible the similarities between the two analysis to simplify several technical aspects. The dominant Feynman diagram for the process is the same: As it will become clear in the following a simple recasting of the single top analysis ([46] and [4]) is not possible given the different kinematical regime of the new Top Partner signal and a new strategy for signal to background optimization will be described. However, we will make use the same analytical tools and backgrounds, but for the signal we will use the events generated by us with Madgraph.

6.1 Event pre-selection

Given the final state that we expect, the initial pre-selection of the events witll require the presence of a reconstructed lepton and neutrino (from the Missing Energy), represetning the decay products of the W boson; a b jet from the decay of the $\tilde{T}$, from the decay of the Top Partner, and an untagged jet, that is the forward jet. The exact requirements imposed on the various objects are the following:

- MUON:
  1. $p_T > 26\,\mathrm{GeV}$;
  2. $GlobalMuon$;
  3. $PFMuon$;
  4. $|\eta| < 2.1$;
  5. $\chi^2_{norm} < 10$;
  6. At least 5 valid hits in the silicon tracker;
  7. At least 2 segments must match the global muon object in the muon chambers

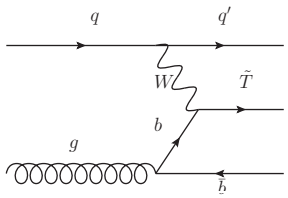

Figure 6.1: $\tilde{T}$ single production feynman diagram

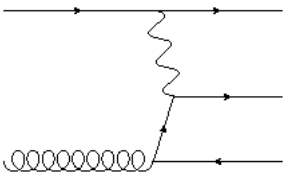

Figure 6.2: Standard Model top quark single production feynman diagram

8. At least one hit in the inner tracker;
9. $I_{rel} = \frac{I^{ch.h}+max((I^{\gamma}+I^{n.h.}-I^{PU}),0)}{p_T}$, with $I^{ch.h}, I^{\gamma}, I^{n.h.}, I^{PU}$ respectively the sum of the transverse energies deposited by stable charged hadron, photons, neutral hadrons, in a cone size of $\Delta R = \sqrt{(\Delta\eta)^2 + (\Delta\phi)^2} < 0.4$; $I^{PU} \equiv 0.5 \times \sum p_T^{PU}$ is the sum of transverse momenta of tracks associated to non-leading vertices, used to estimate contributions from pileup events (0.5 refelcts the ratio neutral-to-charged, from isospin invariance). $I_{rel} < 0.12$.

- ELECTRON:

1. $p_T > 30\,\text{GeV}$ (ECAL driven);
2. $|\eta| < 2.5$;
3. $|\eta_{SuperCluster}| > 1.5660$ && $|\eta_{SuperCluster}| < 1.4442$ not considered;
4. pass Conversion Veto;
5. $I_{rel} = \frac{I^{ch.h}+max((I^{\gamma}+I^{n.h}-\rho\times A),0)}{p_T}$; here the correction from pileup events is performed by subtracting the average density ρ over the $\eta-\phi$ space of particles not used to reconstruct jets, multiplied by an "effective area" A (effective portion in the $\eta - \phi$ space available for the energy deposit of PU particles inside of the isolation cones around the electron momentum direction). $\Delta R < 0.3$ and $I_rel < 0.1$.

- JETS:

1. anti-k_T , $\Delta R < 0.5$;
2. at least 2 constituents;
3. $p_T > 40\,\text{GeV}$
4. $|\eta| < 4.5$;
5. charged hadron energy fraction more than 1;
6. charged Hadron Multiplicity > 1;
7. charged Em Energy Fraction< 0.99;
8. neutral Em Energy Fraction< 0.99;
9. neutral Hadron Energy Fraction < 0.99;
10. the average energy density ρ in the $\eta - \phi$ space of neutral particles not clustered into jets is used to extrapolate the energy due to pileup interactions.

- B-TAGGING: Track Counting High Purity algorithm [47] is used to reconstruct jet stemming from b-quarks hadronization. The Pysics Object Group (POG) supports one threshold (of the discriminator) for this algorithm at the moment, corresponding to a value of 3.41. The advantage of sticking to these reference points lies mostly in the fact that the data/simulation scale factors and corresponding uncertainties on efficiencies and mistag rates have been evaluated

elsewhere [48]. The efficiency in simulated signal events with one identified lepton and two jets,is 43% for jets matched to a b-quark at generator level within $\Delta R < 0.3$, $p_T > 40\,\text{GeV}$, in the acceptance of the trackers ($|\eta| < 2.5$). For our purpose this is not the optimal choice for the optimization of the efficency in the reconstruction of the signal - but we can not change any feature for this analysis, since we can not modify the backgrounds MonteCarlo already produced. This will be included in the new analysis targeted at the 13 TeV run of the LHC in 2015.

Events with an additional lepton that passes some looser selections are rejected ($p_T < 10\,\text{GeV},\ |\eta| < 2.5,\ I_{rel} < 0.2$ for muons; $E_T < 20\,\text{GeV},\ |\eta| < 2.5,\ I_{rel} < 0.2$ for electrons). Events with very high energy noise in the HCAL barrel or endcaps are rejected, using pulse shape, hit multiplicity, and timing criteria. The missing transverse momentum $\not{p}_T$ is defined as the negative of the vectorial sum of the transverse momenta of all reconstructed PF particles. $\not{E}_T$ is defined as the magnitude of the transverse momentum vector. The transverse mass is defined as:

$$m_T = \sqrt{\left(p_T^l + \not{E}_T\right)^2 - \left(p_x^l + \not{p}_x\right)^2 - \left(p_y^l + \not{p}_y\right)^2} \tag{6.1}$$

Stating that we are at higher energies, we omitted the requirements of $m_T > 50\,\text{GeV}$, as it was in the single top reference, beacause we did not have so much contribution from QCD events. Equally, in the electron channel we did not require $\not{E}_T > 45\,\text{GeV}$, for the same reason. HT and ST are defined as the scalar sum of the transverse momenta of the particles in the event:

$$HT = \sum_{i=l,b,j'} p_T \tag{6.2}$$

$$ST = HT + \not{E}_T \tag{6.3}$$

Events are divided in categories according to the number of jets and tags, using the wording "N-jets M-tags". We refer to events with N jets M of which are tagged as b. The categories enriched in top-partner production that will be considered in the following are the 2J-1T and 3J-1T. The variable $|\eta_{j'}|$ is defined as the pseudorapidity of the non-tagged jet in the 2J-1T and 3J-2T; in 2J-0T is the sum of the two jets pseudorapidity and in 3J-1T is the psuedorapidity of the jet with lower value of the b-tag discriminator. The majority of the backgrounds surviving the final selection contain an actual b-jet, the main exception being W/Z+c jets. This algorithm was chosen over others because of the discriminating power with respect to this particular background.

In the following figures there are plots of the standard variables of the reconstructed events; we can see how strong is the requirement of having a fixed number of jets in our events. The efficiency of the b-tagging algorithm is another source of loss of events. In 6 tables and plots of the efficiency of the selections are given.

In the following figures the standard kinematical variables of the recounstructed objects are shown. There are different scenarios: with and without the PileUp reweighting. The effects of the PileUp in such a type of events is negligible. The cut in RMS, used in SingleTop to discriminate jets of the signal from PileUp jets, has no effect in our samples. This is because of the striking signature of the top-partner single production.

6.1.1 Top Partner Mass Reconstruction

To reconstruct the top-partner invariant mass we combine the information from the kinematical distribution of the lepton, b-tagged jet and neutrino. This is a process already studied in literature, the main reference is [49].There is an uncertainty in the choice of the right longitudinal momentum of the neutrino. This is due to the intrinsic nature of neutrino, that we measure as a missing energy,

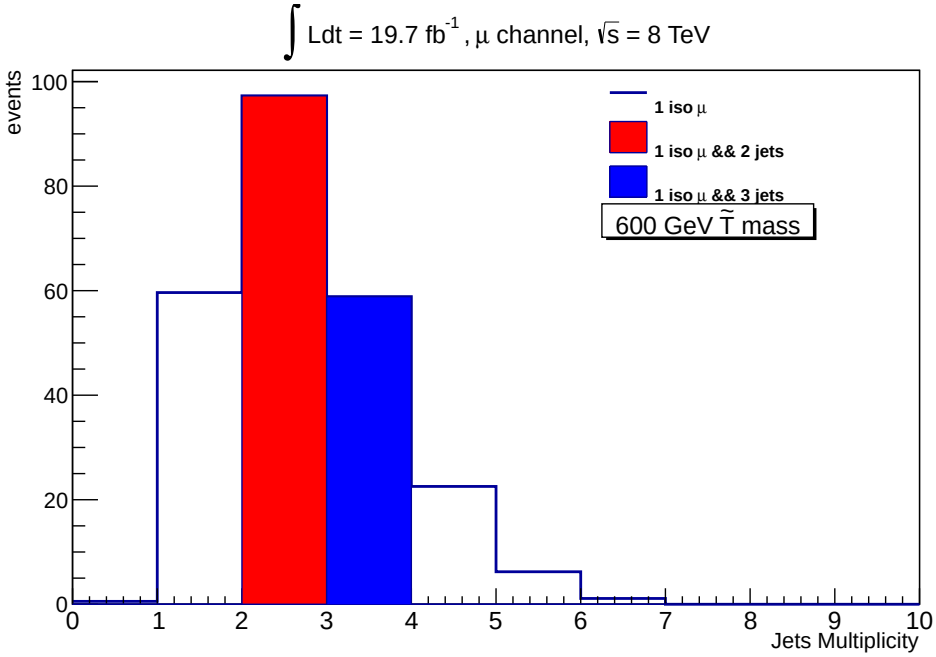
∫ Ldt = 19.7 fb-1 , μ channel, √s = 8 TeV
events
Jets Multiplicity
1 iso μ
1 iso μ && 2 jets
1 iso μ && 3 jets
600 GeV T̃ mass

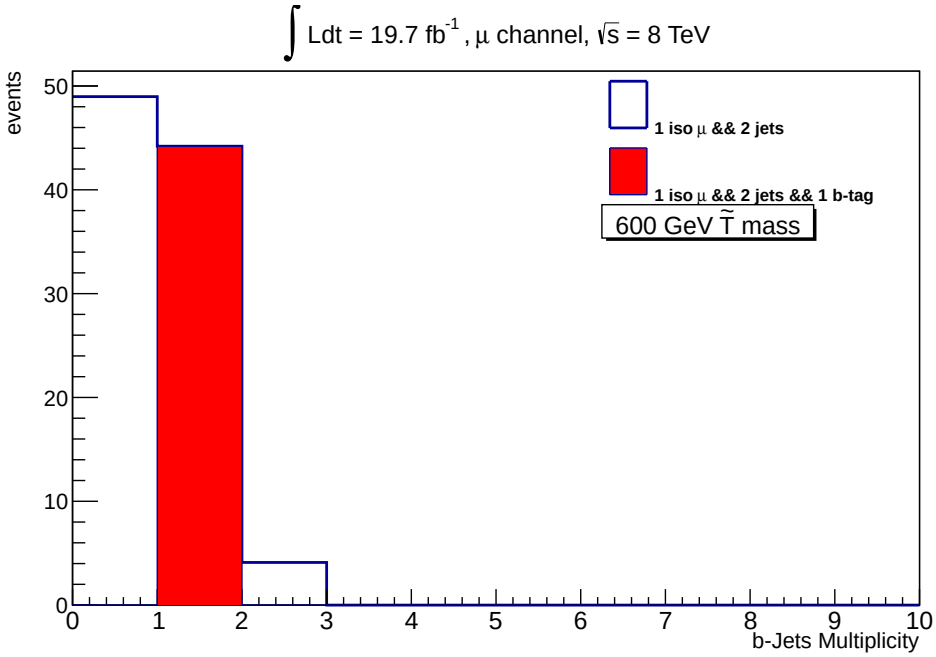
∫ Ldt = 19.7 fb-1 , μ channel, √s = 8 TeV
events
b-Jets Multiplicity
1 iso μ && 2 jets
1 iso μ && 2 jets && 1 b-tag
600 GeV T̃ mass

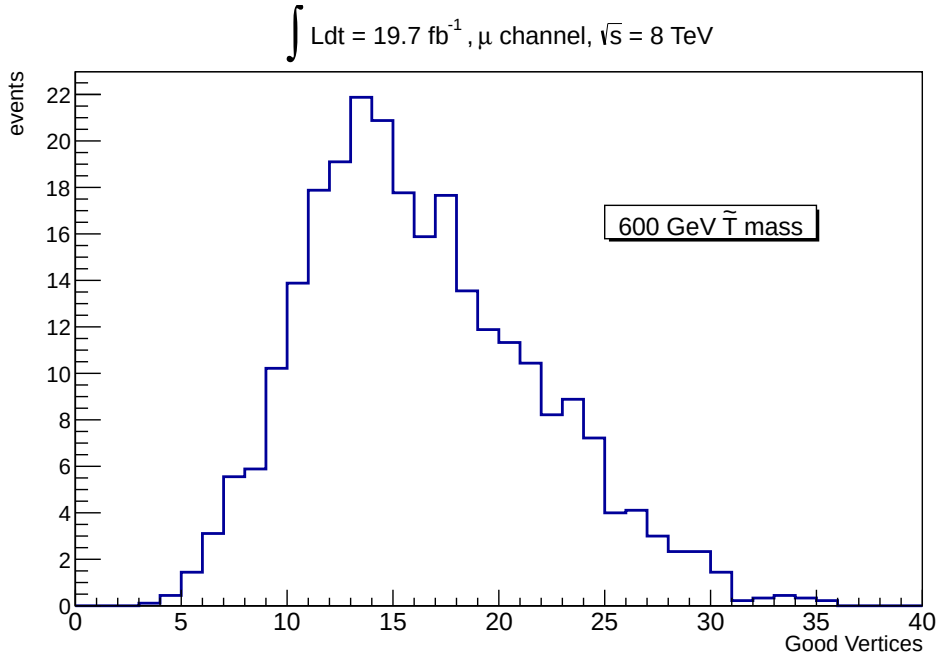

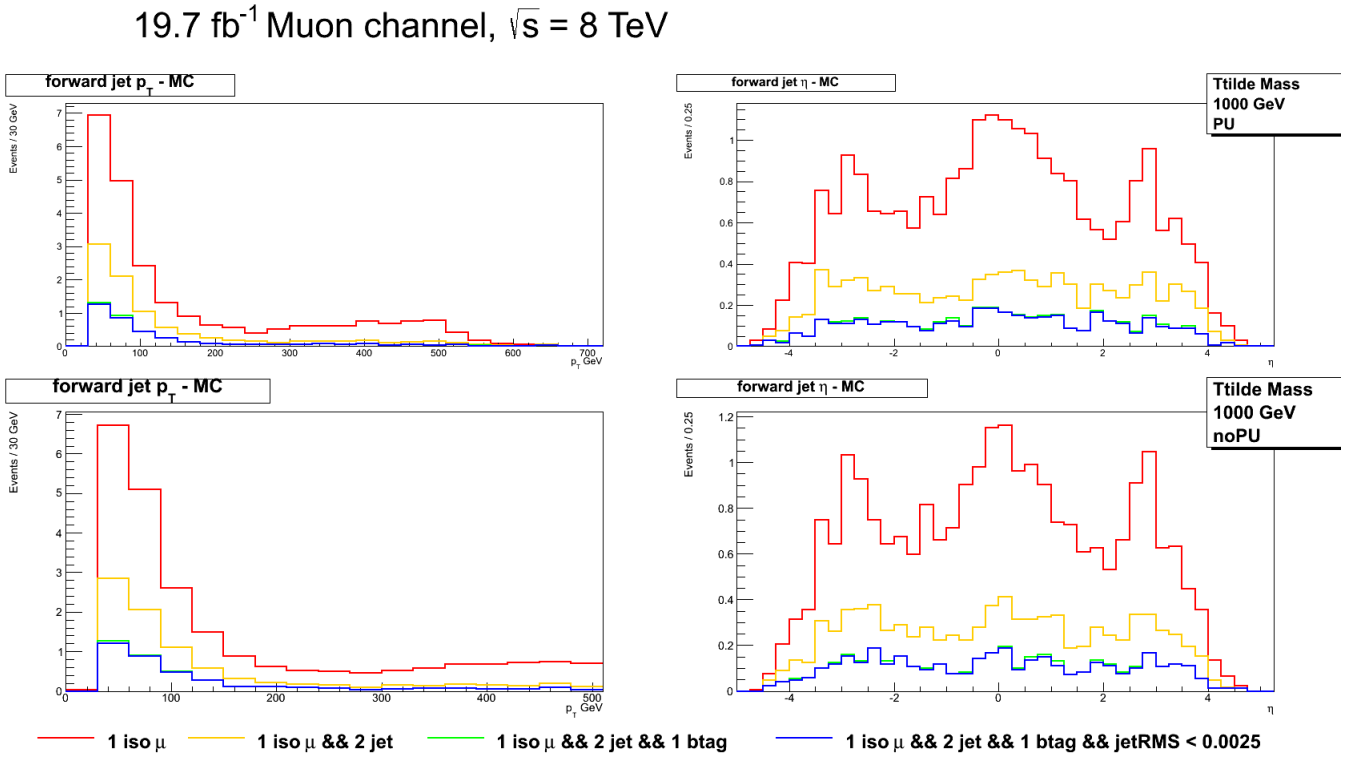

Figure 6.3: Forward jet distributions and selections

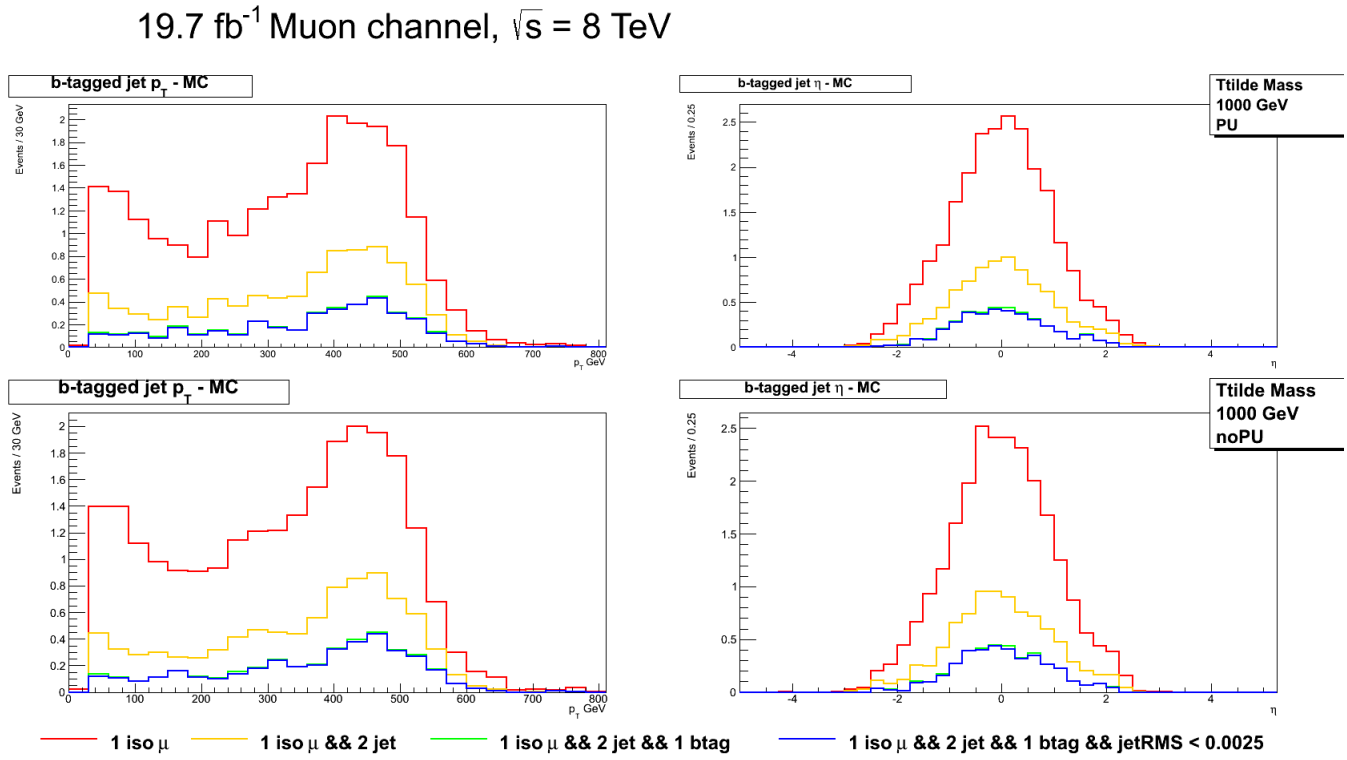

Figure 6.4: b-tagged jet distributions and selections

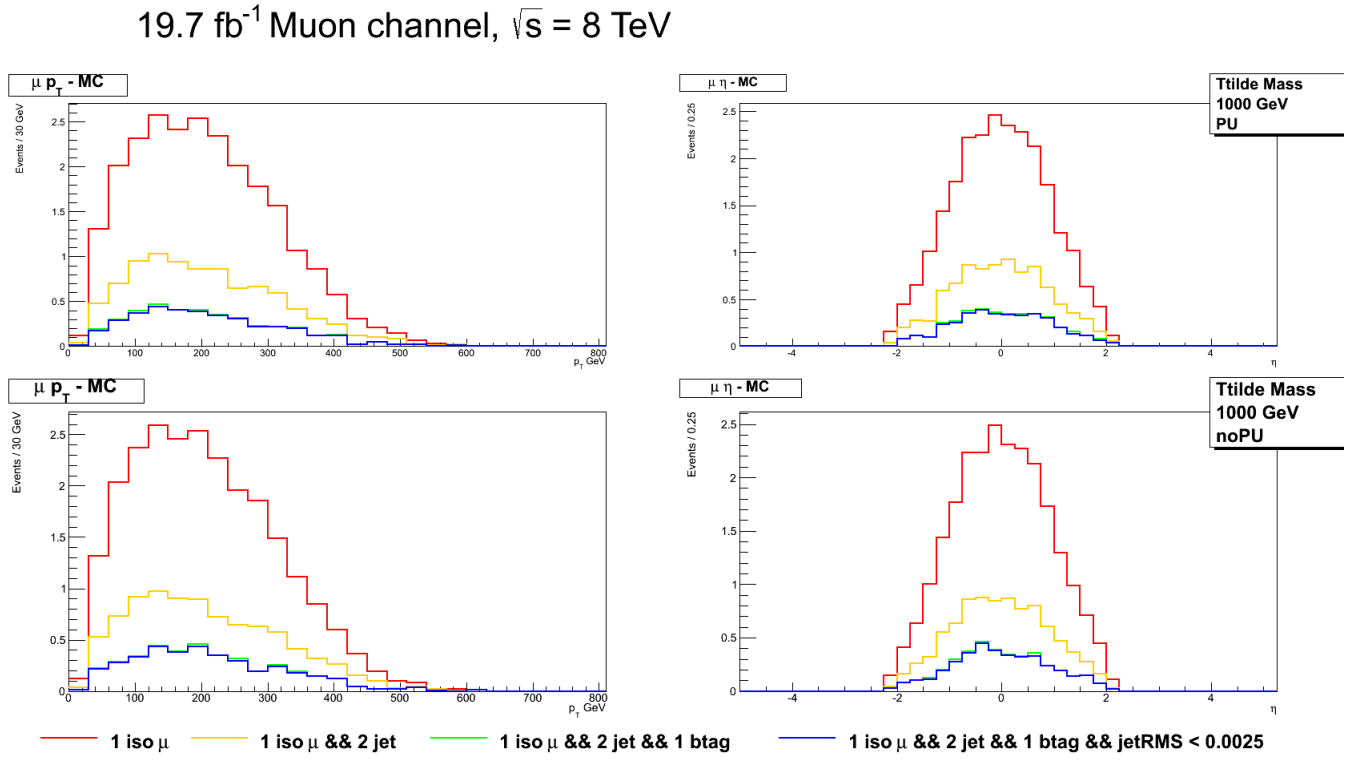

Figure 6.5: Muon distributions and selections

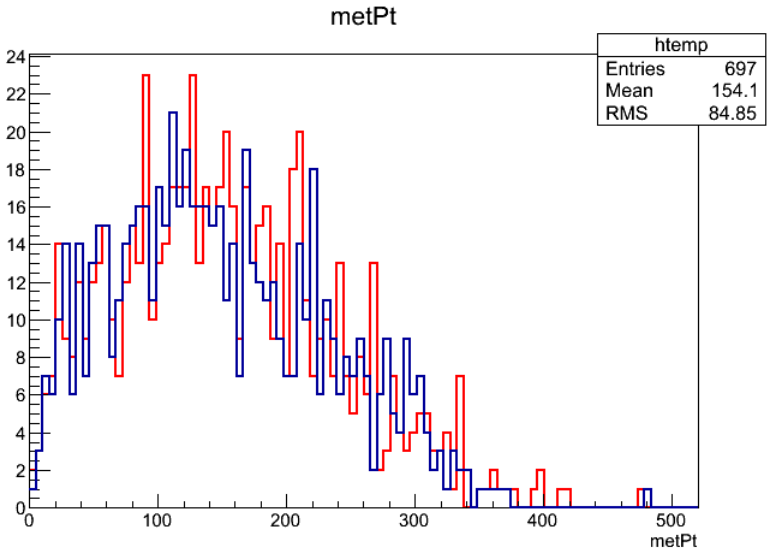

Figure 6.6: Missing Transverse Energy with PileUp reweighting (red line) and without (blue line)

then we do not have all the information. So a constraint, from the decay of the W boson is used. Assuming that all the x and y component of the $\not{E}_T$ is due to the escaping neutrino, we could write

$$m_W^2 = \left(E_l + \sqrt{\not{E}_T{}^2 + p_{z,\nu}^2}\right)^2 - \left(\mathbf{p}_{T,l} + \not{\mathbf{E}}_T\right)^2 - \left(p_{z,l} + p_{z,\nu}\right)^2 \tag{6.4}$$

This equations have in general two solutions

$$p_{z,\nu} = \frac{\Lambda \cdot p_{z,l}}{p_{T,l}^2} \pm \sqrt{\frac{\Lambda^2 \cdot p_{z,l}^2}{p_{T,l}^4} - \frac{E_l^2 \cdot \not{E}_T^2 - \Lambda^2}{p_{T,l}^2}} \tag{6.5}$$

where

$$\Lambda = \frac{m_W^2}{2} + \mathbf{p}_{T,l} \cdot \not{\mathbf{E}}_T \tag{6.6}$$

If the discriminant in 6.5 becomes negative ($m_T > m_W$), the solutions have an imaginary component. This happens in 36 % of the cases (referenza SingleTop), mostly due to the finite $\not{E}_T$ resolution. The imaginary component is eliminated modifying $\not{E}_T$ in order to reproduce $m_T = m_W$; this is done requiring the discriminator (then the square root in 6.5) is null. Therefore the smallest solution for $p_{z,\nu}$ is chosen.

6.2 Improving the signal-bakground discrimination

The background is defined as a process which phenomenological signature could be identified as the signal. Background evaluation is one of the most important step of an analysis: we have to consider all the possible sources that can mime the signature of the signal. The background contributions are often divided into physical and unphysical processes. The latter are due to instrumental effects. Physical backgrounds are instead processes that end in the same final state, both at generator and at showering level. Exploiting the similarity of the top partner process and single top one it is obvious to infer not only that they share similar backgrounds but that the single top process itself is a background for our BSM signal. Coherently with the goals of this work, in this section we will compute an eximation of the background processes, and we will describe the set of cuts we

thougth to gain a better significance between signal and backgrounds. The final goal of the thesis is to place some bounds on the production of $\tilde{T}$ at the Large Hadron Collider with $\sqrt{8}$ TeV. This is the list of the background actually considered:

- W + jets;
- $t\bar{t}$;
- single top t-channel;
- single top s-channel;
- di-boson;
- Z + jets;
- tW - channel;
- QCD multijets;

All the backgrounds processes have been simulated with $MADGRAPH$ interfaced to $PYTHIA$ and simulated with the CMS Full Simulation. The value of the top-quark mass used in all simulated samples is $m_t = 172.5 GeV/c2$. All samples use the CTEQ6.6 parton distribution functions, while the factorisation and renormalisation scales are both set to $2m_t$. In order to check the initial signal to background we superimposed the signal to the stack of the backgrounds, on a 400 GeV window in the reconstructed "top partner" mass: we found a low level of significance, mostly due to the low production cross section used for the signal, but also for a significant contribution of backgrounds even in the high mass tails. A new selection needs to be devised. Concerning the production section, we would like to remind the reader that the one used here is only one possible choice. As seen in previous chapters our model has some parameters to tune; we can always choose a new set of parameters that enhances the cross section. See for instance in Fig. 3.4 in chapter 3 how much the cross section can be enhanced. For example, one of the reference in the literature [50] has chosen a cross section surely higher, without loss of generality. The consequence is that we will put a bound in different region of the parameters space. Then we had to change the strategy, in order to reach the goal of our thesis; however it is necessary a debat on the loss of shape of the reconstructed invariant mass, that has not a sharp peak at the right mass value of the top partner. In the next chapter we will give some arguments that could explain the particular behaviour of the reconstructed invariant mass. A table with the nominal cross section used for the top partner production can be find at Tab. 3.2 in chapter 3, instead Tab. 6.1 contain the cross sections of the Standard Model background processes. Figs. 6.7, 6.8 describe the difference in the scenario at $\tilde{T}$ mass of 800 GeV, with and without the pseudo-rapidity cut, as described in [46].

Process	Cross Section (pb)	Datasets
tW	22.2	`T_ tW-channel-DR_ TuneZ2Star_ 8TeV-powheg-tauola`
t s-channel	5.4	`TToLeptons-s-channel_ 8TeV-powheg-tauola`
t t-channel	86.4	`TToLeptons-t-channel_ 8TeV-powheg-tauola`
$Zjets$	3503.3	`DYJetsToLL_ M-50_ TuneZ2Star_ 8TeV-madgraph`
$Wjets$	36257.2	`Wn`JetsToLNu-TuneZ2Star_ 8TeV-madgraph
Di-boson WW	54.3	`WW_ TuneZ2Star_ 8TeV-pythia6-tauola`
Di-boson ZZ	8.05	`ZZ_ TuneZ2Star_ 8TeV-pythia6-tauola`
Di-boson ZW	32.66	`WZ_ TuneZ2Star_ 8TeV-pythia6-tauola`
$t\bar{t}$	234	`TTJets_ SemiLeptMGDecays_ 8TeV-madgraph`

Table 6.1: Backgrounds cross sections - The samples are generated either inclusively or with a final state restricted to the leptonic mode; Leading Order where not indicated - all crosse sections are taken from [4]

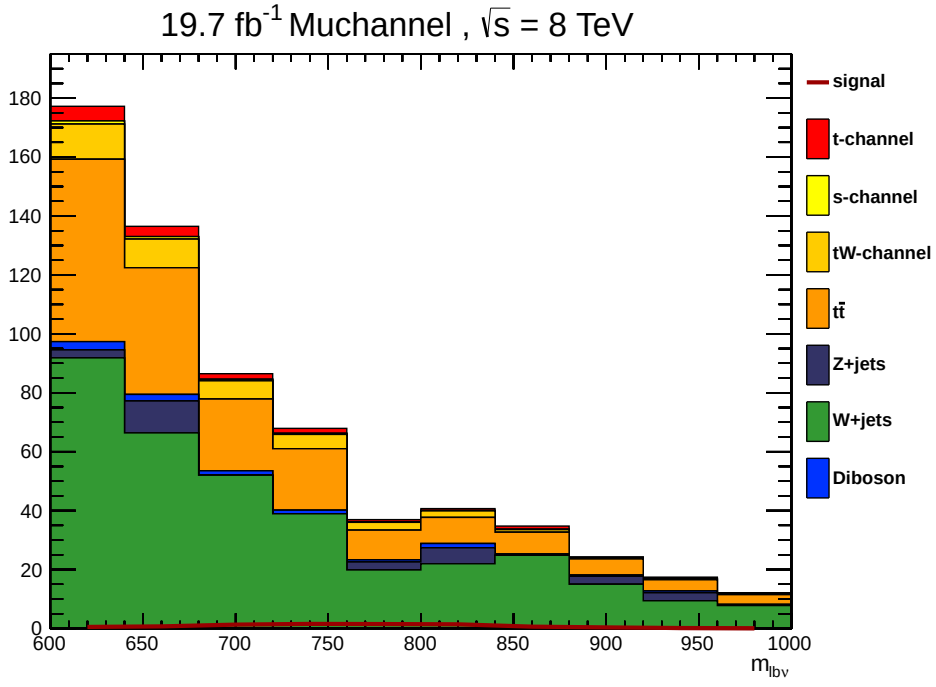

Figure 6.7: Signal and backgrounds - no cuts - 800 GeV $\tilde{T}$ mass

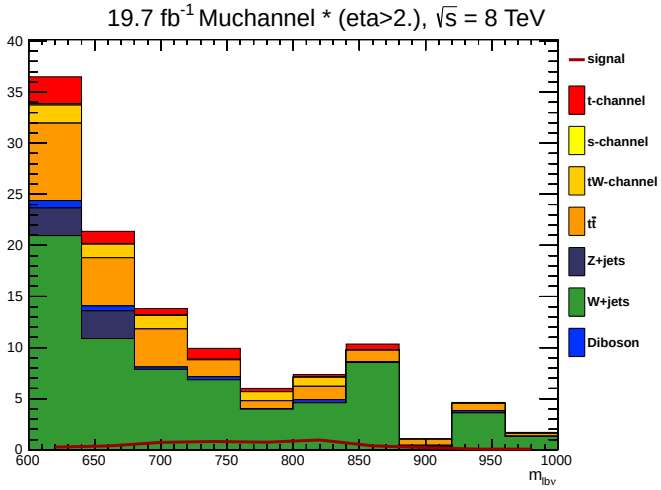

Figure 6.8: Signal and backgrounds - $\eta > 2.0$ - 800 GeV $\tilde{T}$ mass

However, we have observed that the top-partner invariant mass (reconstructed in this way) is not a good variable to exploit for the exctraction of the signal. A better way to place a bound in the $\tilde{T}$ production could be a fit in the shape of $\eta_{j'}$ that is a discriminating variable of the process. So we pass from a cut-and-count to a shape fit strategy. The evaluation of the significance is an important step in such an analysis; compatibly with the directives of the CMS statistical group, we compute the significance as

$$s = 2(\sqrt{S+B} - \sqrt{B})\,, \tag{6.7}$$

rather than

$$s = \frac{S}{\sqrt{S+B}} \tag{6.8}$$

the reason is dictated by the particular situation, composed by few events of signal and a larger number of background events. Tab. 6.2 contain the values of significance we have computed at this step of the analysis.

Mass (GeV) and cut	Signal (events)	Backgrounds (events)	$S/\sqrt{S+B}$
600	51	3681	0.84
700	18	1436	0.48
800	8	634	0.32
900	5	294	0.29
1000	3	165	0.24
$\eta_{j'} > 2.0$			
600	30	569	1.24
700	10	232	0.60
800	4	112	0.42
900	2	50	0.39
1000	0 (0.31)	30	0.31

Table 6.2: Number of events and significance for 2J-1T sample, muon channel

6.2.1 The new kinematical selection

Having made the observation that a cut-and-count (in the top-partner invariant mass variable) strategy would not have been the right choice for such a situation, we decided upon a fit in the forward jet pseudo-rapidity, that is discriminat for those reasons we have cited above. This means that we will avoid the use of the psuedo-rapidity $|\eta_{j'}|$ for a cut, and we have to improve the signal-background ratio using different variables. The main features of the kinematics of the $\tilde{T}$ production in single channel have to be exploited. The most important feature is that we are dealing with a heavy particle. Some consequences:

- hardness of the process;
- the decay of the $\tilde{T}$ is almost back to back;
- the W boson produced in the process has a high energy (it is "boosted"), then its decay products are collinear at most;
- the forward jet is not "fat";
- the forward jet and and the b-tagged jet are back to back;

We chose to evaluate only the most important sources of backgrounds,that are WJets and TTBar, we can check directly in the figure6.7. First of all we checked all the variables of the various samples we had to deal with. A list of those:

- lepton, b-tagged jet, forward jet p_T and η;
- $m_{l\nu b}$ top partner invariant and transverse mass - described in the previous chapter;
- $HT = \sum_{i=l,b,j'} p_T^i$; scalar sum of the transverse momenta of the lepton, the b-tagged jet and the forward jet;
- $ST = HT + p_T^{\nu_l}$;
- $dR(l,b) = \sqrt{\Delta^2\eta_{lb} + \Delta^2\phi_{lb}}$; a measure of the distance between the b-tagged jet and the lepton;
- $dPhi_{l\nu} = |\Delta\phi_{l\nu}|$; azimuthal angle between the lepton and the candidate neutrino from the missing transverse energy measured, from the decay of the W gauge boson from the $\tilde{T}$;
- E_T - weighted root mean square (RMS) of the forward and b-tagged jet towers' ϕ;
- $p_T^{j'b} = \sqrt{(\mathbf{p_T}^{j'} + \mathbf{p_T}^{b})^2}$, vectorial sum of the transverse momenta of the forward and b-tagged jet.

To decide the right value for every cut, we tried different values valuating every plot for every sample and superimposing them and valuating the signficance of the background-signal discrimination. So here a list of the cut we thought to:

1. reconstrucion and jets selection;
2. $HT > 300 - 350 - 400 - 450 - 500\,\text{GeV}$;
3. $ST > 400 - 450 - 500 - 550 - 600\,\text{GeV}$;
4. $dR(l,b) > 2.0$;

5. $|dPhi(l,\nu)| < 1.5$;
6. $m_{l\nu b}$ 400 GeV windows size;
7. $bJetPt > 140 - 175 - 210 - 245 - 280\,\text{GeV}$;
8. $m_T^{l\nu b} > 400 - 500 - 600 - 700 - 800\,\text{GeV}$;
9. fJetRMS && bJetRMS < 0.05;
10. $p_T^{j'b} > 120 - 150 - 180 - 210 - 240\,\text{GeV}$;
11. $\eta_{j'} > 2.0$;

The plots here below are all taken from the sample $2J\_1T$, in the muon channel. In every canvas there are five pads, one for every mass of the top partner, and there is the pad with the backgrounds quoted before, for the scenario of 800 GeV of $\tilde{T}$ mass.

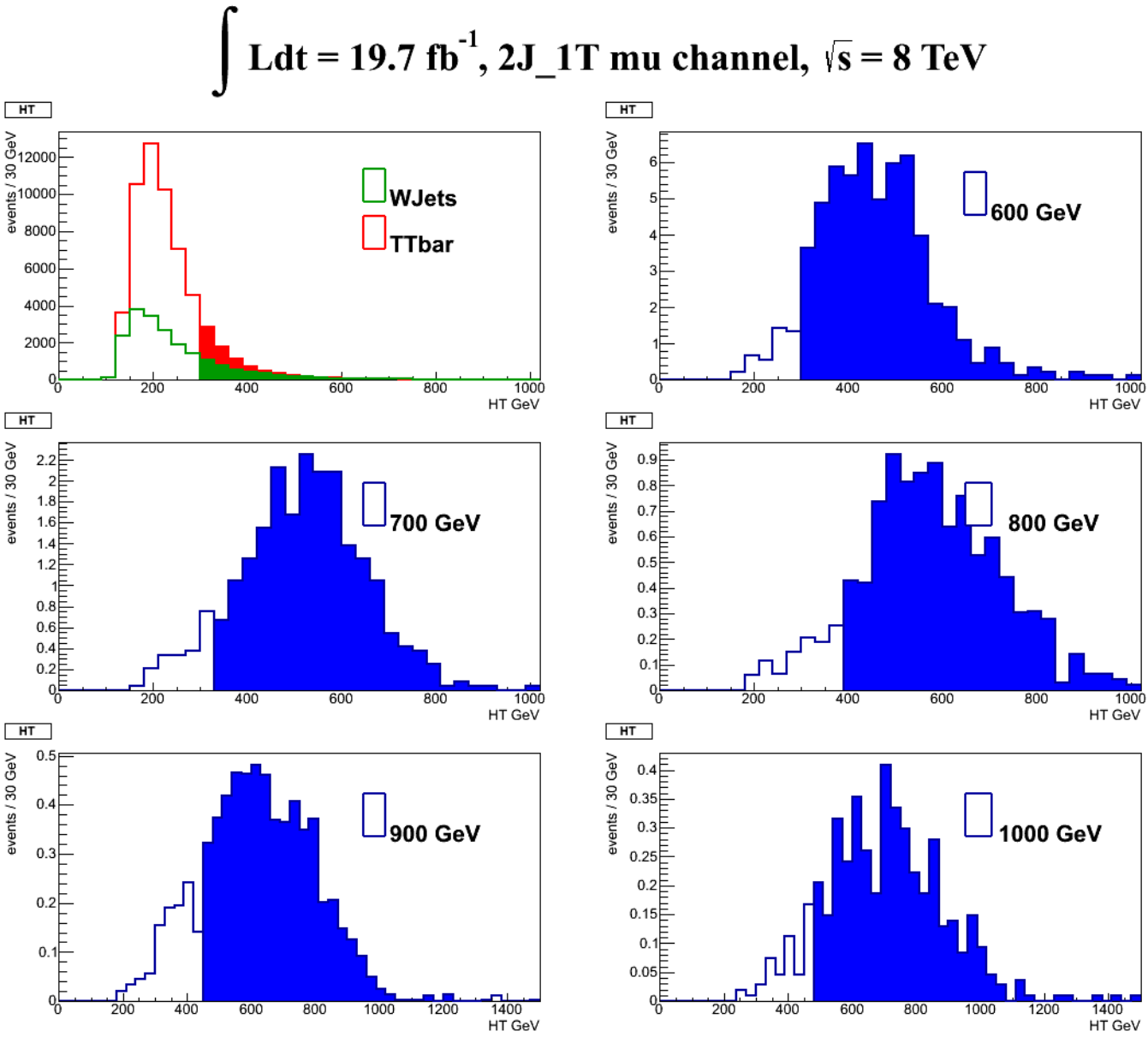

Figure 6.9: HT; cut values: 300-350-400-450-500 GeV

In these two plots we can see the difference between the shape and the values of the signal sample and the backgrounds ones; as we stated, our process is harder than SM ones. This is due to the heaviness of the particle that decays. We also studied the correlation between HT and ST in our process, in order to understand if both two cuts were efficient. Then we plotted HT with a cut in ST and viceversa, so we understood that that was not a large correlation between these two variables in the sample; a cut in ST after a selection in HT is substantially a cut in the missing transverse energy. We plotted similar histograms also for the backgrounds:

The angular variables are very important for a discrimination of such a process, the W boson of the Standard Model processes is not boosted as in our case. This property reflects in our signal in the collinearity of the lepton and the neutrino present in the decay. To support this idea,in Fig. 6.14 there is the parton level transverse momentum of the reconstructed W.

Instead, in the 6.15, we can state that the $\tilde{T}$ is produced at rest. Choosing a 400 GeV window in the top partner reconstructed invariant mass would be a very good cut if the variable wasn't affected by the problems we have seen. However it has a good discriminant power, since in Standard Model processes the invariant mass reconstructed is peaked at top-quark mass values. Even though we miss too much signal events we opt for this cut. An additional cut on the transverse mass of the reconstructed object helps little, because the transverse mass is slightly peaked at lower values than the complete invariant mass.

We have theoretical reasons to suppose that the forward jet produced in the $\tilde{T}$ decay process is less "fat" than those produced in Standard Model processes; also the b-tagged jet has this feature, probably due to its hardness.

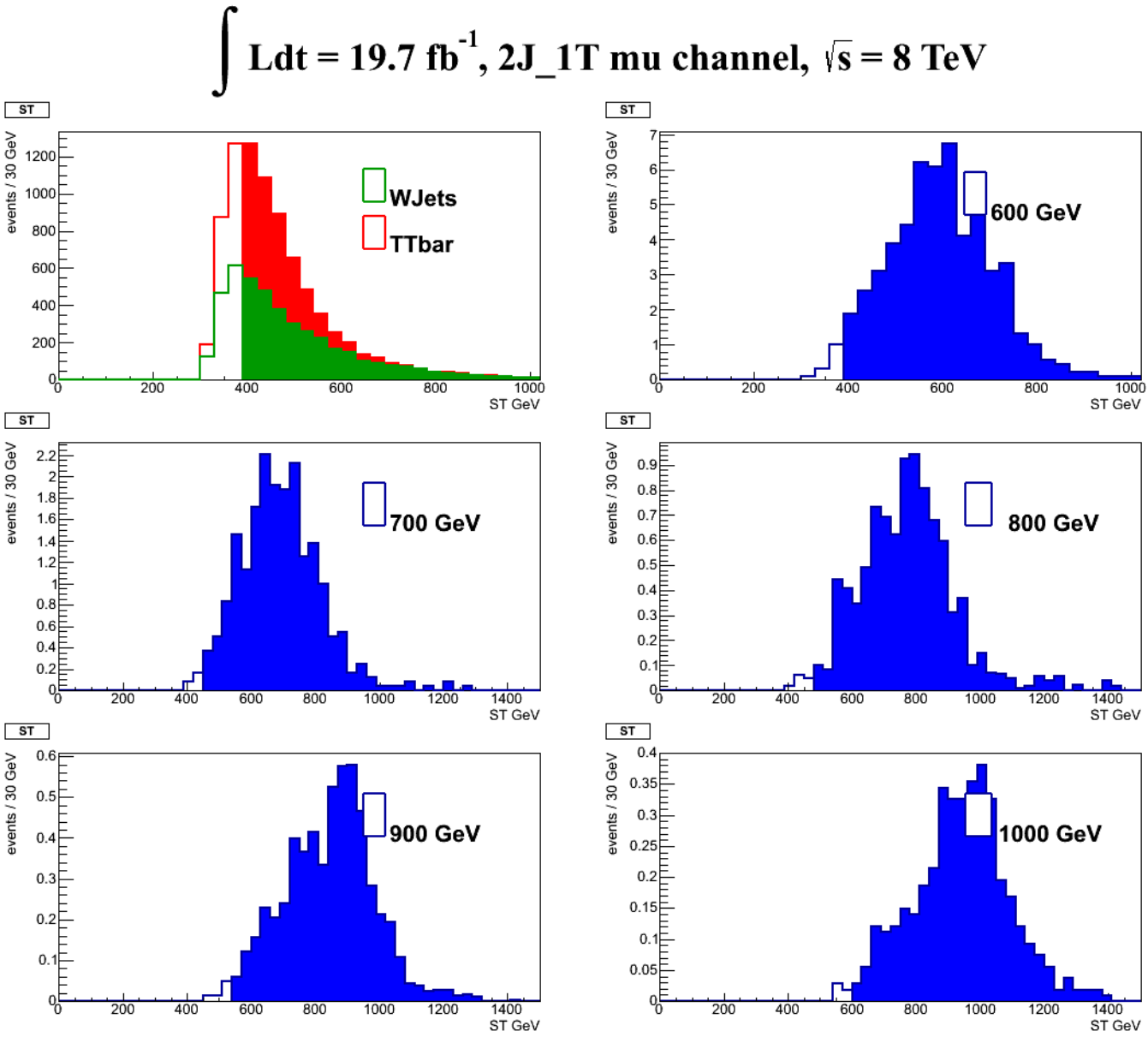

Figure 6.10: ST; cut values: 400-450-500-550-600 GeV

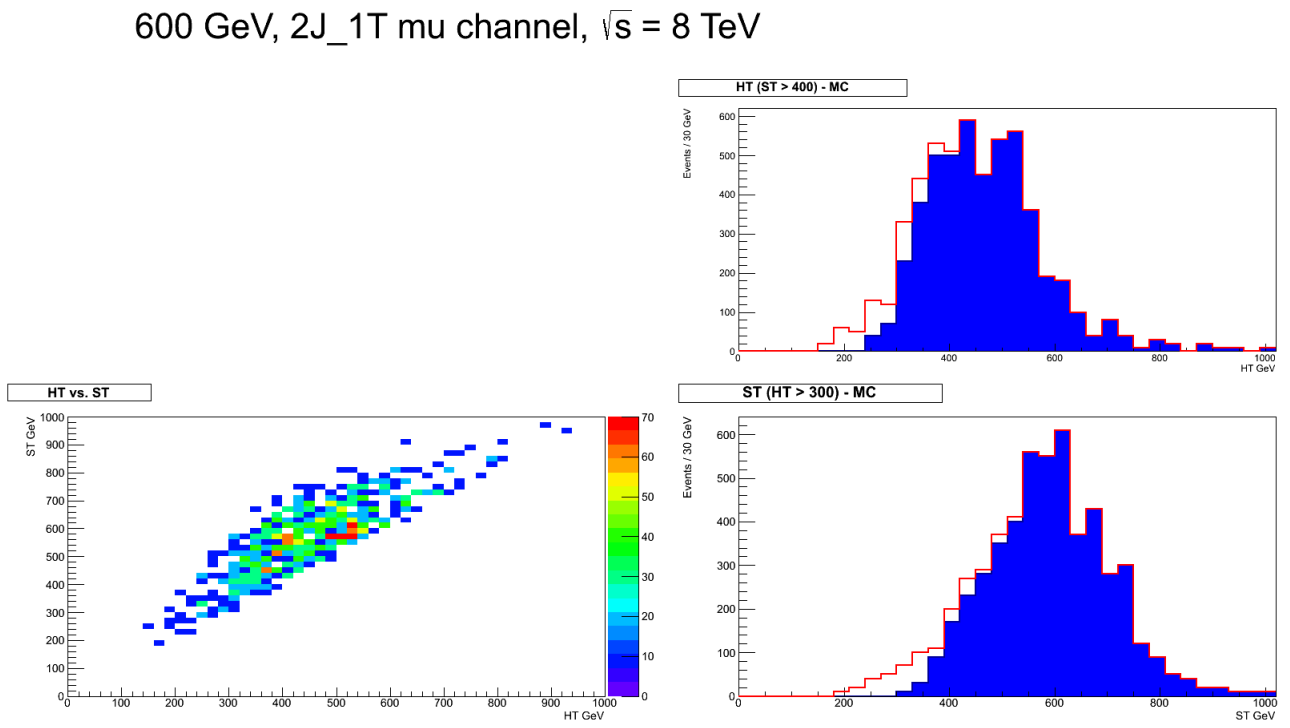

Figure 6.11: Study of the correlation of the transverse momenta scalar sum variables: 600 GeV sample

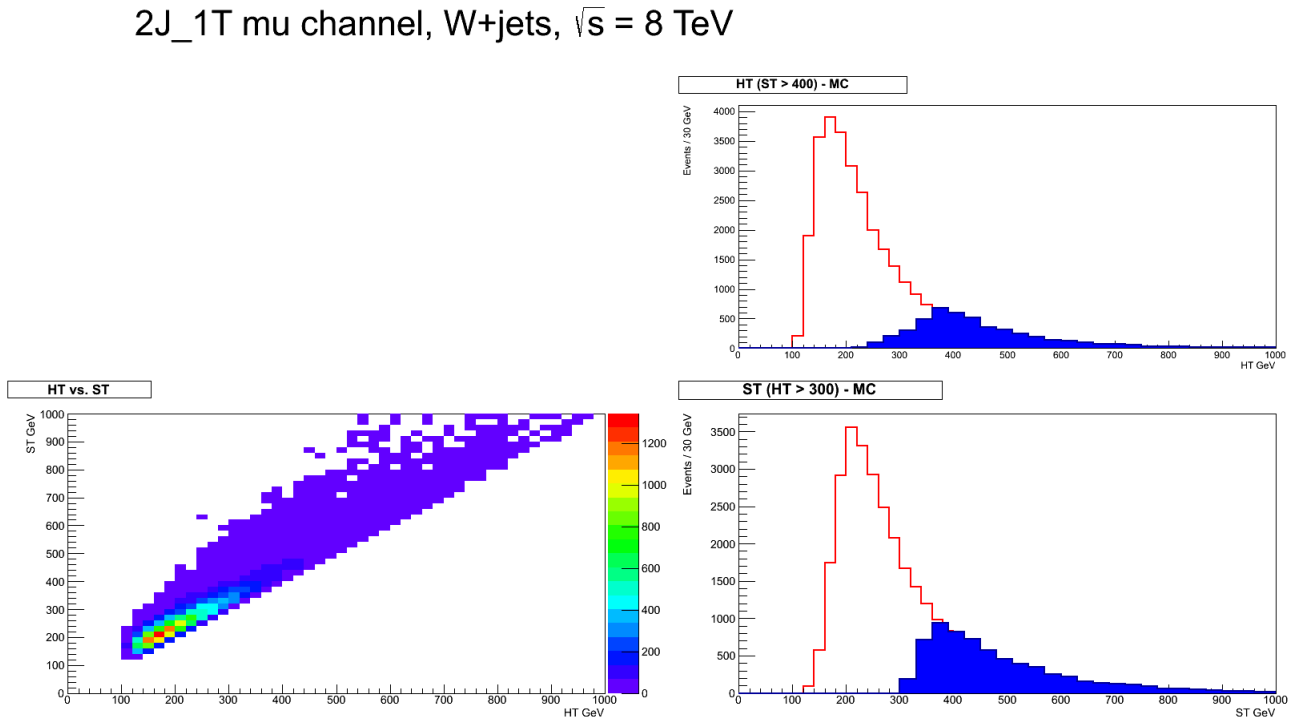

Figure 6.12: Study of the correlation of the transverse momenta scalar sum variables: WJets

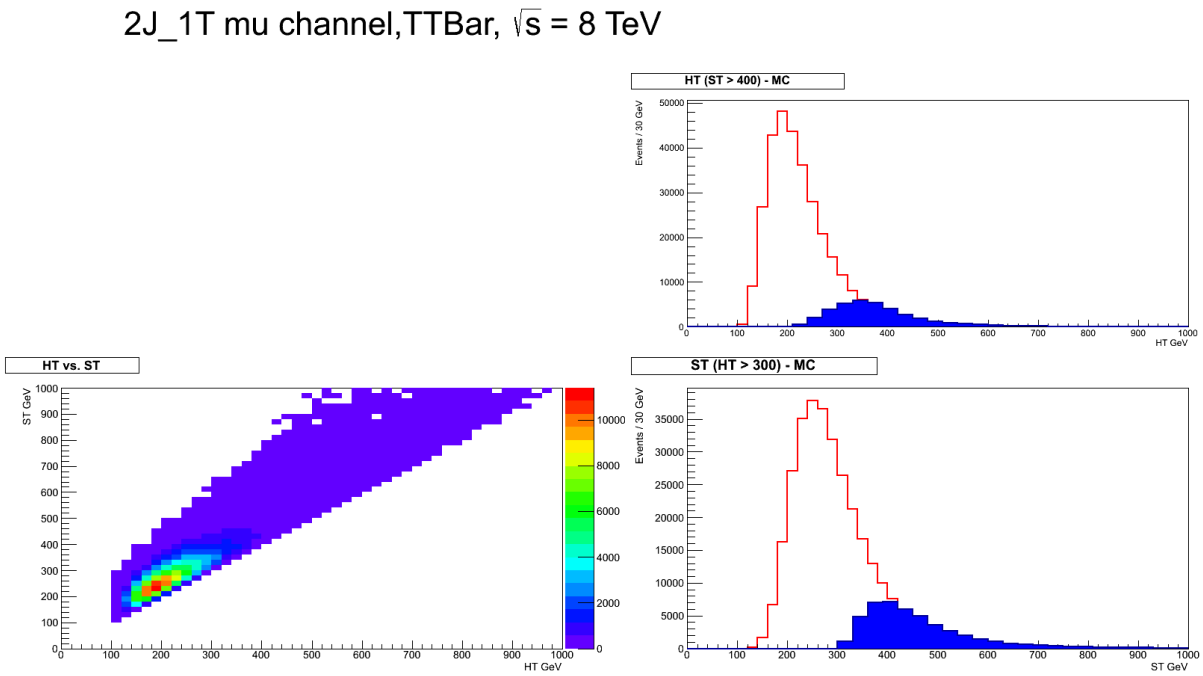

Figure 6.13: Study of the correlation of the transverse momenta scalar sum variables: TTbar

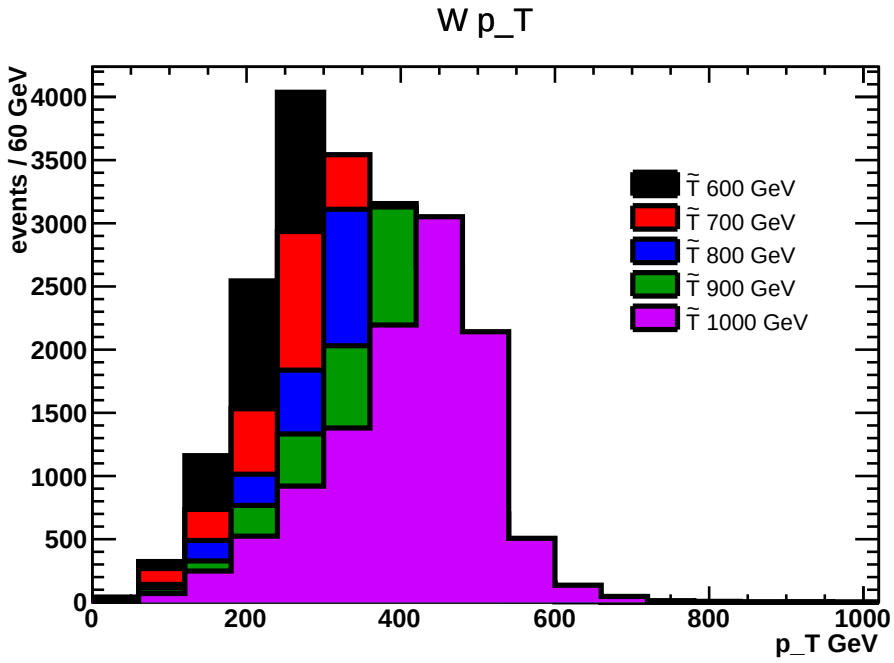

Figure 6.14: Transverse momentum p_T of the W boson

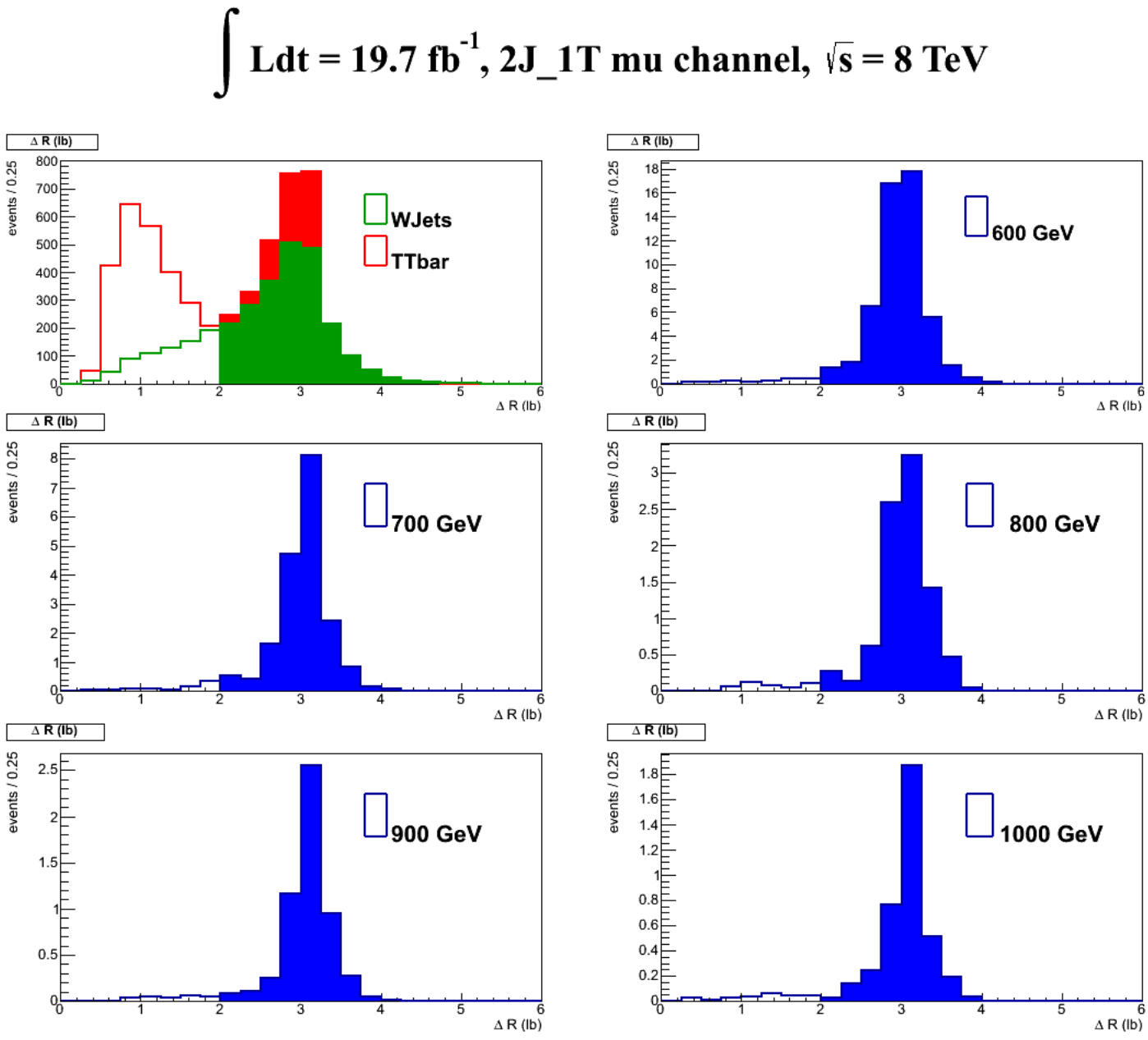

Figure 6.15: ΔR_{lb} ; $\Delta R_{lb} > 2.0$

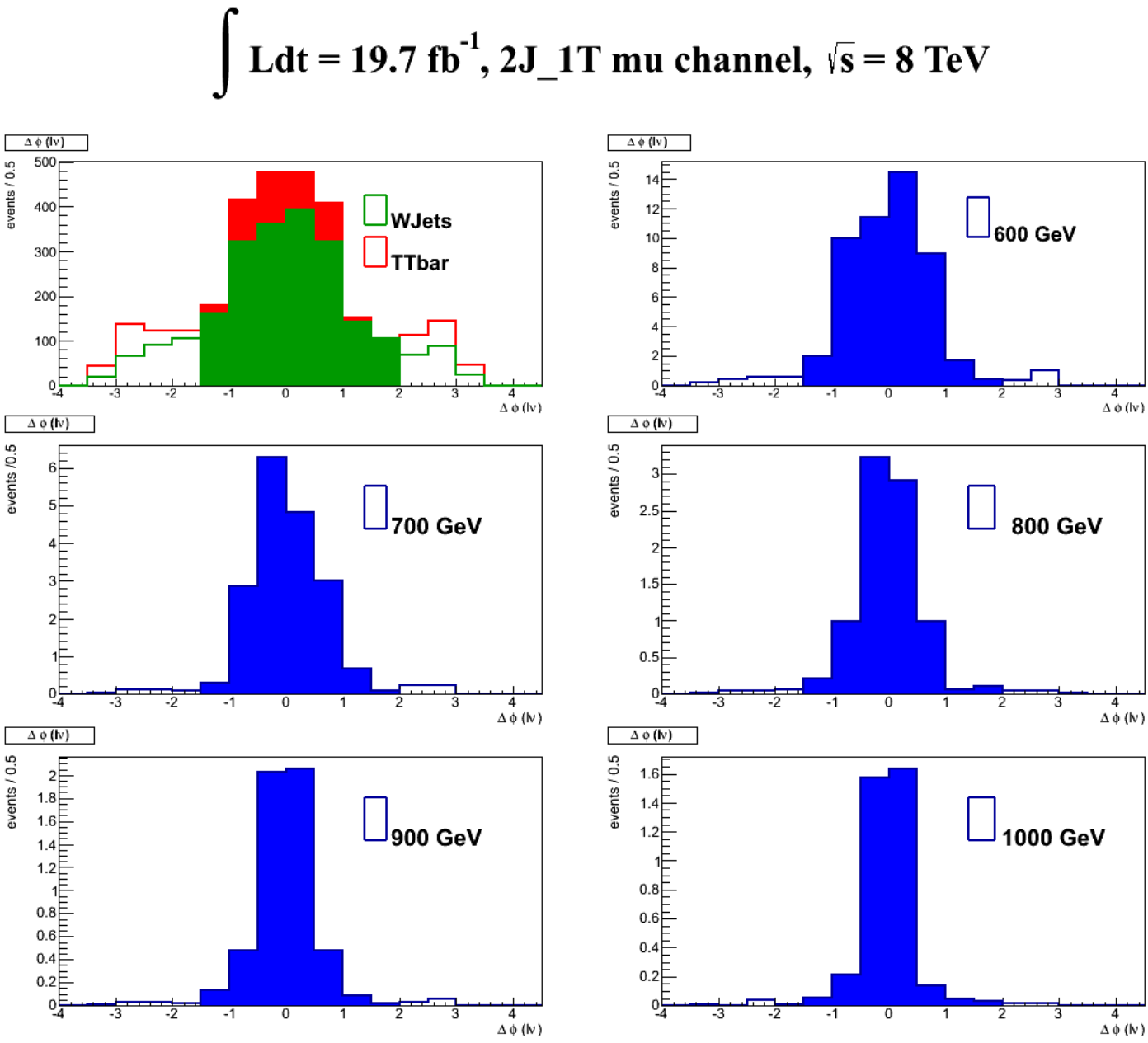

Figure 6.16: $\Delta\phi_{l\nu}$; $|\Delta\phi_{l\nu}| < 1.5$

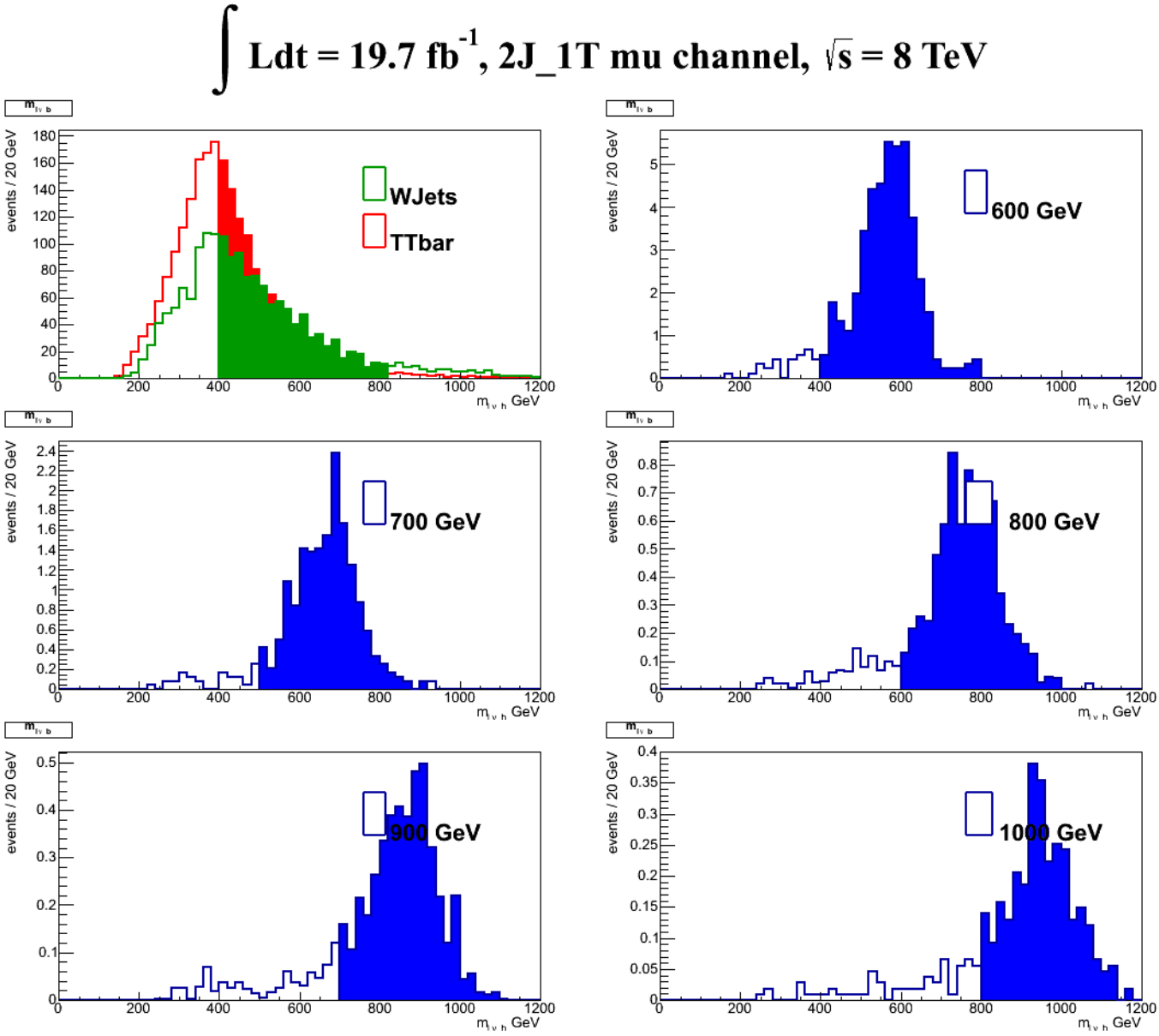

Figure 6.17: $m_{l\nu b}$;400 GeV window

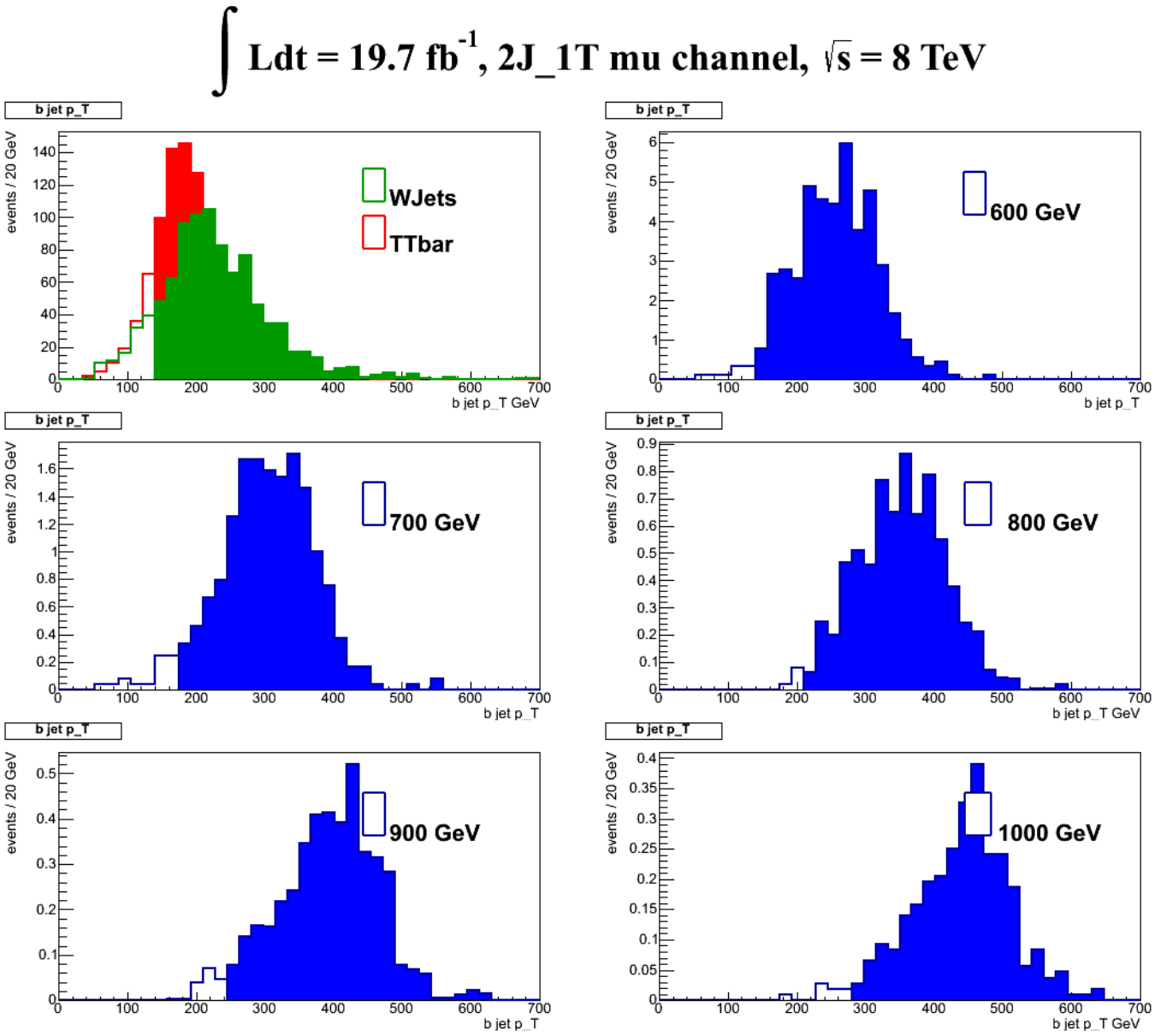

Figure 6.18: b-tagged jet p_T; cut values: 140-175-210-245-280 GeV

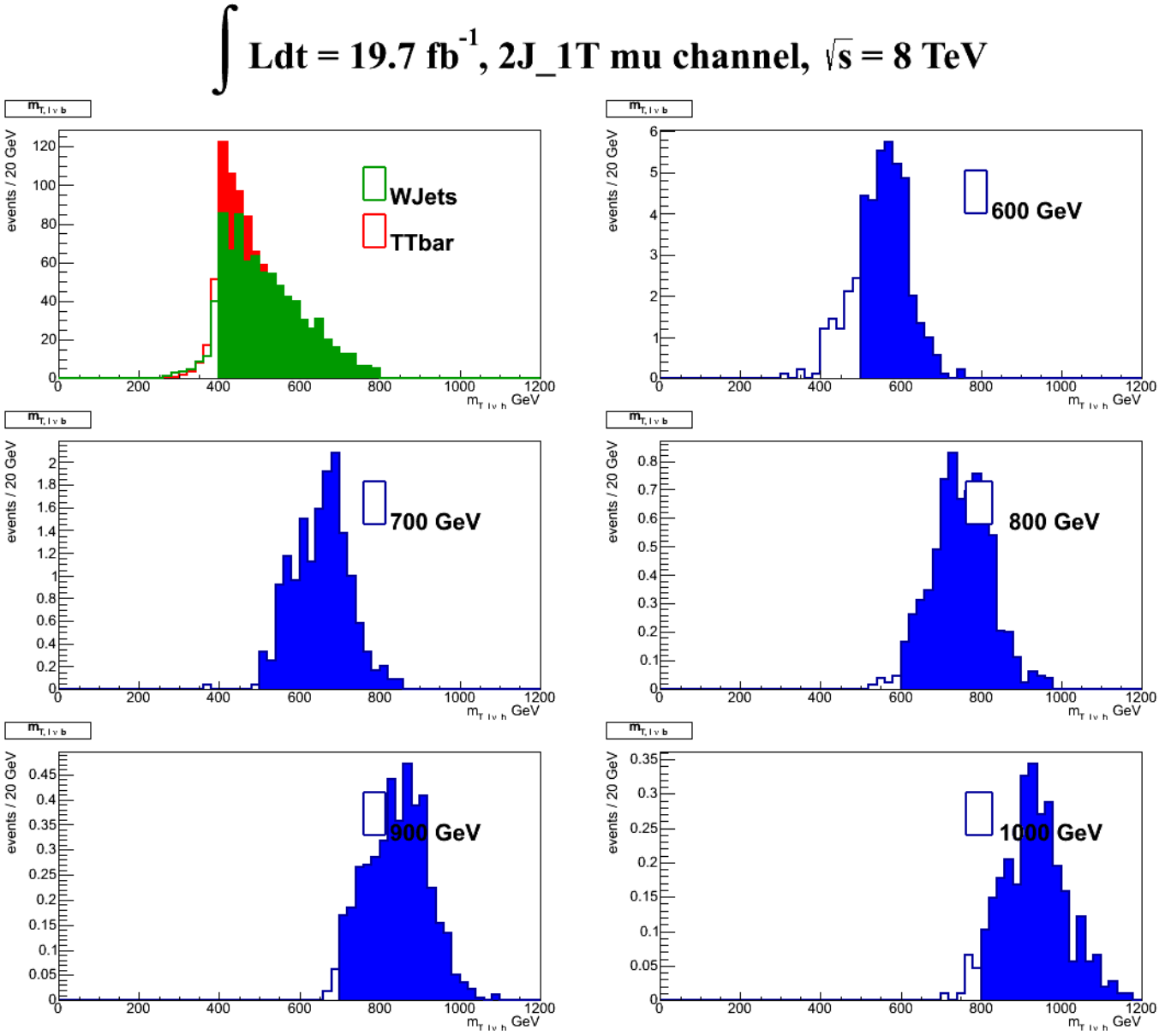

Figure 6.19: $m_{T,l\nu b}$; cut values: 400-500-600-700-800

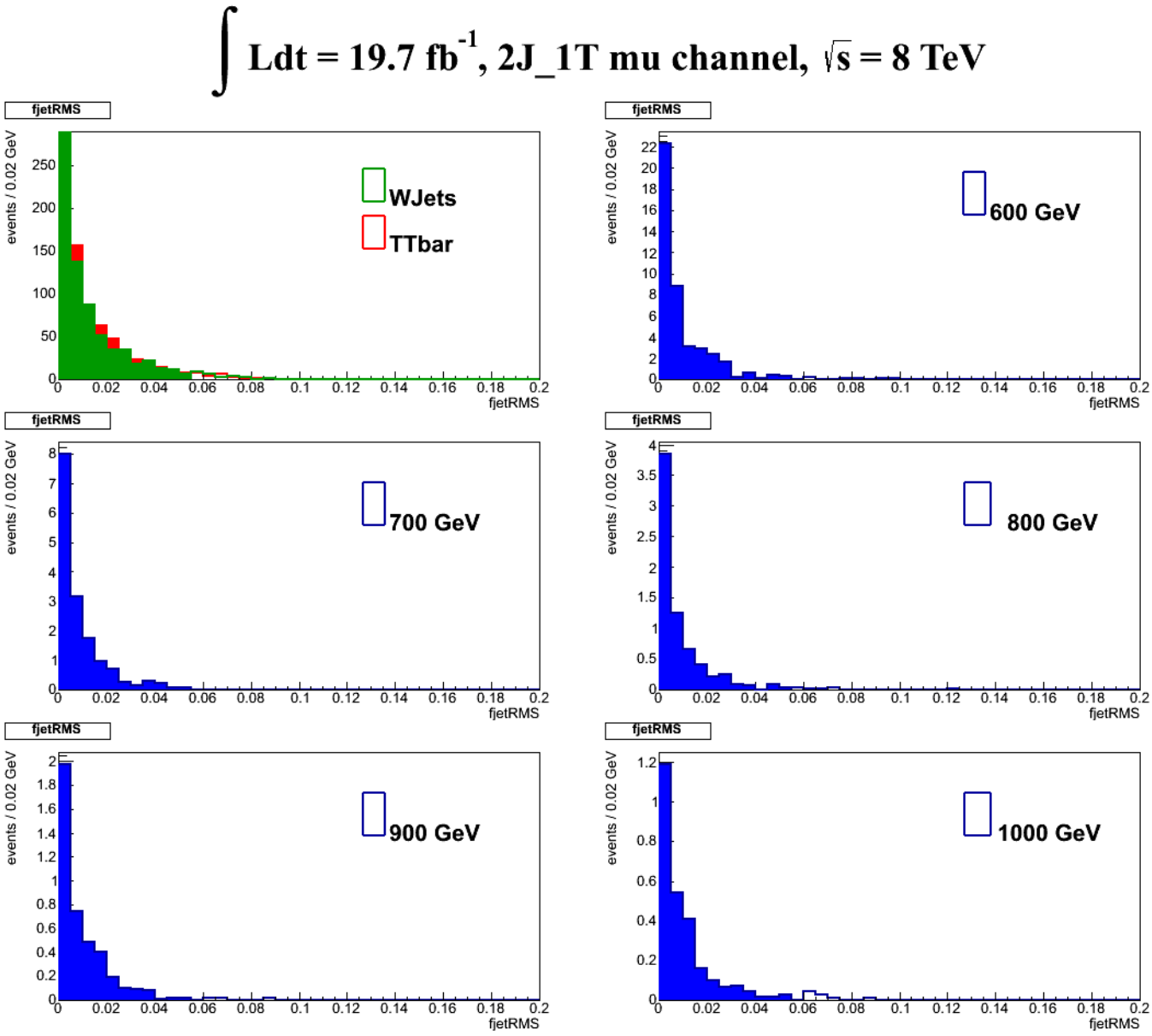

Figure 6.20: RMS of the jets ; fJetRMS&&bJetRMS < 0.05

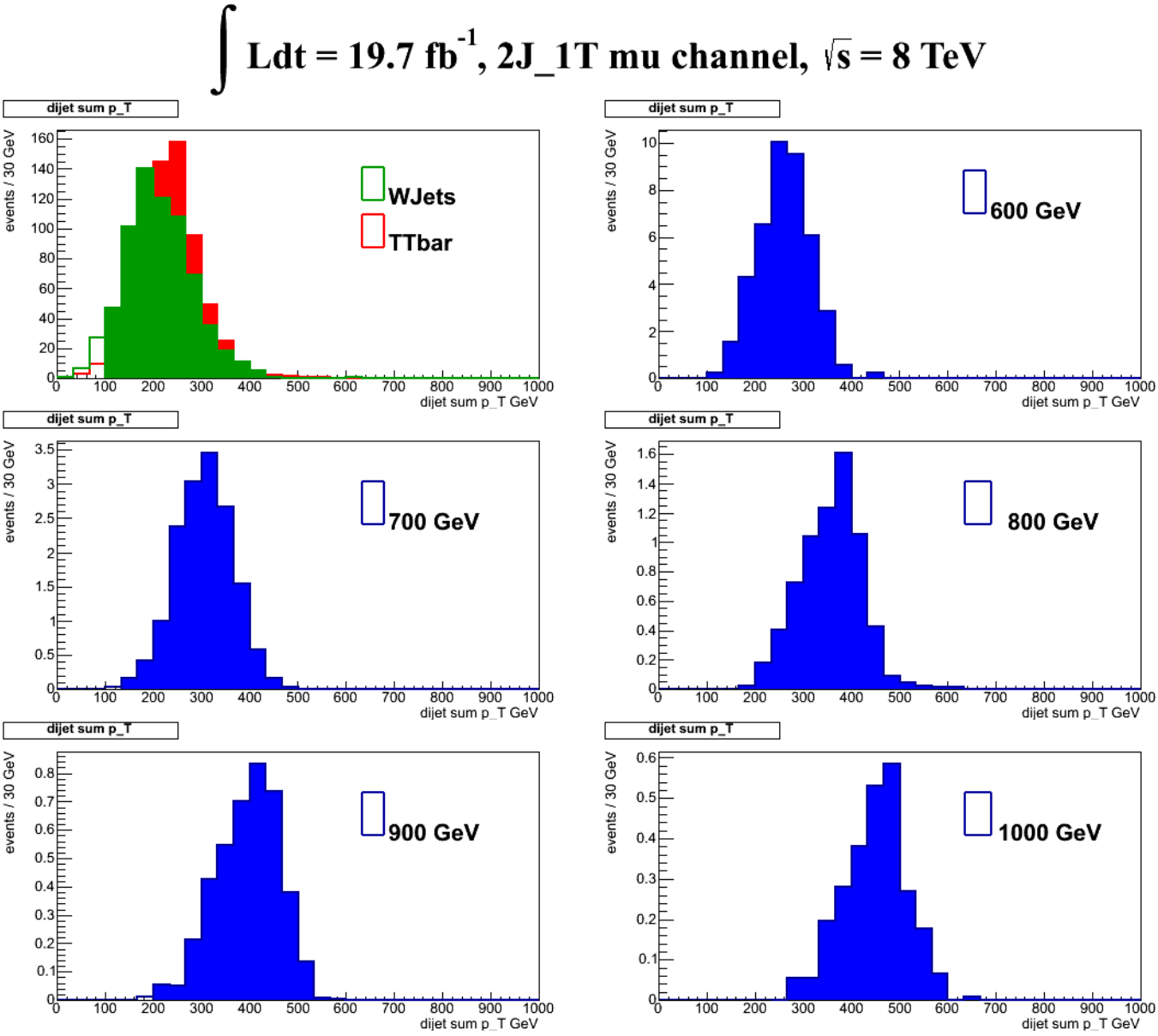

Figure 6.21: di-jet p_T vectorial sum; cut values: 120-150-180-210-240

sample	1	2	3	4	5	6	7	8	9	10	11
600 GeV	60	55	53	52	48	45	44	43	41	40	24
700 GeV	22	19	19	18	17	16	15	15	15	15	8
800 GeV	10	9	9	8	8	7	7	7	6	6	3
900 GeV	6	5	5	5	5	4	4	4	4	4	2
1000 GeV	4	4	4	3	3	2	2	2	2	2	1

Table 6.3: Muon channel , 2J_1T sample

600 GeV	44	40	39	38	36	34	33	33	33	32	18
700 GeV	18	15	15	15	14	12	11	11	11	11	6
800 GeV	9	8	7	7	6	6	5	5	5	5	3
900 GeV	5	4	4	4	4	3	3	3	3	3	2
1000 GeV	3	3	3	3	3	2	2	2	2	2	1

Table 6.4: Electron channel , 2J_1T sample

600 GeV	27	20	19	17	16	14	13	13	12	11	7
700 GeV	12	9	8	8	7	6	6	6	6	6	4
800 GeV	6	4	4	4	4	3	3	3	3	3	1
900 GeV	4	2	2	2	2	1	1	1	1	1	1
1000 GeV	2	1	1	1	1	1	1	1	1	1	0

Table 6.5: Muon channel , 3J_1T sample

600 GeV	35	27	25	23	22	20	18	18	18	17	10
700 GeV	13	9	9	8	7	6	6	6	5	5	3
800 GeV	6	4	4	4	4	3	3	3	3	3	1
900 GeV	4	3	3	3	2	2	2	2	2	2	1
1000 GeV	2	2	1	1	1	1	1	1	1	1	0

Table 6.6: Electron channel , 3J_1T sample

6.3 Selections, efficiencies and event yields

The next tables contain the number of events for every sample of signal (which differs in mass of the particle generated) and for WJets and TTbar background processes; the events are normalized to present luminosity: 19.7 fb^{-1}.

WJets_600 GeV	20160	4387	2983	2260	1698	946	836	764	691	566	98
WJets_700 GeV	20160	2790	2029	1516	1161	475	417	374	341	312	52
WJets_800 GeV	20160	1868	1406	1035	807	248	217	185	168	161	24
WJets_900 GeV	20160	1271	973	703	562	133	113	100	90	88	14
WJets_1000 GeV	20160	899	689	491	396	78	66	58	52	51	8

Table 6.7: Muon channel , 2J_1T sample

WJets_600 GeV	17112	4058	2774	2109	1551	844	757	692	629	490	67
WJets_700 GeV	17112	2626	1877	1406	1059	424	380	339	307	267	35
WJets_800 GeV	17112	1758	1289	962	733	241	216	190	173	157	18
WJets_900 GeV	17112	1196	909	670	513	136	118	102	96	92	13
WJets_1000 GeV	17112	833	643	467	367	76	66	54	50	49	4

Table 6.8: Electron channel , 2J_1T sample

WJets_600 GeV	8408	2394	1679	1301	983	556	473	437	402	327	71
WJets_700 GeV	8408	1546	1097	855	660	294	257	237	221	189	42
WJets_800 GeV	8408	1000	747	581	453	169	140	125	117	105	26
WJets_900 GeV	8408	683	519	403	322	96	77	65	61	59	17
WJets_1000 GeV	8408	463	373	282	229	51	44	36	32	31	9

Table 6.9: Muon channel , 3J_1T sample

WJets_600 GeV	9623	2723	1881	1432	1068	582	505	467	422	340	75
WJets_700 GeV	9623	1741	1266	979	745	323	286	254	230	209	44
WJets_800 GeV	9623	1144	852	658	513	163	144	127	114	107	24
WJets_900 GeV	9623	769	594	452	352	85	73	64	59	58	13
WJets_1000 GeV	9623	525	410	317	252	47	38	28	27	26	6

Table 6.10: Electron channel , 3J_1T sample

TTbar_600 GeV	57129	8283	5508	2935	2107	986	850	767	700	634	52
TTbar_700 GeV	57129	4157	2948	1475	1070	323	273	245	219	209	18
TTbar_800 GeV	57129	2231	1670	779	566	121	105	90	76	74	6
TTbar_900 GeV	57129	1302	1038	439	322	50	45	40	33	33	2
TTbar_1000 GeV	57129	806	666	256	192	24	22	19	16	16	1

Table 6.11: Muon channel , 2J_1T sample

TTbar_600 GeV	48515	7577	5097	2713	1963	926	799	717	649	583	54
TTbar_700 GeV	48515	3874	2770	1377	997	315	271	236	204	194	16
TTbar_800 GeV	48515	2124	1621	739	544	122	107	95	79	76	5
TTbar_900 GeV	48515	1253	998	416	310	59	52	45	36	36	1
TTbar_1000 GeV	48515	785	646	242	185	27	25	23	18	18	1

Table 6.12: Electron channel , 2J_1T sample

TTbar_600 GeV	56376	8755	5695	2946	2340	1083	912	830	757	652	94
TTbar_700 GeV	56376	4502	3114	1589	1288	396	330	293	261	242	34
TTbar_800 GeV	56376	2401	1749	879	715	160	137	122	105	102	14
TTbar_900 GeV	56376	1354	1024	501	417	67	62	52	43	42	6
TTbar_1000 GeV	56376	802	628	300	252	31	28	25	19	19	3

Table 6.13: Muon channel , 3J_1T sample

TTbar_600 GeV	65833	9392	6070	3132	2487	1141	965	872	807	696	104
TTbar_700 GeV	65833	4714	3224	1666	1340	414	346	310	283	264	40
TTbar_800 GeV	65833	2477	1778	910	735	163	139	122	108	105	17
TTbar_900 GeV	65833	1371	1028	518	424	72	62	54	45	44	6
TTbar_1000 GeV	65833	790	624	304	251	33	30	27	23	22	3

Table 6.14: Electron channel , 3J_1T sample

sample	efficiency (%)
600 GeV	6.45 ± 0.01
700 GeV	5.18 ± 0.01
800 GeV	4.27 ± 0.02
900 GeV	4.29 ± 0.02
1000 GeV	3.22 ± 0.02

Table 6.15: Efficiencies of the 2J-1T sample, muon channel

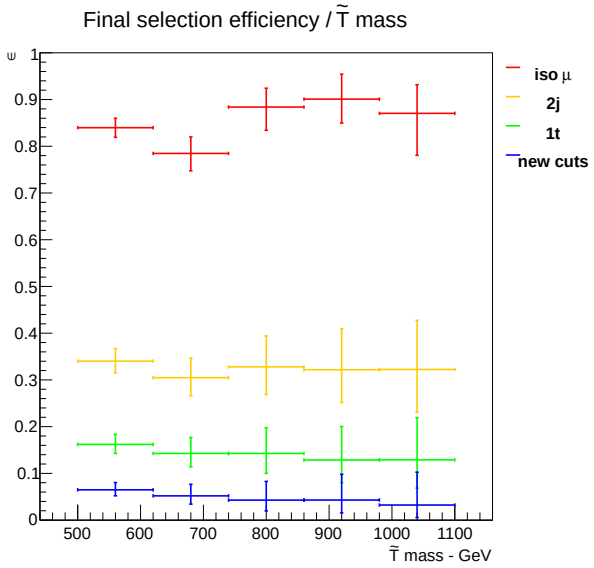

Figure 6.22: Sketch of the final efficiencies for the signal samples

6.3.1 Efficiencies

The efficiencies of the selections are given for every signal sample in the next table. A clear representation of the selections in the number of jets is shown in Tab. 6.15. We note that the muon channel and the electron one are almost equal, instead the two categories 2J-1T and 3J-1T are one half to the other (the latter is less efficient). In Fig. 6.23 we resum in a table the number of events in every sample, for the signal and for the backgrounds.

sample	events
600 GeV $\tilde{T}$	23
WJets	442
ZJets	27
Di-boson	11
TTBar	364
tW-channel	56
t-quark s-channel	7
t-quark t-channel	27
MC tot	938
Data	962
$S/\sqrt{S+B}$	0.74

sample	events
700 GeV $\tilde{T}$	9
WJets	186
ZJets	8
Di-boson	6
TTBar	126
tW-channel	24
t-quark s-channel	3
t-quark t-channel	11
MC tot	367
Data	377
$S/\sqrt{S+B}$	0.49

sample	events
800 GeV $\tilde{T}$	4
WJets	98
ZJets	1
Di-boson	3
TTBar	48
tW-channel	13
t-quark s-channel	1
t-quark t-channel	4
MC tot	171
Data	176
$S/\sqrt{S+B}$	0.32

sample	events
900 GeV $\tilde{T}$	2
WJets	50
ZJets	1
Di-boson	2
TTBar	22
tW-channel	6
t-quark s-channel	0
t-quark t-channel	1
MC tot	85
Data	88
$S/\sqrt{S+B}$	0.27

sample	events
1000 GeV $\tilde{T}$	1
WJets	23
ZJets	1
Di-boson	1
TTBar	9
tW-channel	3
t-quark s-channel	0
t-quark t-channel	0
MC tot	41
Data	42
$S/\sqrt{S+B}$	0.21

Table 6.16: 2J-1T sample, μ channel final event yields

600 GeV $\tilde{T}$	23
MC total	938
Data	962
$S/\sqrt{S+B}$	0.74

(a)

700 GeV $\tilde{T}$	9
MC total	367
Data	377
$S/\sqrt{S+B}$	0.49

800 GeV $\tilde{T}$	4
MC total	171
Data	176
$S/\sqrt{S+B}$	0.32

900 GeV $\tilde{T}$	2
MC total	85
Data	88
$S/\sqrt{S+B}$	0.27

1000 GeV $\tilde{T}$	1
MC total	41
Data	42
$S/\sqrt{S+B}$	0.21

Table 6.17: 2J-1T e channel

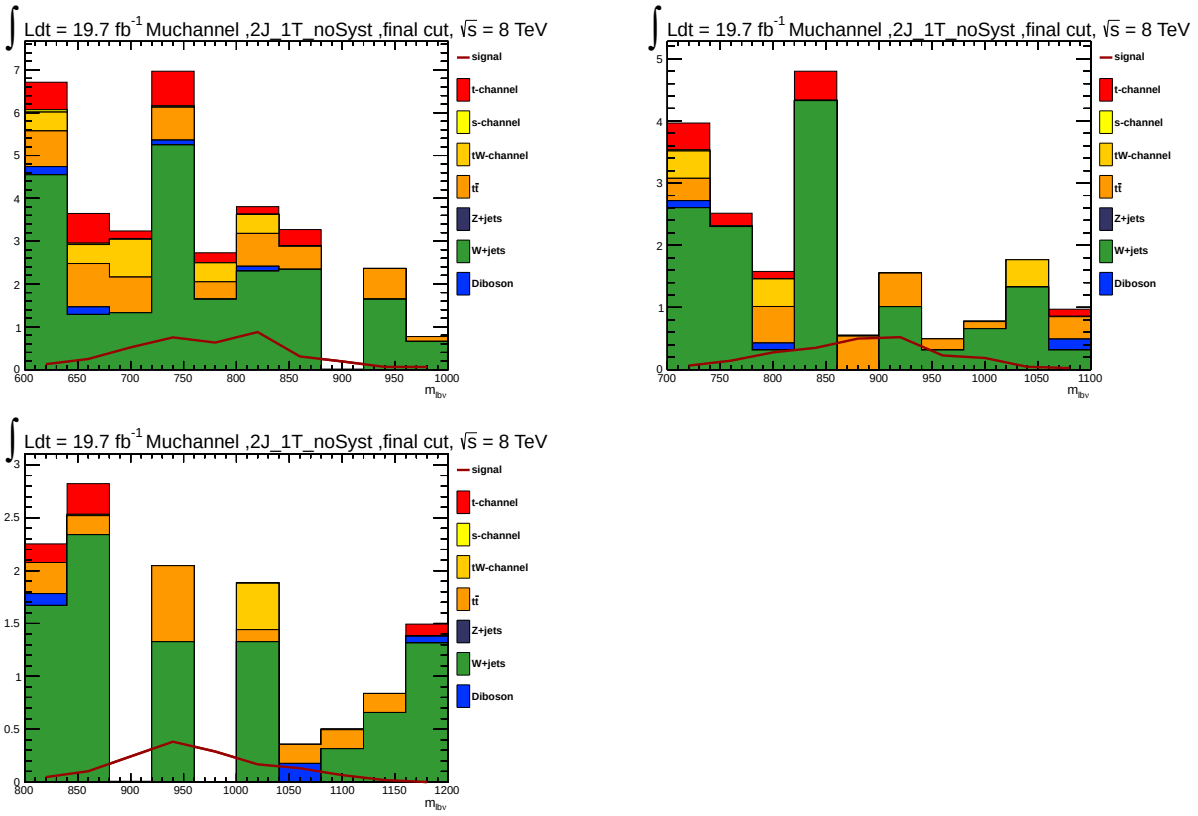

Figure 6.23: Stack of the top partner reconstructed mass with the final set of kinematical cut

6.4 On the reconstruction of the top partner invariant mass

As we saw in the previous chapters, during our work we found that the reconstruction of the top partner mass didn't work very well as it was for the single top quark production process. The peak is not very sharp at all (at half maximum it has a width of about 150-200 GeV), and it is not centered at the right value, but some points lower. There is a strange shoulder at about 200-300 GeV, that is something we do not expect, that could have its origin in the recombination of the reconstructed objects (we may not match the right particle in the reconstruction). First, we noted which were the differences between the Standard Model single top production and the process we generated. As we said, these were the hardness of the process, in particular, for what concern the top partner mass, we were interested in the three objects from the decay. So, as we noted previously, the W in the decay is boosted: lepton and neutrino have almost the same energy and direction. This is confirmed by a plot of the cosinus of the difference of the azimuthal angle between the two objects: It is interesting to note in this figure how the angle reduces with the increasing mass of the top partner (and subsequently the enhancement of the boost of the W gauge boson produced). Initially we thougth that the reason of the wrong reconstruction was to impute to the badness of the algorithm we used. As we have shown there is an uncertainty in the longitudinal momentum of the neutrino. The algorithm studied in [**?**] takes as the z-component of the momentum of the neutrino the smallest; the motivation, as we read in that work, is dictated by reasons concerning the trigger. Then we tried to change algorithm, because at first look, we thoguth the right choice was in the biggest longitudinal component. First, we tried to recover at parton level the same algorithm. Then, as we noted, that neutrino and lepton are collinear and have almost the same

600 GeV $\tilde{T}$	10
MC total	719
Data	730
$S/\sqrt{S+B}$	0.38

700 GeV $\tilde{T}$	3
MC total	320
Data	324
$S/\sqrt{S+B}$	0.21

800 GeV $\tilde{T}$	1
MC total	123
Data	125
$S/\sqrt{S+B}$	0.17

900 GeV $\tilde{T}$	1
MC total	61
Data	63
$S/\sqrt{S+B}$	0.15

1000 GeV $\tilde{T}$	0
MC total	32
Data	32
$S/\sqrt{S+B}$	0.11

Table 6.18: 3J-1T μ channel

600 GeV $\tilde{T}$	10
MC total	719
Data	730
$S/\sqrt{S+B}$	0.38

700 GeV $\tilde{T}$	3
MC total	320
Data	324
$S/\sqrt{S+B}$	0.21

800 GeV $\tilde{T}$	1
MC total	123
Data	125
$S/\sqrt{S+B}$	0.17

900 GeV $\tilde{T}$	1
MC total	61
Data	63
$S/\sqrt{S+B}$	0.15

1000 GeV $\tilde{T}$	0
MC total	32
Data	32
$S/\sqrt{S+B}$	0.11

Table 6.19: 3J-1T e channel final yelds

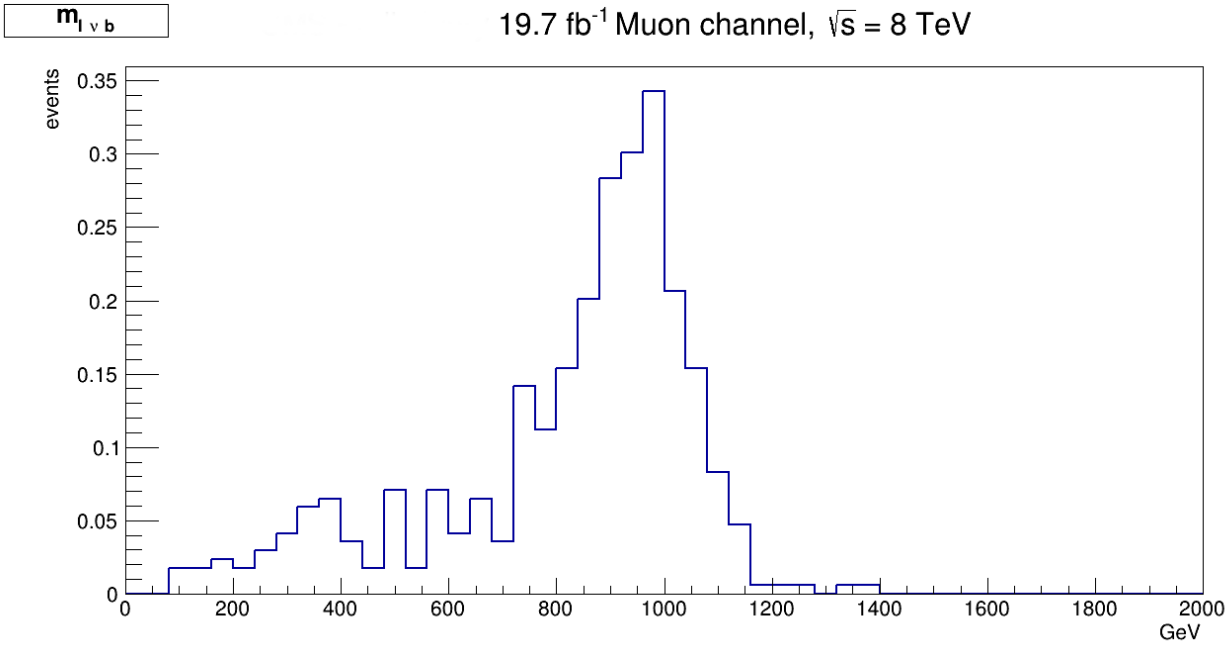

Figure 6.24: Top partner reconstructed mass, $m_{l\nu b}$

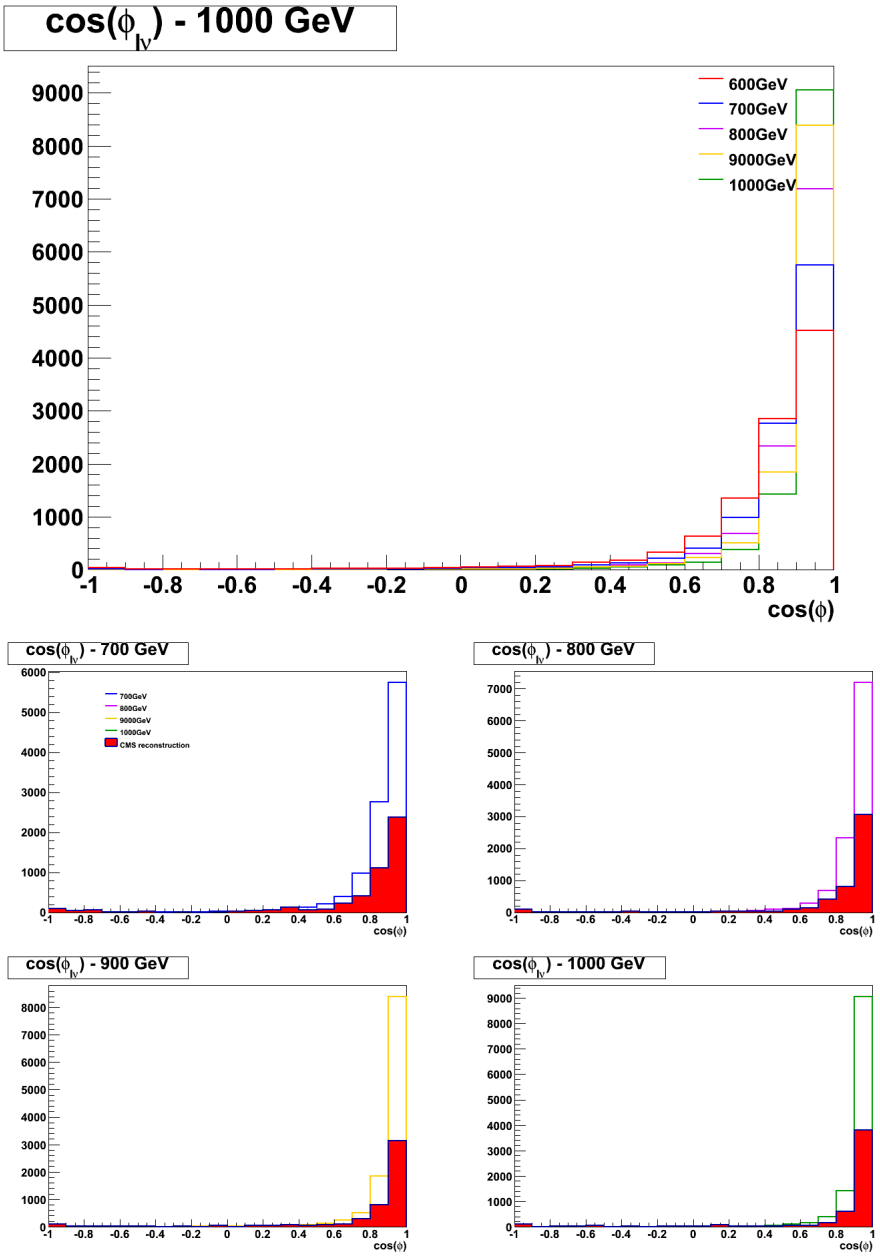

Figure 6.25: Cosinus of the difference of the azimuthal angle between lepton and candidate neutrino

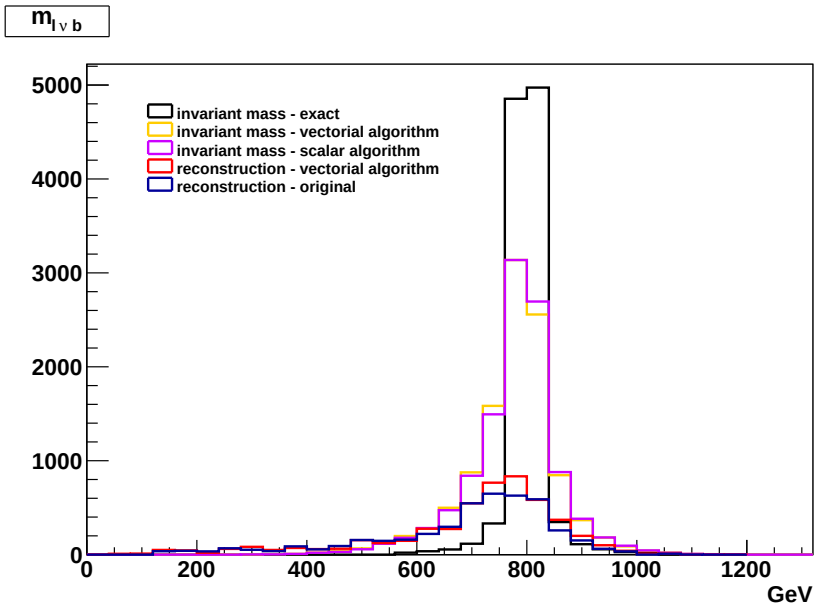

Figure 6.26: Various reconstruction of $\tilde{T}$ mass (800GeV): with original we mean the algorithm used during all the thesis

energy, we reconstruct the mass in the following ways:

$$p_{\nu,z} = \frac{|E_T|}{|p_T^l|} p_{l,z} + o\left(\alpha^2\right) \ , \tag{6.9}$$

this is the *scalar* version of the hypothesis, instead the following is what we call the *vectorial*:

$$\mathbf{p}_\nu = \frac{|E_T|}{|p_T^l|} \mathbf{p}_l + o\left(\alpha^2\right) \tag{6.10}$$

The reason for trying also a vectorial version of the scalar algorithm, substituting all the candidate neutrino with the momentum of the lepton is due to an uncertainty on the whole reconstruction of the neutrino. In the following figure there is the comparison between all the algorithms we tried. The last two figure show the evolution of the reconstruction with the longitudinal momentum of the neutrino with the highest value. As we can see, it is not a problem of the algorithm of reconstruction. It is evidently a problem of physical object reconstruction, as we can see in the comparison in 6.25: the loss of events we have during the simulation with CMSSW is almost in process with lepton and neutrino collinear (that are the events we are interested in!). As we have seen when the efficiencies were computed, more than an half events do not compare in the sample 2J_ 1T because of the b-tagging algorithm, that has a bad efficiency itself. Perhaps the request of such a type of catalogue, divided into a fixed number of jets and b-tagged jets, is not a good one; it would be more interesting to get from a source with events with N number of jets and at least one b-tagged jet. For this purpose we would need a more exact classification of the forward jet: in the single top analysis package the forward jet is classified as the jet with lower b-tag discriminator. Althoguh this could be a good approximation, perhaps a classification based on the pseudo-rapidity (and other request, like in the root mean square of the E_T weighted calorimeter towers' ϕ) would be a better solution. We can see in the following figures, Figs. 6.28, 6.29 and 6.30, the discrepances in the reconstruction of the forward jet, from generator level, to the FASTSIM with the effect of the detector included.

To right understand these figures, we have to note the two histograms superimposed compare two different steps in the analysis, the parton level generation and the CMSSW reconstruction *after*

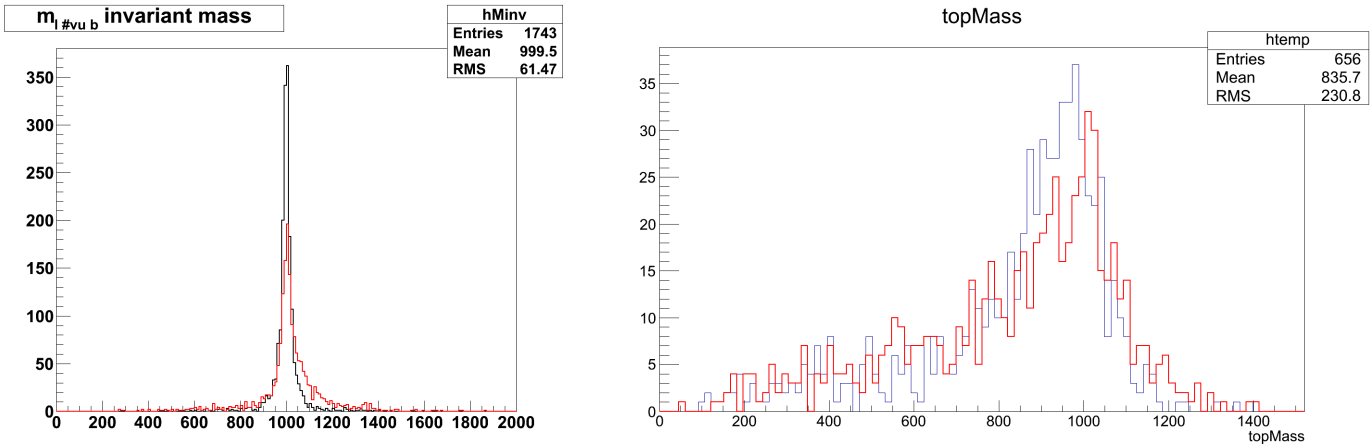

Figure 6.27: Reconstruction of the $\tilde{T}$ mass with the highest longitudinal momentum: comparison at parton level and after CMSSW simulation. The dark line is the original algorithm, with the smallest p_z chosen; the red line is the algorithm with the highest p_z chosen.

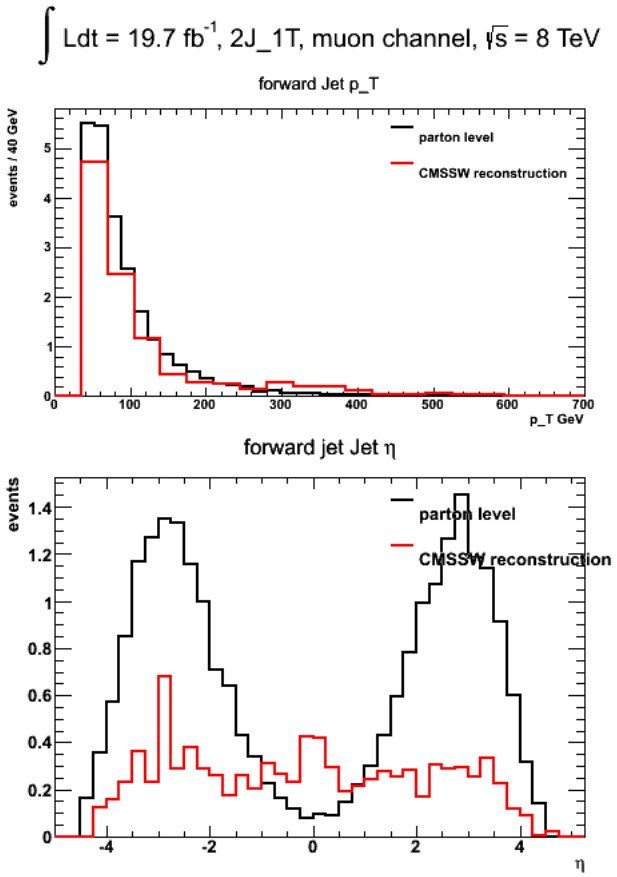

Figure 6.28: MadGraph and CMS reconstructed forward jet p_T and psuedo-rapidity $\eta_{j'}$

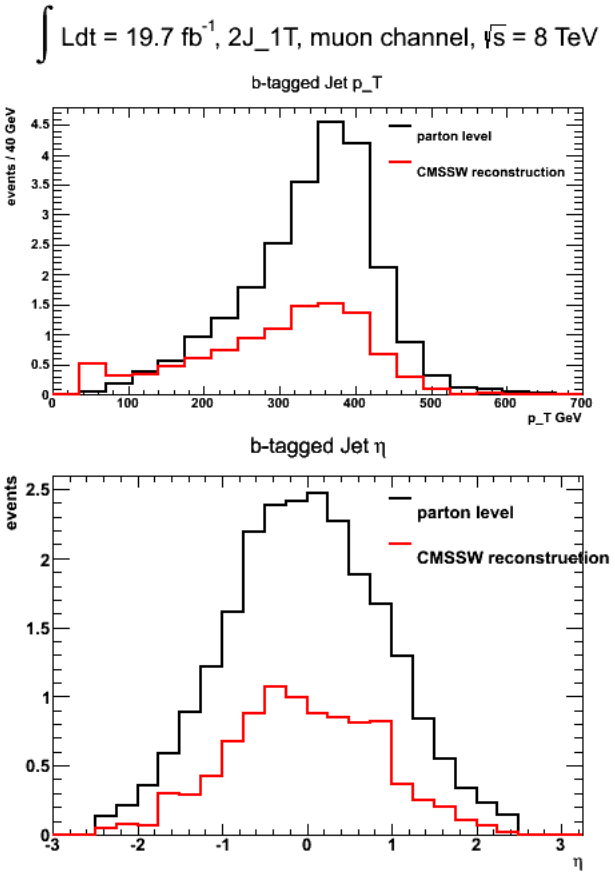

Figure 6.29: MadGraph and CMS reconstructed b-tagged jet p_T and psuedo-rapidity $\eta_{j'}$

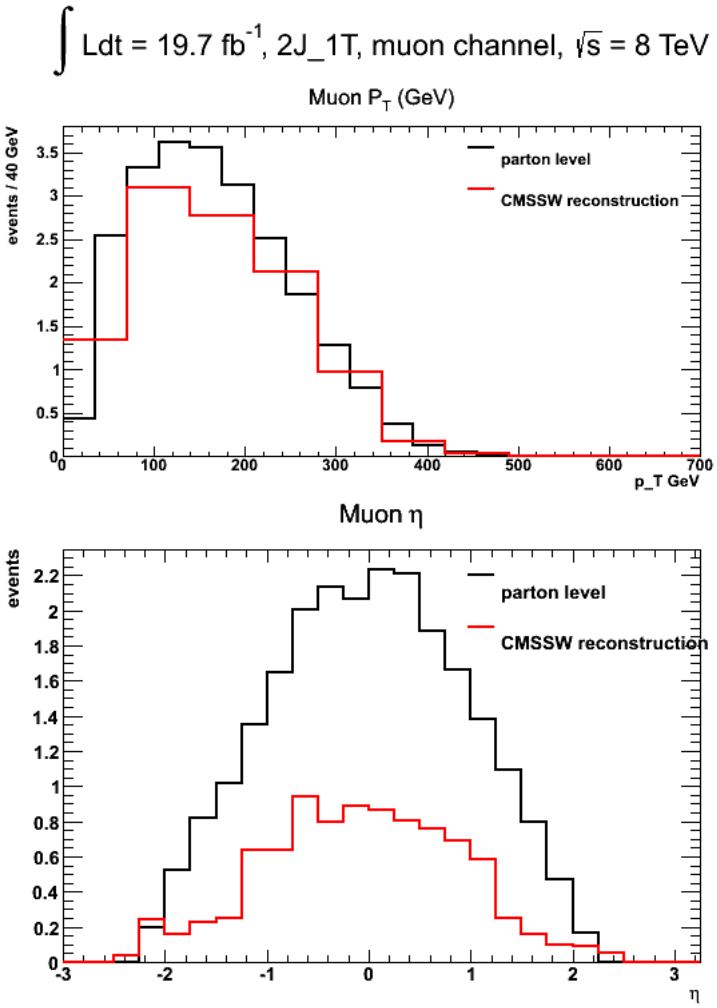

Figure 6.30: MadGraph and CMS reconstructed muon p_T and psuedo-rapidity $\eta_{j'}$

the selection in the number of light and b-tagged jets, then we can see the loss of events - comparing them with the efficiencies computed above. There are two features of these distributions we have to emphasize, the badly reconstructed pseudorapidity of the forward jet and the transverse momentum of the b-jet. The first is not peaked at high values, then it is not a very good discriminant (even if after all it has a good power on the backgrounds). The latter instead has something like a peak at low values (those are events that exceed the amount we expect from parton level distribution). So there are surely some issues on the reconstruction and right selection of the jets. If we regard Fig. 6.3 we can state that the exact selection of two jets in the event roughly cut the jets forward. The forward jet itself has central values of the peak we do not expect.

Chapter 7

Interpretation of results and comments

7.1 Bounds on the production of $\tilde{T}$

Since we do not observe any excess that could be ascribed to the production of a new Top Partner object, we proceed in estimating the bounds on its production cross section. The Bayesian and the classical frequentist, with a number of modifications, are two statistical approaches commonly used in high energy physics, and in particular at LHC [51], for characterising the absence of a signal. We obtain these results through a dedicated *Python* written software, [52] for a reference. Placing an upper limit means: the largest value of the signal s for which the probability of a signal under-fluctuation equal to what has been observed or less is more than a given level α (usually 10% or 5%). An upper limit with a given Confidence Level means that we observe a maximum of the signal s such that $p \geq \alpha = 1 - CL$, where p is the probability (*p-value*) to found an excess grand equal to the background only hypohesis yield. Both methods allow one to quantify the level of incompatibility of data with a signal hypothesis, which is expressed as a confdence level. It is common to require a 95 %C.L. for "excluding" a signal, this is however a convention. The top-partner single production process is said to be excluded at, say, 95% C.L., when the 95% C.L. limit on μ_{signal} drops to one, i.e. $\mu_{95\%\,CL} = 1$. In the next sub-sections, we will follow this convention and discuss limits on the common *signal strength modifier* μ_{signal}. In the following, the signal events of $\tilde{T}$ production are denoted by s, instead the event yields from Standard Model background are written as b. The distribution we consider is binned; every bin i follow a Poisson distribution, around the expected Poisson mean λ_i. This expected yield is given by the sum over all considered backgrounds and signal.

$$\lambda_i = \mu_{signal} \cdot s_i + \sum_p b_{p,i} \tag{7.1}$$

The variable μ_{signal} expresses the normalization constant that should be applied to the signal to have an exclusion limit on the production of our particle, at 95% confidence level. The Poisson probability to observe n_i events, where i runs over the number of bins of the distribution, is:

$$\Pi_i \frac{(\mu_{signal} s + b)^{n_i}}{n_i} e^{-(\mu_{signal} s + b)} \tag{7.2}$$

Generally, for each independent source of systematic uncertainty, a nuisance parameter is introduced. A background normalization uncertainty is modeled with a coefficient for the template B_p with a log-normal prior. A shape uncertainty is modeled by choosing a Gaussian prior for the nuisance parameter and using this parameter to interpolate between the nominal template (which is not affected by the uncertainty) and the shifted templates which are obtained by applying plus/minus

1sigma systematic shifts to the simulated samples and re-deriving the templates. This interpolation uses a smooth function which is cubic in the range up to 1 σ and a linear extrapolation beyond 1 σ.

7.1.1 Bayesian approach

The Bayes theorem is invoked to assign a probability to the signal hypothesis by calculating the posterior "probability density function" $L(\mu)$:

$$L(\mu) = \frac{1}{C}\int_{\theta} p(data|\mu_{signal}s + b)\rho_{\theta}(\theta)\pi_{\mu_{signal}(\mu_{signal}}d\theta \tag{7.3}$$

The functions $\rho_{theta}(\theta)$ describes our prior belief in the scale and description of the uncertainties on signal and backgrounds event yields. $\pi_{\mu_{signal}}(\mu_{signal})$ is the prior probability on the signal strength, which is commonly take to be flat for $\mu_{signal} \geq 0$ and zero elsewhere. C is set to normalise the probability density function to unit area. The Bayesian one-sided 95% CL is defined as:

$$\int_{0}^{\mu_{95\%\,CL}} L(\mu_{signal})d\mu_{signal} = 0.95 \tag{7.4}$$

- Bayesian methods construct the posterior given by the likelihood function times the prior and make statistical inferences from this posterior. This involves integrating out the nuisance parameters which is done in theta using a Markov Chain Monte-Carlo method.
- Calculate Quantiles of the marginal posterior of μ_{signal}. This can be used to derive quantile-based Bayesian confidence intervals (where upper limits are just a special case).

The Bayesian methodology is a likelihood principle since the inference is based on the data alone. It is critized to be a subjective method, mainly due to the freedom of decision in the choice of the prior distribution.

7.1.2 CL_s approach

We have to define a test statistic q_μ designed to discriminate signal-like events from background-like ones. The test statistic compresses all signal-backgrounds discriminating information into a unique parameter. Using the Neyman-Pearson lemma (citazione), the ratio of the two likelihood Q is the most powerful discriminator. It's better to use a log version:

$$q_\mu = -2ln\left(\frac{\mathcal{L}(data|\mu_{signal}s + b)}{\mathcal{L}(data|\hat{\mu_{signal}}s + b)}\right) \tag{7.5}$$

with $0 \leq \hat{\mu_{signal}} \leq \mu_{signal}$ and where $\mathcal{L}(data|rate)$ is a product of Poisson probabilities, for the number of *observed* or *simulated* (that make the difference between observed and expected limit). Events with $q_\mu \geq 0$ appear to be under the background only hypothesis, viceversa for the background-plus-signal hypothesis.

θ is a conditional maximum likelihood estimator; it gives a constraint on the extimation of the likelihood maximum, and it reproduces the systematics uncertainties in data. Generating Markov-Chain Monte Carlo pseudo-data for the two hypothesis allows one to construct the Probability Density Function $f(q_{\mu|\mu_{signal},\theta})$ and $f(q_{\mu|0,\theta})$. The nuisance parameters for the two different hypothesis are set by the maximization described above. Having defined this two distributions we can build the two confidence level interval:

$$p_{\mu_{signal}} = P(q_\mu \geq q - \mu^{obs.}|s + b) = \int_{q_\mu^{pbs.}}^{\infty} f(q_\mu|\mu_{signal}, \theta^{obs.}_{\mu_{signal}})dq_\mu \tag{7.6}$$

$$1 - p_b = P(q_\mu \geq q - \mu^{obs.}|b - only) = \int_{q_0^{pbs.}}^{\infty} f(q_\mu|0, \theta_0^{obs.})dq_\mu \tag{7.7}$$

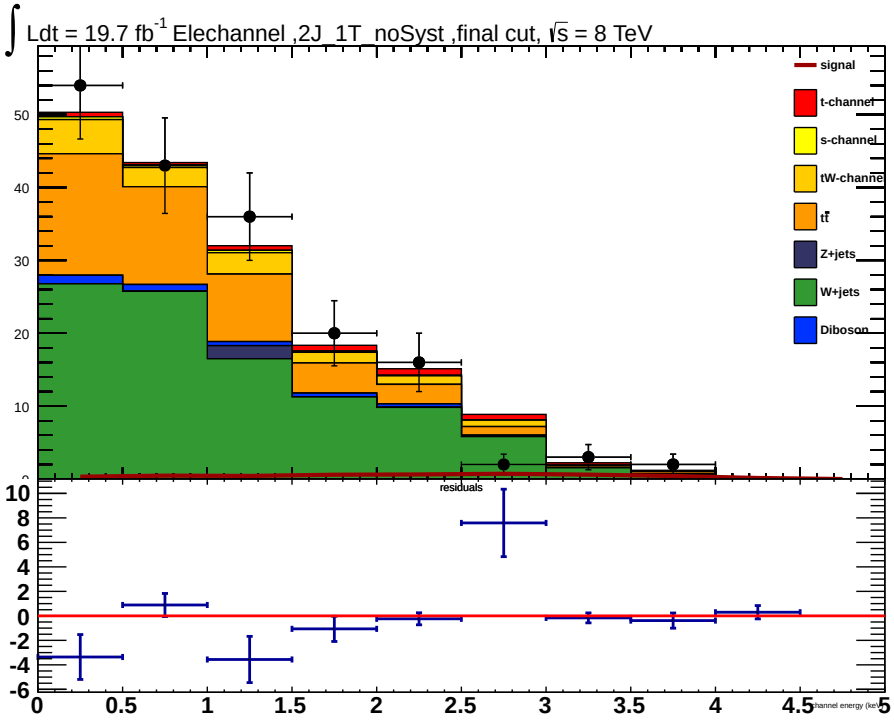

Figure 7.1: Forward jet pseudorapidity $\eta_{j'}$

The CL_s is defined as:

$$CL_s(\mu_{signal}) = \frac{p_{\mu_{signal}}}{1 - p_b} \tag{7.8}$$

To reach the desired 95% Confidence Level, we adjust μ_{signal} until we reach $CL_s = 0.05$. The calculation of the expected limit and its correlated fluctuations is slightly different. The expected median upper-limit and its ± 1, 2σ is a bound on the background only hypothesis. Generating a large set of background only pseudo-data, we calculate the $\mu_{signal}^{95\%CL_s}$ for each of them, as if they were real data. Then, one can build a cumulative probability distribution of results by starting integration from the side corresponding to low event yields. The point at which the cumulative probability distribution crosses the quantile of 50% is the median expected value. The $\pm 1\sigma$ (68%) band is defined by the crossings of the 16% and 84% quantiles. Crossings at 2.5% and 97.5% define the $\pm 2\sigma$ (95%) band.

7.1.3 Results

To place a bound for the production of $\tilde{T}$, we use a modified frequentist method, known as CL_s, and a Bayesian approach too, implemented in the *theta* software [52]. The signal is, of course, scaled to the cross section (per luminosity - and a data-driven scale factor). The backgrounds yields are scaled to the cross section and luminosity of the analyzed datasets. The presence of systematics uncertainties affect the value of λ_i. Systematics uncertaintes have not been directly computed for this new selection. We then apply an overall factorization of systematics uncertainties adding a log-normal distribution equal to the 10 % of the total event yields of background, [46]. In figure 7.2 a plot of the 95%CL_s with the Monte Carlo generated during our work.

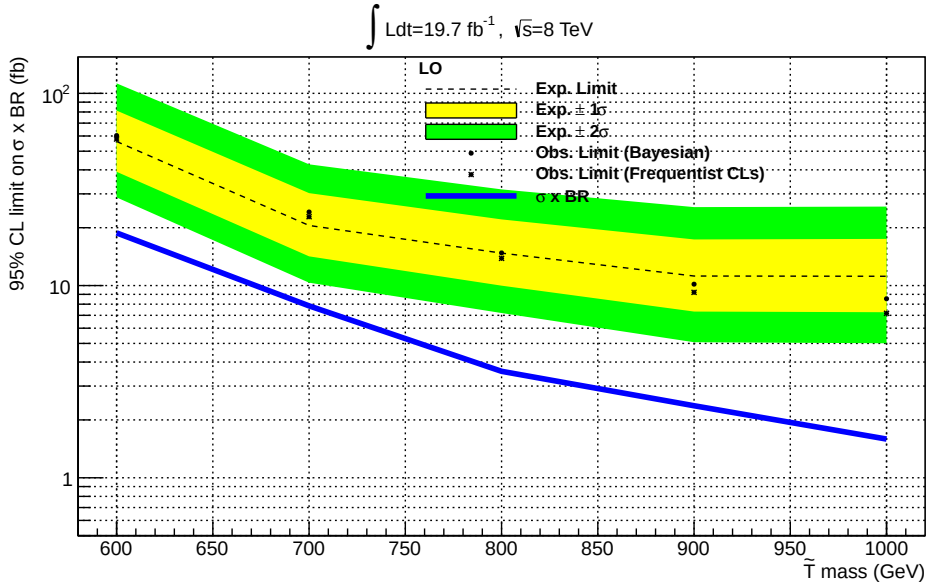

Figure 7.2: 95% CL_s on $\sigma \times Br(Wb)$ of $\tilde{T}$ single production at Large Hadron Collider, $\sqrt{s} = 8\,TeV$ and $\int \mathcal{L}dt = 19.7 fb^{-1}$

7.1.4 Theoretical interpretation of the results

The theoretical band discussed in 3 is superimposed to this plot: it is a straighforwad procedure having used such methods for placing a bound (that is on μ_{signal} - a normalization to the cross-section rate). The only free coupling c_2 is tuned to obtain this scenario: given the mass of the top-partner and setting the mass of the top-quark to its Particle Data Group value, there is an unique relation linking y to c_2. Modifying one of these, we are going to enhance or reduce the chiral rotation angle θ_L. We remind that:

$$g_{\tilde{T}b} = \frac{\sqrt{2}}{2} g_{EW} sin\left(\theta_L(y, c_2, M_\Psi)\right) \tag{7.9}$$

For our model the particular dependence between c_2 and $sin(\theta_L)$ is inverse: $sin(\theta_L) \propto 1/c_2$. Fig. 7.3 is the exclusion plot with $c_2 \in [1/3, 1]$. In Fig. 7.4 we have plot the distribution of the c_2 parameter, that as we described in Chapter 3, completely controls the coupling for the $\tilde{T}$ production, as a function of the mass. The grey band shows the 95% CLs region excluded with the present analysis. We can see that, as we expected from the results, we have stronger bounds for low masses, since the efficiency in the reconstruction is slightly worse for high mass scenario.

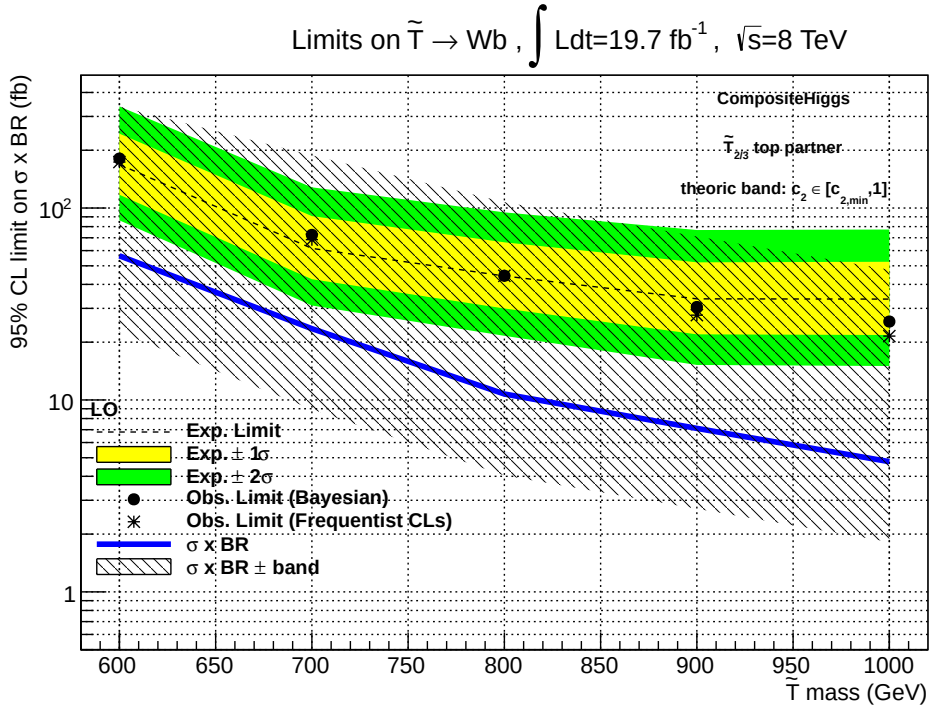

Figure 7.3: 95% CL_s on $\sigma \times Br(Wb)$ of $\tilde{T}$ single production at Large Hadron Collider, $\sqrt{s} = 8\,TeV$ and $\int \mathcal{L}dt = 19.7 fb^{-1}$. Theoric band: $c_2 \in [1/3, 3]$

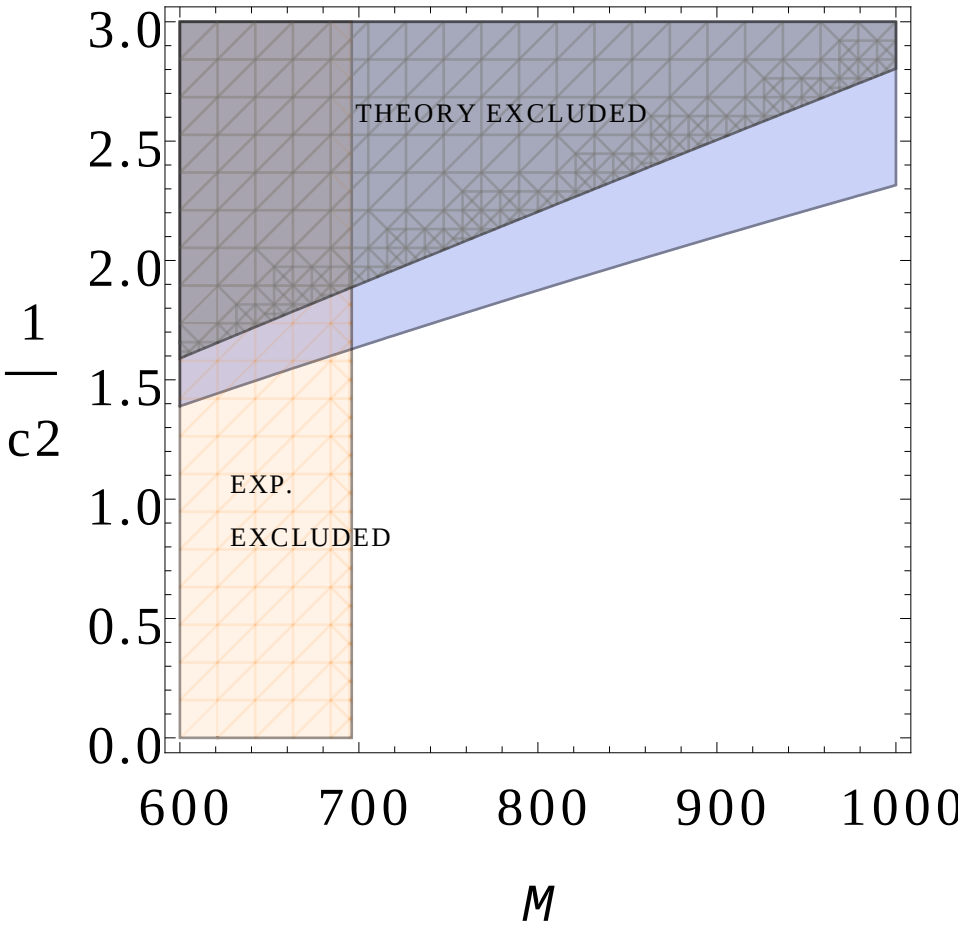

Figure 7.4: 95% CLs excluded region in the $(1/c_2, M_{\tilde{T}})$ space. In blue the excluded area, in orange the present bound given by CMS and ATLAS, [2] and [3]

Chapter 8

Conclusions

The Large Hadron Collider facility, with its high center of mass energy and luminosity, allows for direct search of TeV-scale new physics. We studied top-partners in the single production mechanism, the most promising (for branching ratio and signature) decay channel. We analyzed the signal by exploiting the heaviness of the particle, and the hardness and collinearity of its deacay products, we implemented several cuts to improve the signal-background discrimination. The systematic uncertainties are recasted with an extimation from the single top analysis. We extrapolated the event yields by fitting the pseudo-rapidity of the forward jet of the process, that is a discriminant variable of the signal. The present Thesis has excluded with 95% Confidence Level the presence of the 2/3 charged partner of the top with mass until 1 TeV, in the framework of the Composite Higgs model. The exclusion is sensitive to a large area of the parameter space of the model, as we can see in Fig. 7.4. Event though not all the area is filled, the present work is an important step that could lead to a more complete and efficient analysis to be used at the next Run of the Large Hadron Collider in 2016. As we discussed in the last chapter, more efficient tools can be used to better reconstruct the events. Preparing a dedicated analysis for RunII can immediately start from this work, that despite of its brief nature, contains all the informations to prepare a new analysis. Data completely agrees with Standard Model predictions, hence no new physics is found. We summarize all our work in the two final figures, that we reported here, the exclusion plot and the exluded area in the parameter space. The values of the costant that completely controls the coupling of the top-partner with the Standard Model fermions, c_2 would be naturally $c_2 \sim 1$. In that region we do not be able to exclude nothing, we are sensitive to values $1/3 \leq c_2 \leq 2/3$.

Bibliography

[1] http://cms.web.cern.ch/cms/Media/Images/.

[2] CMS Collaboration, Inclusive search for a vector-like T quark by CMS, (2013).

[3] ATLAS Collaboration, Search for pair production of a heavy top-like quark decaying to a high-p_T W boson and a b quark in the lepton plus jets nal state in pp collisions at $\sqrt{8}$, TeV with the ATLAS detector, (2013).

[4] Alberto Orso Iorio for the CMS collaboration, Measurement of the single top t-channel inclusive cross section and charge ratio and at 8 TeV, CMS AN-2013/032 (2013).

[5] S. Weinberg, Phys. Rev. Lett. 19 (1967).

[6] R. Keith Ellis, W. James Stirling and Bryan R. Webber, QCD and collider physics (CUP, 1996).

[7] CMS collaboration, Phys. Lett. B716 (2012), http://dx.doi.org/10.1016/j.physletb.2012.08.021.

[8] ATLAS collaboration, Phys. Lett. B716 (2012), http://dx.doi.org/10.1016/j.physletb.2012.08.020.

[9] R.D. Peccei, Lect. Notes Phys. 741 (2008), arXiv:hep-ph/0607268.

[10] Super-Kamiokande collaboration, Phys. Rev. D86 (2006), arXiv:hep-ex/1205.6538.

[11] J. Adam et alia, Nucl. Phys. B834 (2010).

[12] Planck collaboration, A. and A. PlanckMission2013 (2013), arXiv:astro-ph.CO/1303.5062.

[13] M. Gell-Mann and F. Levy, Nuovo Cimento 16 (1960).

[14] D.B. Kaplan and H. Georgi, Phys. Lett. B136 (1984).

[15] D.B. Kaplan, Nucl. Phys B365 (1991).

[16] R. Contino, The Higgs as a Composite Nambu-Goldstone Boson, TASI lecture (2009), arXiv:hep-ph/1005.4269v1.

[17] A. Wulzer, Strongly coupled theories and their use (PhD. Lecture, 2013), www.pd.infn.it/ wulzer.

[18] R. Contino, G. Da Rold and A. Pomarol, Lect. Notes Phys. 741 (2008), arXiv:hep-ph/0607268.

[19] C. Callan, S. Coleman, J. Wess and B. Zumino, Phys. Rev. 177 (1969).

[20] S. Coleman, J. Wess and B.Zumino, Phys. Rev. 177 (1969).

[21] M.E. Peskin and T. Takeuchi, Phys. Rev. D46 (1992), doi:10.1103/PhysRevD.46.381.

[22] K. Agashe, R. Contino and A. Pomarol, Nucl. Phys. B719 (2005), arXiv:hep-ph/0412089.

[23] A. De Simone, O. Matsedonskyi, R. Rattazzi and Andrea Wulzer, A first top partner hunter's guide, JHEP 2013:4 (2013), arXiv:hep-ph/1211.5663.

[24] J. Alwall et al., MadGraph 5 : Going Beyond, JHEP 1106 (2011), arXiv:hep-ph/1106.0522.

[25] Particle Data Group, J.e.a. Beringer, Review of Particle Physics, Phys. Rev. D86 (2012).

[26] The LHC Study Group, The Large Hadron Collider Conceptual Design, CERN/AC 95-05 (1995).

[27] http://lpc.web.cern.ch/lpc/lumi.html.

[28] The LHC Study Group, The CMS Experiment at the CERN LHC, JINST 3 S8004 (2008).

[29] CMS Collaboration, The CMS tracker system project: Technical Design Report, CERN (1997).

[30] CMS Collaboration, The CMS tracker: addendum to the Technical Design Report, CERN (2000).

[31] CMS Collaboration, CMS Tracking Performance Results from Early LHC Operation, CERN-PHEP 2010-019 (2010).

[32] CMS Collaboration, CMS silicon strip tracker operation. In Symposium on Radiation Measurement and Applications, SORMAXII (2010).

[33] CMS Collaboration, Operation, calibration and performance of the cms silicon tracker, ICHEP 2010 (2010).

[34] CMS Collaboration, The CMS electromagnetic calorimeter project : Technical Design Report, CERN (1997).

[35] CMS Collaboration, The CMS hadron calorimeter project: Technical Design Report, CERN (1997).

[36] CMS Collaboration, The CMS muon project : Technical Design Report, CERN (1997).

[37] GEANT4 collaboration, GEANT 4 a simulation toolkit, Nucl. Intrum. Meth. 056 (2003).

[38] CMS Collaboration, Fast simulation of the CMS detector, Journal of Physics, Conference Series 219 (2010).

[39] M. Rudowicz and S. Peters. Grindhammer G., Nucl. Instrum. Meth. A290:469 (, 1990).

[40] T. Sjostrand, S. Mrenna, and P. Skands, PYTHIA 6.4 physics and manual,, JHEP 05 026, arXiv:hep-ph/0603175, 2006.

[41] CMS Collaboration, Particle flow event reconstruction in CMS and performance for jets, taus and missing energy, CMS Physics Analysis Summary PFT-9-001 (2010).

[42] R. Fruhwirth, Nucl. Instrum. Methods A262444 (1984).

[43] CMS Collaboration, Reconstruction of electron tracks with the Gaussian-Sum Filter in the CMS tracker at LHC, CMS Analysis Note RN-2003-001 (2003).

[44] CMS Collaboration, Underlying event and jet reconstruction in CMS, CERN (2011).

[45] M. Cacciari, G.P. Salam and G. Soyez, JHEP 04 063 (2008), arXiv:hep-ph/0802.1189.

[46] CMS collaboration, Measurement of the single-top production cross section and charge ratio in the t-channel at $\sqrt{s} = 8\,\text{TeV}$, CMS PAPER TOP-12-038 .

[47] CMS Collaboration, Track Counting b tagging algorithm, CERN (1997), https://twiki.cern.ch/twiki/bin/view/CMSPublic/SWGuideBTagTrackCounting.

[48] CMS Collaboration, b-tagging performance (efficiency and mistag rate) measurements from CMS., (July 2011).

[49] J. Bauer, PhD. thesis, IEKP-KA 2010-08 (2010).

[50] J. Li, D. Liu and J. Shu, Towards the fate of a natural Composite Higgs model through single t' search at the 8 TeV LHC, JHEP 2013:47 (2013), arXiv:hep-ph/1306.5841.

[51] F. Dulat and B. Mistlberger, Limit setting procedures and theoretical uncertainties in Higgs boson searches, JHEP 1205 (2012), arXiv:hep-ph/1204.3851.

[52] http://www-ekp.physik.uni-karlsruhe.de/ ott/theta/theta-auto/.